UNIVERSITA’ DEGLI STUDI DI CATANIA

DIPARTIMENTO DI FISICA E ASTRONOMIA

DOTTORATO DI RICERCA IN SCIENZA DEI MATERIALI E NANOTECNOLOGIE

DOMENICO PELLEGRINO

Effects of ion irradiation on 4H- SiC p-n junction

Tutor: Prof.ssa L. Calcagno

Cotutor: Dott.ssa A. Sciuto

Anno accademico 2020- 2021

Index

Introduction

The increasing dependence of the modern society on electrical appliances for comfort, transportation, and healthcare has motivated the great development of semiconductor materials and devices for power generation, distribution and management technologies [Baliga2005], [Kimoto2014]. Around the 1950, the invention of the silicon (Si) based metal-oxide semiconductor field effect transistors (MOSFETs) led to the solid-state electronics birth [Kimoto2014]. Although the reliability of these devices grew rapidly, their fundamental limitation is related to costly solutions and the relatively low operating voltages (under 100 volts) [Baliga2005]. In the meantime, compound semiconductors have established unique positions in those applications where Si-based devices cannot exhibit good performance because of the inherent material properties. The development of power electronics is pushing towards wide bandgap semiconductor.

In this context, the silicon carbide (SiC) is a wide bang gap semiconductor characterized by very high hardness, temperature stability, chemical inertness, high thermal conductivity, high breakdown voltage and high critical electric field strength that make it a promising material for the devices operating in hostile environment such as those high voltage, high temperature and radiation rich [Kimoto2014], [Willander2006], [Matsunami2004]. In particular, SiC base p-n junction and Schottky diodes, fundamental elements of microelectronics and solid state devices, find wide applications in the UV, X-ray and charged particles detectors [Litrico2018], [Mazzillo2015], [Cutroneo2013], [Torrisi2012], [Nava2008], [Seely2005]. Over the last years, considerable effort has been concentrated on better understanding the performance of SiC- based radiation detectors to be used in high temperatures and high radiation conditions under which conventional semiconductors detectors cannot be adequately used [Nava2008]. SiC detectors were used with good results for neutrons

[Ruddy2006], for x-rays [Bertuccio2003] and for charged particles emitted by alpha sources [Torrisi2012], [De Napoli2007]. The possibility to use X-ray SiC detectors operating at room or high temperature is of large interest as an alternative to conventional detectors that must operate at cryogenic temperatures [Bertuccio2003]. Moreover, SiC detectors have been used to monitor the ionizing radiation emitted from high intensity laser- generated plasma [Musumeci2014], [Cutroneo2013], [Torrisi2009], permitting prompt measurements of X-rays and ions emitted during the short life of pulsed plasma [Margarone2008]. In particular, Torrisi et al. [Torrisi2015] has proved that SiC detectors, with an interdigit Ni_2Si front electrode, were able to detect ultraviolet radiation, soft X-rays, and low energy ions generated by a low intensity laser. In such applications these detectors showed high efficiency and very short rise time, due to their particular design that leaves a fraction of the active region directly exposed to the impinging radiation [Sciuto2016], [Torrisi2015].

The power electronics, concept introduced by Newell in 1973, involves conversion of electric power by using semiconductor devices. Today, power electronics is one of the most promising strategies to improve the power conversion in order to reduce dissipation. Moreover, the realization of high-performance power devices will lead to enormous energy saving, conservation of fossil fuels and environmental pollution reduction.

The main applications of power semiconductor devices (figure 1) include power supplies, motor control, telecommunications, heating, robotics, electric/hybrid vehicles, traction and electric power transmission [Baliga2005], [Kimoto2014], [Nigam2002]. Among these possible applications, SiC based power devices are promising for medium- high voltage area applications such as UV, X-ray and charged particles detectors, electric/hybrid vehicles, traction and electric power transmission where there is the request of operating at voltage higher than 300V, low- loss

power devices, high thermal dissipation and wide temperature range [Kimoto2014], [Cutroneo2013], [Torrisi2012], [Nava2008].

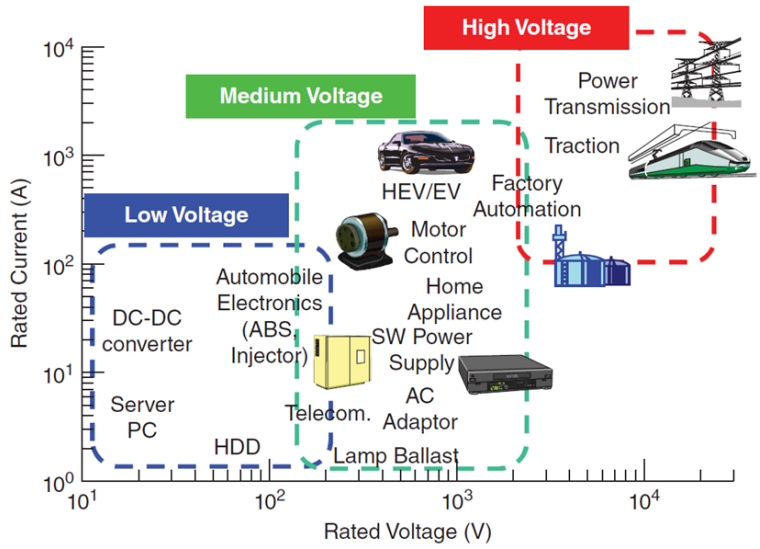

Figure 1: Main application of power semiconductor devices in a plot of rated current (A) as a function of rated voltage (V) [Kimoto2014].

The ion irradiation modifies the electric properties of the semiconductor devices and material [Baliga2008], [Izzo2008], [Claeys2002].

Proton or alpha particles irradiation as well as electron and neutron can be used in SiC technology to improve the power devices electrical performance as well as to control the carrier lifetime; electron and proton irradiation is widely used in silicon power devices for example to reduce the turn-off time [Baliga2008]. The full knowledge of the defects induced by irradiation as well as their effects on SiC based devices properties is a fundamental point and a full knowledge is still missing.

In the present thesis the effect of the defects induced by ion irradiation on the electrical properties of p-n junction will be investigated in details. Indeed, the goals of this thesis are the study of the radiation induced point defects in n-type 4H-SiC and their evolution as a function of the irradiation

fluence as well as the study of the radiation induced changes in the SiC p-n junction electrical properties.

In the chapter 1 an overview of silicon carbide is presented in order to evidence its characteristic properties that rough out this material suitable in applications where Si cannot be used.

In the chapter 2 the theory of p-n junction is displayed in details in order to clarify the main parameters of this simple devices and explain the main mechanisms responsible of current flow. Moreover, the SiC- based devices together their peculiar properties and the irradiation effects on these devices are also presented.

The chapter 3 deals with the processes used for the fabrication of SiC based p-n junction and the main techniques used for its characterization.

The chapter 4 illustrates the results about the effects of ion irradiation on room temperature electrical properties of the junction as well as their temperature behaviour.

The whole work is the result of an extremely intense collaboration between the University of Catania and the CNR-IMM HQ.

Chapter 1

Silicon Carbide: materials and defects

Silicon carbide (SiC) crystallizes in a wide variety of structures, each of which exhibits unique electrical, optical, thermal, and mechanical properties. For these properties it is nowadays the dominant material of electronic industry. However, many of these properties can be modified by irradiation.

The physical properties of SiC and the radiation induced defects are very important subjects for fundamental studies as well as for an accurate prediction of devices performance.

In this chapter are described the crystallographic structures and the main electrical properties of SiC as well as the main defects induced by irradiation.

1.1 Crystallographic structure

The silicon carbide (SiC) was discovered by Berzelius in 1824 and it is characterized by a rigid stoichiometry: 50% silicon and 50% carbon atoms. In the crystal both Si and C atoms are tetrahedrally bonded with covalent bonds by sharing electron pairs in sp^3- hybrid orbitals. The strong chemical bonding between Si and C atoms, with a bond energy of 4.6 eV, gives to the material unique properties such as very high hardness, chemical inertness and high thermal conductivity [Kimoto2014]. From a crystallographic point of view, the variation in the silicon and carbon occupied sites along the c-axis in a hexagonal close-packed system (figure 1.1.1) brings about different crystal structures, called polytypes. Due to the high thermal stability [Kimoto 2014] the most studied SiC polytypes (figure 1.1.2) are the following: 3C, 4H and 6H where the notation letter indicates the crystal

system that it is cubic for C and hexagonal for H. Instead, the notation number indicates the occupied sites sequence in the structure; for example, in the 3C we have ABC while for the 4H we have ABCB, as shown in Fig. 1.1.1.

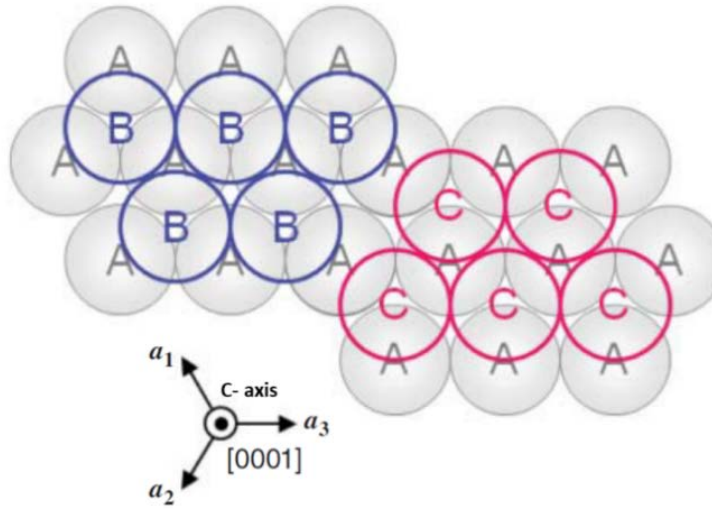

Figure 1.1.1: Occupation sites (A, B, and C) in the hexagonal close-packed system [Kimoto2014]

The silicon carbide lattice sites can have different structure in their immediate neighbors because of the different way to stack Si-C bilayers in the crystallographic structure. In particular, it is possible to distinguish among hexagonal sites in the case of the lattice sites with hexagonal-structured surroundings and cubic sites when it has cubic-structured surroundings. In figure 1.1.2 hexagonal and cubic sites are indicated by “h” and “k”, respectively; moreover, the figure shows the [0001] direction for 4H and 6H- SiC and [111] direction for 3C-SiC, using Miller- Bravais notation [Kimoto2014]. Instead, the 4H-SiC has one hexagonal and one cubic site [Kimoto2014].

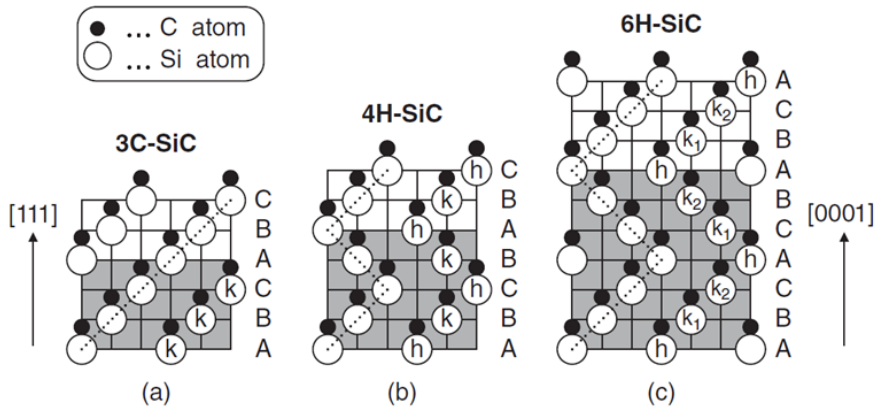

Figure 1.1.2: Structures of SiC polytypes; (a) 3C-SiC, (b) 4H-SiC, and (c) 6H-SiC. Open and closed circles denote Si and C atoms, respectively [Kimoto2014].

1.2 Electrical properties

SiC semiconductor exhibits an indirect band structure with band gap values of 2.36 eV, 3.02 eV and 3.26 eV for the 3C, the 6H and the 4H-SiC respectively; all are much large than the Si band gap (1.1 eV) [Kimoto2014].

The wide band gap of SiC allows a smaller carrier generation in the device depletion regions which is fundamental to reduce the leakage current of the p-n and metal-semiconductor-junction based devices [Baliga2005]. In particular, in power device applications, 4H-SiC is preferred because of its larger gap with respect to the other polytypes [Kimoto2014].

The intrinsic carrier density (n_i) is determined by the thermal generation of electron- hole pairs across the semiconductor energy band gap E_g. Its value can be calculated by using the densities of states in the conduction band N_C and in the valence band N_V [Baliga2005]:

$$n_i = (N_C \cdot N_V)^{1/2} \quad e^{\left(-\frac{E_g}{2kT}\right)} \qquad (1.2.1)$$

where k the Boltzmann constant and h the Plank constant [Kimoto2014].

The figure 1.2.1 shows the temperature dependence of the intrinsic carrier density for silicon and for different SiC polytypes (3C, 4H and 6H- SiC) [Kimoto2014]. The intrinsic carrier density for silicon carbide is smaller than that for silicon due to the large difference in bandgap energy. At room temperature (300 K), the carrier density is $1.4x10^{10}$ cm^{-3} for silicon [Baliga2005] and 0.13 cm^{-3}, $1x10^{-6}$ cm^{-3} and $5x10^{-9}$ cm^{-3} for 3C, 6H and 4H-SiC, respectively [Kimoto2014]. This property allows the SiC- based electronic devices to operate at high temperatures with low leakage current thanks to the Fermi level position far from the SiC midgap and to the incomplete ionization of the dopant [Kimoto2014], [Baliga2005], [Sze1981].

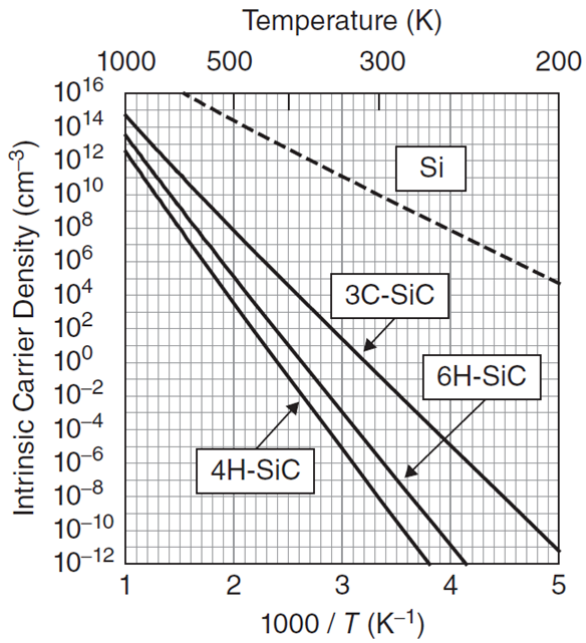

Figure 1.2.1: Intrinsic carrier density of silicon (Si), 3C, 4H and 6H- SiC [Kimoto2014].

Instead, the impact ionization coefficient for electrons α_n (holes, α_p) is defined as the number of electron- hole pairs created by an electron (hole) traversing 1 cm through the depletion layer along the direction of the

electric field. Both electron and hole impact ionization coefficient α is dictated by Chynoweth's law [Baliga2008]:

$$\alpha = a \cdot e^{(-\frac{b}{E})} \qquad (1.2.2)$$

where E is the electric field component in the direction of current flow while a and b are semiconductor material constants. In particular, for silicon they are a_n= 7x10^5 cm^{-1} and b_n=1.23x10^6 Vcm^{-1}, for electrons and a_p= 1.6x10^6 cm^{-1} and b_p=2x10^6 Vcm^{-1}, for holes. The silicon carbide parameters a and b are greater than that of silicon; in the case of 4H-SiC, they are a_n= 3.13x10^8 cm^{-1} and b_n=3.45x10^7 Vcm^{-1}, for electrons and a_p= 8.07x10^6 cm^{-1} and b_p=1.5x10^7 Vcm^{-1}, for holes [Baliga2008].

The impact ionization coefficient has a strong dependence upon the electric field for both silicon and 4H-SiC (figure 1.2.2). The onset of carrier generation by impact ionization occurs at much larger electric fields in 4H-SiC than in silicon; thus, the breakdown for 4H-SiC based electronic devices occurs at higher electric fields. For the 4H-SiC critical electric field E_C for breakdown is in the range 2- 3 x 10^6 V/cm and when it exceeds 10^4 V/cm, as commonly encountered in power devices, the drift velocity saturates [Kimoto2014], [Baliga2008].

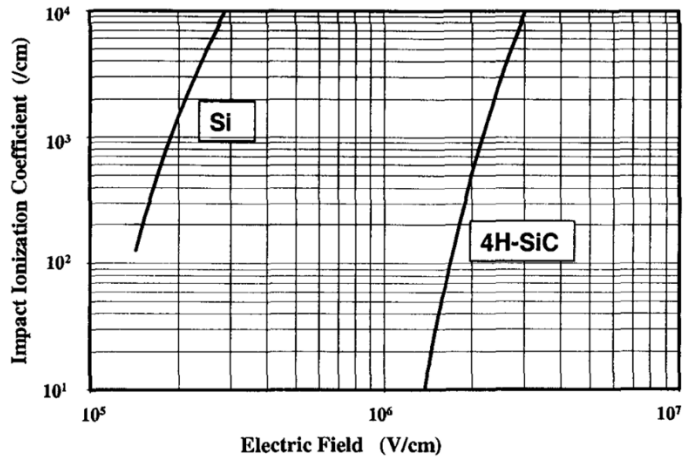

Figure 1.2.2: Impact ionization coefficient for Silicon and 4H-SiC [Baliga2005]

An important parameter in semiconductor is the carrier mobility which depends on carrier concentration and temperature. The figure 1.2.3 shows the electron (figure 1.2.3 a) and hole mobility (figure 1.2.3 b) as a function of donor density and acceptor density, respectively, at room temperature in 4H and 6H- SiC. The electron mobility of 4H-SiC is almost double that of 6H-SiC at a given dopant density, and 4H-SiC exhibits a slightly higher hole mobility than 6H-SiC. In particular, the maximum electron and hole mobility in 4H- SiC are about 1200 $cm^2V^{-1}s^{-1}$ and 120 $cm^2V^{-1}s^{-1}$, respectively. The higher 4H-SiC carrier mobility makes this polytype the most attractive for electronic power devices application [Kimoto2014].

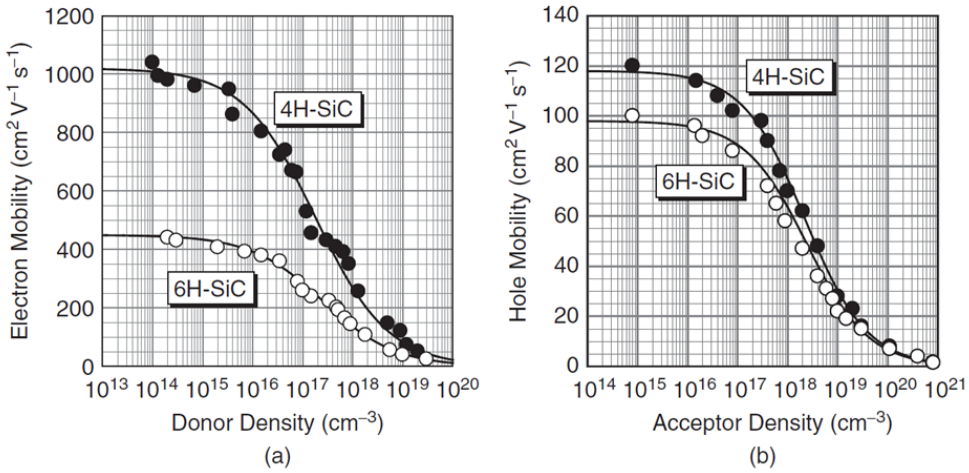

Figure 1.2.3: (a) electron and (b) hole mobility as a function of donor density and acceptor density, respectively, for 4H-SiC and 6H-SiC at room temperature [Kimoto2014].

However, at low doping concentration, the 4H-SiC electron mobility μ_n and hole mobility μ_p are smaller than the carrier mobility in silicon (figure 1.2.4). In both cases, the carrier mobility decreases with increasing doping concentration due to enhanced Coulomb scattering of free electron and hole by the ionized donors and acceptors [Baliga2005].

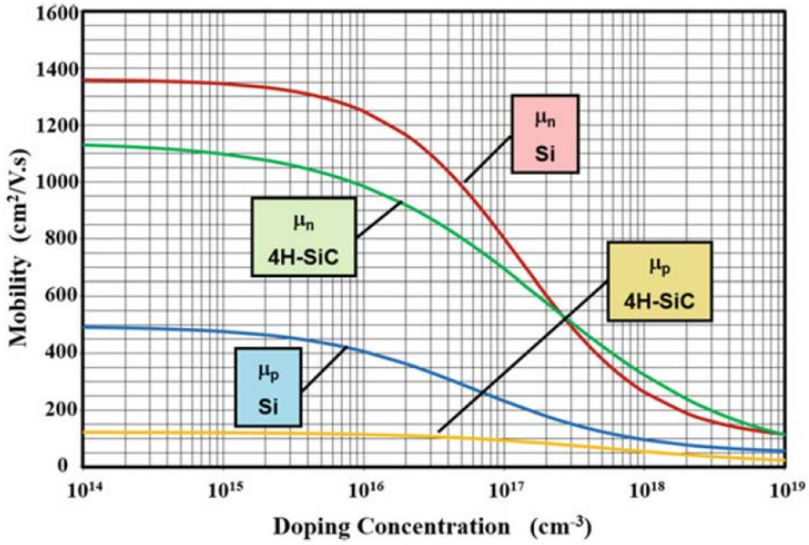

Figure 1.2.4: Bulk mobility for electrons (μ_n) and holes (μ_p) in silicon and 4H-SiC at room temperature [Baliga2008].

The carrier mobility depends also on temperature and in figure 1.2.5 is shown the temperature dependence of electron mobility μ_n and hole mobility μ_p for the 4H-SiC and silicon, both with a doping concentration below 10^{15} cm^{-3}. In both cases there is a rapid reduction of the mobility with increasing temperature. As for the silicon carbide, also the silicon mobility depends from T^{-n}. In particular, n is 2.7 and 3.4 for low n- doped and p-doped 4H-SiC, respectively; instead, it is 2.42 e 2.20 for low n- doped and low p- doped silicon, respectively [Baliga2008].

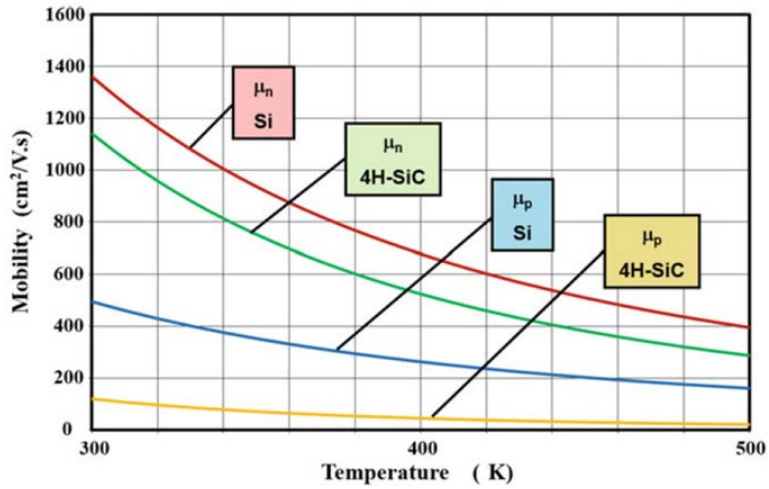

Figure 1.2.5: Temperature dependence of the mobility for electrons (μ_n) and holes (μ_p) in silicon and 4H-SiC [Baliga2008]

1.3 Silicon carbide defects

Point defects can be introduced in semiconductor, such as silicon carbide, during device processing or by irradiation of final device. They are imperfections that occurs at a specific location, or point, in a crystal. This is in contrast to an extended defect, which is not confined to a specific lattice site. A dislocation, for example, is a one-dimensional “line” defect [Kimoto2014].

Point defects, in turn, can be intrinsic and extrinsic defects: (1) intrinsic or native defect, which involve only the atoms of the host crystal, and (2) extrinsic defects, which involve impurity atoms. When an impurity is deliberately introduced into a semiconductor, it is referred to as a dopant.

The main point defects are vacancy, interstitial, impurity atoms and antisites in the case of compound semiconductors, like SiC [Tuomisto2019], [Nastasi2006].

Extended or structural defects are permanent deviations from structural perfection that is from the correct placement of atoms in real crystals. Extended defects are usefully classified by the number of dimensions in

which they are extended, that is, of greater than atomic size, into volume, surface and line defects.

Extended defects are generally introduced during growth process such as CVD epitaxial growth. Main extended defects are surface morphological defects, dislocation, stacking faults and micropipes [Kimoto2014].

1.3.1 Point and point like defects

The point defects are microscopic defects due to the deviation in the periodicity of the crystal lattice arising from a single point. The main point defects are show in the figure 1.3.1. The vacancy consists in the absence of one atom from its position in the crystal lattice. The interstitial defect is an atom situated in a forbidden position of the lattice, if this position is not occupied by a foreign atom the defect is also called self- interstitial. The substitutional defects are due to an external atom such as an impurity which replaces the crystal atom in the lattice position [Tuomisto2019], [Nastasi2006]. In the case of a diatomic semiconductor like SiC, the exchange between the carbon and silicon atoms in their lattice positions forms the antisite defects [Kimoto2014], [Tuomisto2019].

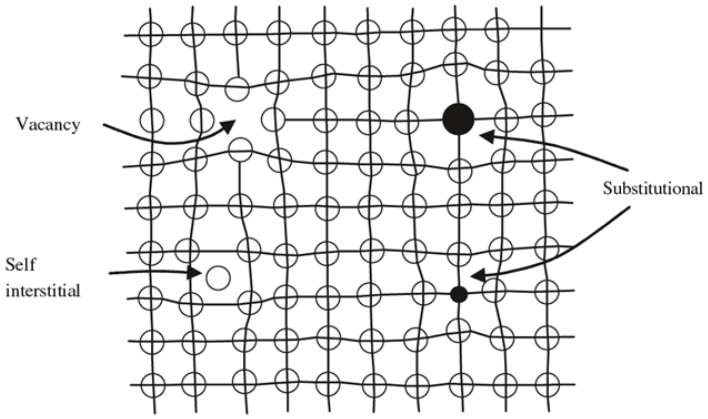

Figure 1.3.1: Points defects in a two- dimensional and monoatomic crystal [Nastasi2006]

The interaction between points defects gives rise to point like defects, as divacancy (V_{Si}- V_C), vacancy- interstitial pairs (also called Frenkel defects) and antisite pairs (Si_C- C_{Si}) in SiC [Kimoto2014].

The presence of these defects can induce a reduction in semiconductor free carrier concentration due to the compensation effect, a passivation of donors when interact with point defects, as well as they can affect the material electric properties such as electrical resistance, electron mobility and carrier lifetime [Kimoto2014], [Izzo2008]. These defects modifying the electrical properties of devices, may result in a permanent failure of the systems [Kimoto2014], [Claeys2002].

1.3.2 Ion irradiation defects

The silicon carbide point and point like defects can be introduced during epitaxial growth as well as during ion and electron irradiation [Kimoto2014], [Izzo2009], [Alfieri2005], [Lebedev2000] [Danno2005]. In particular, energetic particles penetrating through a material decelerate and the transferred energy produces a damage in crystal lattice, known as displacement damage, with a consequent production of vacancies-interstitial pairs [Claeys2002]. These defects are responsible of deep levels into the semiconductor band gap that act as recombination centers and affect the material resistivity, carrier lifetime and mobility [Kimoto2014], [Izzo2008].

The main technique used for the characterization of these levels is the Deep Level Transient Spectroscopy (DLTS). It is based on the variation in the electrical capacity of a Schottky (or p-n junction) diode as a function of temperature following the application of a periodic voltage pulse. The analysis of the acquired spectrum allows to obtain, for each level, different information such as its energy position in the band gap, the capture cross section and the level (defect) concentration [Lang 1974], [Shroder2006],

[Kimoto2014]. However, this technique is not able to give information about the microscopic structure of the defects, but complementary technique as Electron Paramagnetic Resonance (EPR) can be used to this purpose [Kimoto2014], [Kawara2013], [Lebedev2000]

Literature report about SiC Schottky diodes or p-n junction irradiated with different ions, electron and neutrons and the DLTS spectra evidenced the formation of different defects [Lebedev2000], [Dalibor1997], [Hazdra2014], [Castaldini2004], [Danno2005], [Danno2007].

In figure 1.3.2 it is shown a DLTS spectra of a Schottky Ni_2Si/n- type 4H-SiC junction irradiated with 7 MeV carbon ion C^+ in a wide fluence range, from 10^9 to 10^{13} ion/cm^2 (figure 1.3.2). The unirradiated sample shows only a small peak at 300 K related to the $Z_{1/2}$ defect. This defect, present also in as –grown n- type 4H-SiC [Kimoto2014], introduces an energy level at E_c- 0.63/ 0.66 eV (E_C is the bottom of conduction band energy) and it is related to the carbon vacancy [Kimoto2014]. However, the microscopic structure of the $Z_{1/2}$ defect is not well known and some authors associated this defect to a carbon interstitial or antisites [Castaldini2004], [Izzo2009].

After C^+ irradiation, the intensity of $Z_{1/2}$ related peak increases (figure 1.3.2) and there is the formation of other two peaks at 480 K and 650 K, respectively, with a shoulder at 550 K (figure 1.3.2). The formed defects are $RD_{1/2}$ and RD_4 located at 0.98 eV and 1.4 eV below the conduction band edge, respectively. As regards their microscopic nature, the $RD_{1/2}$ level is related to a defect formed by a carbon and silicon vacancy, while the RD_4 [Izzo2009] or $RD_{1/4}$ [Izzo2008] level is related to the carbon vacancy. These two defects have been observed after irradiation and their intensities (trap concentration) increase and evolve with increasing the ion fluence. In particular, at irradiation fluence of 10^{13} ion/cm^2 only the RD_4 defects survive (figure 1.3.6 b). Moreover, high irradiation fluence induce the recombination and aggregation of these different point defects [Izzo2009].

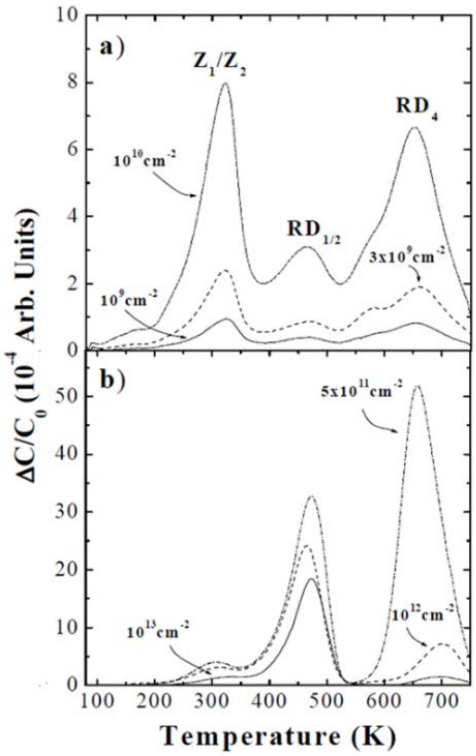

Figure 1.3.2: DLTS spectra of 4H-SiC epitaxial layer irradiated with 7.0 MeV C^+ in the low fluence (a) and in the high fluence range (b) [Izzo2009].

High energy electron and light ions as proton or helium irradiation of SiC produces also point defects and in figure 1.3.3 are shown DLTS spectra of 4H-SiC epitaxial layer irradiated with 15 MeV electron with fluence 4 $x10^{14}$ ion/cm^2 (figure 1.3.3 a) and 1.2 MeV proton with fluence ranging 10^9- 10^{10} ion/cm^2 (figure1.3.3 b); after irradiation the sample was annealed at 400, 600 and 800 °C for 20 min [Alfieri2005]. In addition to the $Z_{1/2}$, there is the formation of $EH_{6/7}$ defect [Alfieri 2005], located at 1.55 eV below the conduction band edge [Kimoto2014]. This defect is also present in as-grown n- type 4H- SiC and its microscopic structure is related to the carbon vacancy with a different charge state than the $Z_{1/2}$ [Kimoto2014]. Both electron and proton irradiation induces the EH_4 and EH_5 defects formation [Alfieri 2005], [Hemingsson 1997], [Castaldini2004], [Doile1998],

[Storasta 2004]: the EH_4 defects, located into the band gap at E_C- 0.72 eV, is related to the isolated vacancies or interstitial defect [Doile1998], instead EH_5, located into the band gap at E_C- 1.13/ 1.17 eV [Hemingsson1997], [Fabbri2009], is related to the complex defect of silicon and carbon vacancies [Hemingsson1997], [Fabbri2009].

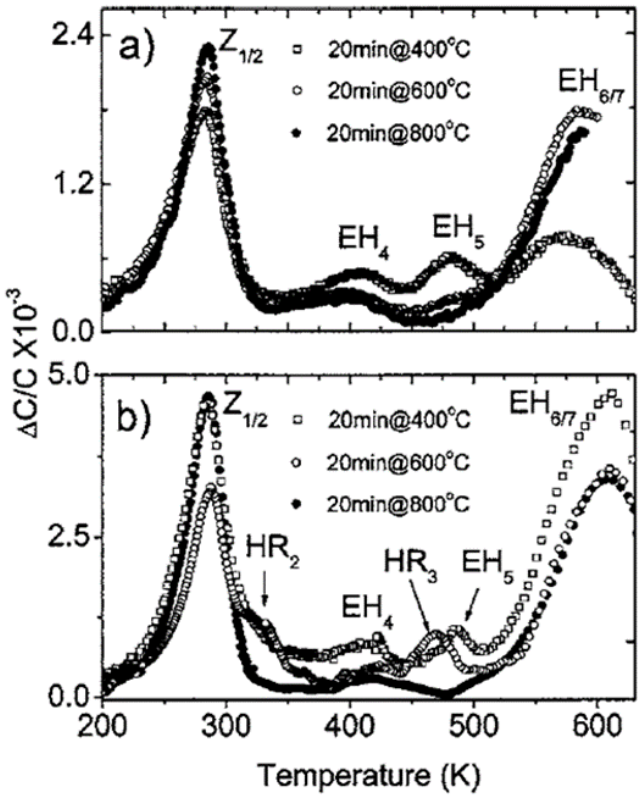

Figure 1.3.3: DLTS spectra of as-irradiated samples and of samples after annealing processes at 400 °C, 600 °C, and 800 °C and (a) 15 MeV electrons and (b) 1.2 MeV protons [Alfieri2005].

Moreover, the proton irradiation induces also the formation of the other defects: $RD_{1/2}$ [Castaldini2005], HR_2, located at E_C- 0.69 eV, and HR_3, located at E_C- 1.03 eV. The last two are related to the interaction between Hydrogen atom and silicon and carbon vacancies, respectively. The post-irradiation annealing produces a decrease of the defect concentration

(related to the height of the different peak [Lang 1974]), and at temperature of 800°C only $Z_{1/2}$ and $E_{6/7}$ survive [Alfieri2005]. Both these defects are stable at the temperature up to 1700 °C [Kimoto2014].

The different data reported in literature evidence that the irradiation induces the formation of different defects such as RD $_{1/2}$, RD $_{1/4}$, EH4 and EH5; in particular, some of these such as $Z_{1/2}$ and $EH_{6/7}$ are present also in as-grown 4H- SiC and they are stable at temperature up to 1700°C. Moreover, the increase of ion fluence can produce an increase in the defects concentration and an evolution of point defects.

Chapter 2

P-N Junction theory and SiC based devices

The silicon carbide for its properties allows the realization of different kinds of devices characterized by high performances, high efficiency and high reliability. The SiC-based devices can be summarized into three general classes: power switching, microwave, and specialty devices (sensors, high-temperature integrated circuits, etc.). They are mainly based on unipolar devices such as SBD (Schottky barrier diode) and MOSFET (Metal Oxide Semiconductor Field Effect Transistor) or on bipolar devices such as BJT (Bipolar Junction Transistors) and IGBT (Insulated- Gate Bipolar Transistors) [Kimoto2014].

All bipolar junction devices have the p-n junction diode as fundamental component [Kimoto2014], [Baliga2008], [Neudek1983]. This simple bipolar device is a homo-junction, generally realized by two types of semiconductor materials, p-type and n-type, inside a single crystal of semiconductor. The "p" (positive) side contains an excess of holes, while the "n" (negative) side contains an excess of electrons in the outer shells of the electrically neutral atoms. This allows electrical current to pass through the junction only in one direction. The p-n junction is created by doping, for example by ion implantation or epitaxy (growing a layer of crystal doped with one type of dopant on top of a layer of crystal doped with another type of dopant) [Kimoto2014], [Neudek1983].

2.1 P- N junction theory

The basic theory on p-n junction and its characteristics were introduced by Schockley in 1950 [Shockley1950].

For simplicity, let's consider a step junction at $x_j = 0$ in one dimensional approximation and without the application of external bias $V_A = 0$ (figure 2.1.1). Moreover, the p and n- type regions are uniformly doped and let's suppose that the acceptor concentration N_A in p side is much higher than the donor concentration N_D in n side, both parts are electrically connected by means of two perfect ohmic contacts and the charge neutrality exists everywhere in the device [Neudek1983], [Sze1981].

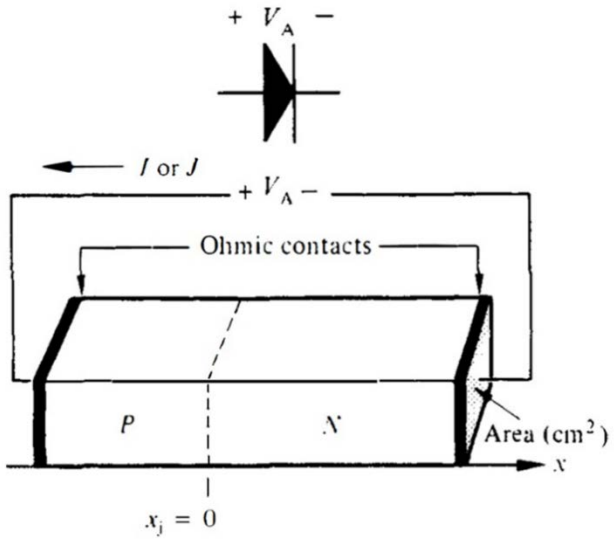

Figure 2.1.1: Symbol to indicate the standard p-n junction (top) and one dimensional step p-n junction (bottom) [Neudek1983]

2.1.1 P-N junction static properties

In the static condition, the hole and electron diffuse within the material (the holes diffuse from the p- to the n- side and electrons will diffuse in opposite direction) so as to make their concentration homogeneous throughout the material. The diffusion process disrupts the charge balance in p side and in n side and, thus, it cannot continue forever. The imbalance charge (figure 2.1.2 a) due to the diffusion implies the existence of an electric field (figure 2.1.2 b) and therefore a potential difference (figure 2.1.2 c). The produced negative electric field has a maximum value $\mathcal{E}_m$ at $x_j = 0$ and it counteracts

the carrier diffusion so that under thermal equilibrium the net flow of carriers is zero. The space charge region, near the junction, where the mobile carrier concentration has been reduced below their thermal equilibrium value is called the depletion region W. Instead, the voltage across the junction depletion region is called built-in or diffusion potential V_{bi} (figure 2.1.2 c) [Neudek1983], [Sze 1981]. The p-n junction band structure at thermal equilibrium is shown in figure 2.1.2 d where E_c is the conduction band edge, E_v is the valence band edge, E_i the intrinsic Fermi level of the semiconductor and E_F the line- up Fermi level of the system [Neudek1983]:

$$[E_f - E_i]_{\text{p-type}} = - kT \ln \left(- \frac{p_p}{n_i}\right) \qquad (2.1.1)$$

$$[E_f - E_i]_{\text{n-type}} = kT \ln \left(- \frac{n_n}{n_i}\right) \qquad (2.1.2)$$

Where n_n and p_p are the electron and hole concentrations in n and p- type semiconductors, respectively. The built-in potential V_{bi} is given by following equation [Neudek1983]:

$$[E_f - E_i]_{\text{n-type}} - [E_f - E_i]_{\text{p-type}} = q\, V_{bi} \qquad (2.1.3)$$

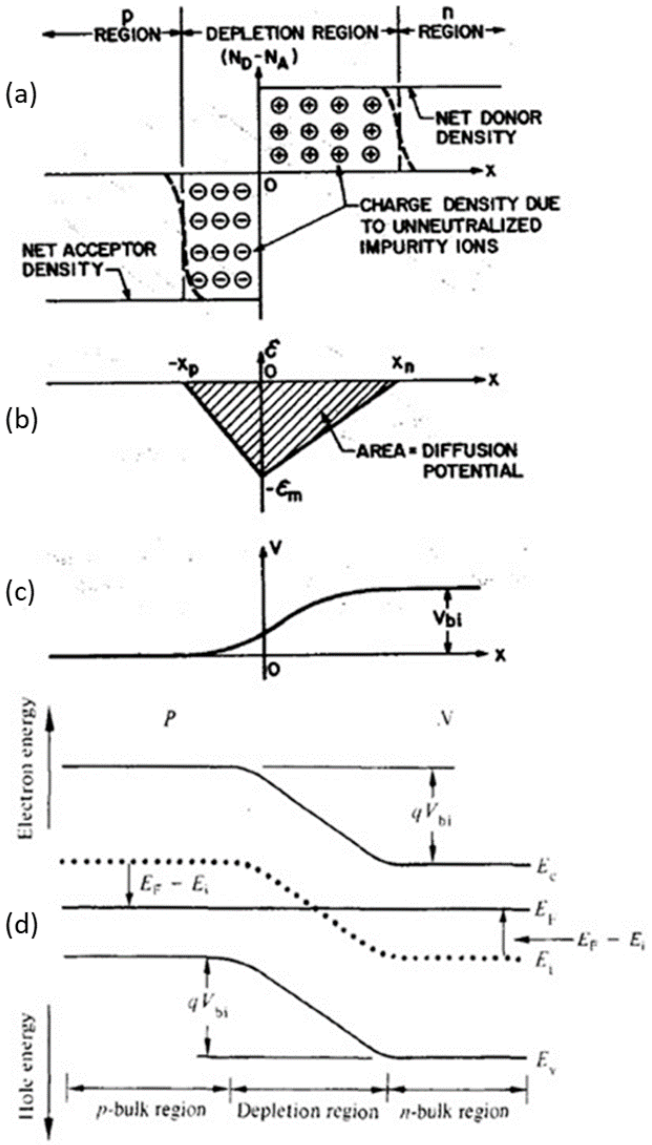

Figure 2.1.2: p-n junction under thermal equilibrium (a) charge distribution into the space charge region, (b) the electric field distribution, (c) the potential variation with the distance [Sze1981] and (d) p-n junction energy band diagram at thermal equilibrium [Neudek1983]

The depletion region capacitance C_J is defined as the ratio between the incremental increase in charge dQ_c and the incremental change of the

applied voltage dV_A [Sze1981], it is related to the depletion region width W by following equation [Neudek1983]:

$$C_J = \frac{A K_s \varepsilon_0}{W} \tag{2.1.4}$$

where K_S is the relative dielectric constant, ε_0 is the vacuum dielectric constant, A is the junction area.

By solving the Poisson equation under an external bias V_A [Neudek1983], the depletion region width W is obtained [Neudek1983], [S. M. Sze 1981]:

$$W = \left[\frac{2 K_s \varepsilon_0}{q} (V_{bi} - V_A) \frac{N_A + N_D}{N_A N_D} \right]^{1/2} \tag{2.1.5}$$

By substituting the equation (2.1.5) in (2.1.4), the C_J equation becomes [Neudek1983]:

$$C_J = (A K_S \varepsilon_0) \cdot \left[\frac{2 K_s \varepsilon_0}{q} (V_{bi} - V_A) \frac{N_A + N_D}{N_A N_D} \right]^{-1/2} \tag{2.1.6}$$

The equation (2.1.6) implies that C_J decreases as V_A becomes more negative (figure 2.1.3) due to the W increase by depleting majority carrier [Neudek1983], [Baliga2008].

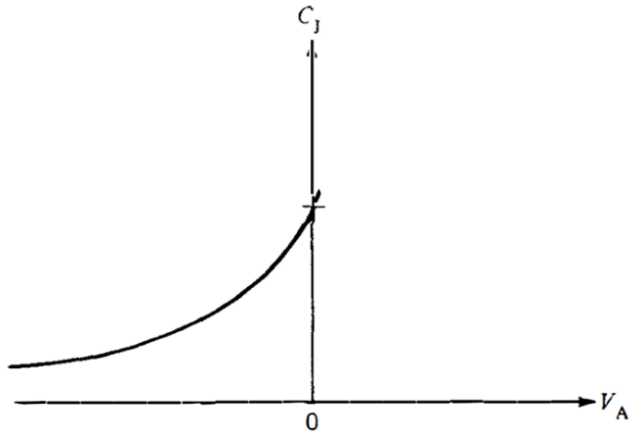

Figure 2.1.3: Depletion capacitance C_J as a function of reverse voltage V_A [Neudek1983]

2.1.2 P-N junction current- voltage characteristic

To obtain the ideal diode equation let's consider the p-n junction of the figure 2.1.1 and let's suppose the following: (1) in all depletion region the mobile carrier concentrations are small of donor and acceptor concentrations (depletion approximation) [Neudek1983], (2) the injected minority carrier densities are negligible with respect than that of majority carrier and (4) no generation- recombination current exists in the depletion layer [Sze 1981].

Under thermal equilibrium (band diagram in figure 2.1.2 d) the current can flow by drift due to the negative electric field and by diffusion due to the carrier concentration gradient among the two side of the junction.

The total current density is given by following equation [Neudek1983]:

$$J = J_p + J_n \tag{2.1.7}$$

Explaining the currents component [Neudek1983]:

$$J_p = q\,\mu_p\,p\,\mathcal{E} - q\,D_p\left(\frac{dp}{dx}\right) \tag{2.1.8}$$

$$J_n = q\,\mu_n\,n\,\mathcal{E} - q\,D_n\left(\frac{dn}{dx}\right) \tag{2.1.9}$$

Where the first terms of the equations 2.1.8 and 2.1.9 are the drift current component, depending by electric field $\mathcal{E}$, electron and hole concentration in n- side n and in p- side p, respectively, and by electron and hole mobility in n- side μ_n and in p- side μ_p, respectively. Instead, the diffusion component, second term in the equations 2.1.8 and 2.1.9, depends by the gradient of electron and hole concentration, respectively, and by the carrier diffusion coefficients D_N and D_P [Neudek1983].

At thermal equilibrium the carrier flux due to drift is equal and opposite to that of diffusion, therefore the net current is zero: J = 0 [Neudek1983].

If a forward bias V_A is applied to the structure (figure 2.1.4), the n side bulk region is shifted upward in electron energy (proportional to the applied voltage V_A). Moreover, the slope of the band edges in the depletion region is reduced respect to the thermal equilibrium value, therefore the energy barrier for hole in the p region and for electron in n region is reduced from $q \cdot V_{bi}$ to $q \cdot (V_{bi} - V_A)$ where q is the charge and V_{bi} the built- in potential. The net effect of forward bias application is a large increase in the diffusion current components due to the large number of holes and electrons with energy greater than the barrier height, thus the number of carriers able to diffuse increases exponentially [Neudek1983], [Sze 1981].

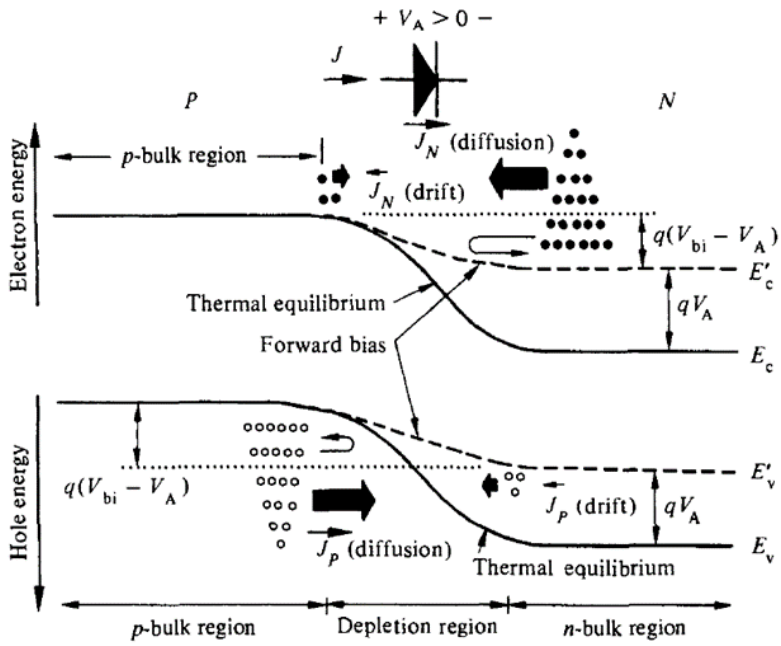

Figure 2.1.4: Band diagram and current flux of a p-n junction with forward bias $V_A > 0$ [Neudek1983]

The opposite situation is obtained for the reverse polarization $V_A < 0$ (figure 2.1.5). The n side bulk region is shifted downward in electron energy. Therefore, the number of holes and electrons with a sufficient energy to get over the potential barrier is reduced; the diffusion current is less than its

thermal equilibrium value. However, the drift current component remains at the thermal equilibrium value, being limited by the number of thermally generated carrier. Because the drift component is independent of barrier height, the current becomes a constant after several tenths of volts. The net reverse current I_0 is small, negative and independent by V_A after a few of volt [Neudek1983].

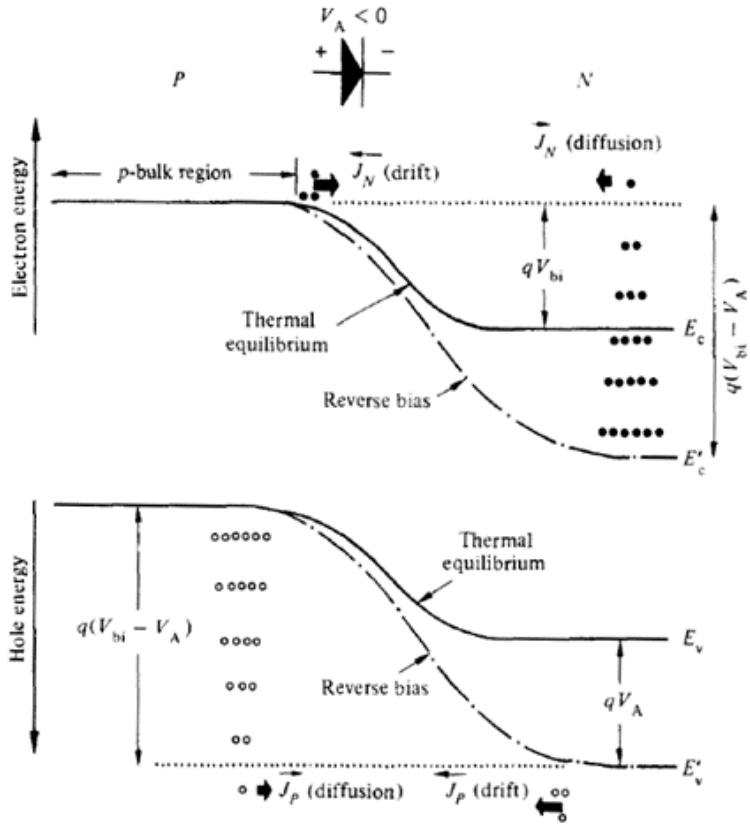

Figure 2.1.5: Band diagram and current flux of a p-n junction with reverse bias $V_A < 0$ [Neudek1983]

The ideal diode or Shockley equation, relation between the current density J and the applied voltage V_A, is the following [Neudek1983], [Sze 1981]:

$$J = q\,(L_n^{-1}\,D_n\,n_{p0} + L_p^{-1}\,D_p\,p_{n0}) \cdot (e^{\,qV_A/kT} - 1) \qquad (2.1.10)$$

Multiplying by the junction area A, the total current I is obtained [Sze1981]:

$$I = I_0 \left(e^{qV_A/kT} - 1\right) \tag{2.1.11}$$

Where I_0 is called saturation current [Sze 1981]:

$$I_0 = A\, q \left(L_n^{-1} D_n n_{p0} + L_p^{-1} D_p p_{n0}\right) \tag{2.1.12}$$

The curve of current I (or current density J) as a function of applied voltage V_A is called I or J – V curve or characteristic. The ideal p-n junction I- V characteristic (figure 2.1.6) shows an exponential increase of the forward current and a constant negative value for the reverse current I_0. The reverse saturation current I_0 is related to the minority carriers n_{p0} thermally generated in the p- bulk region and p_{n0} generated in the n- bulk region [Neudek1983]. Moreover, the I_0 depends on T^3 and exponentially on the energy gap E_g [Sze 1981].

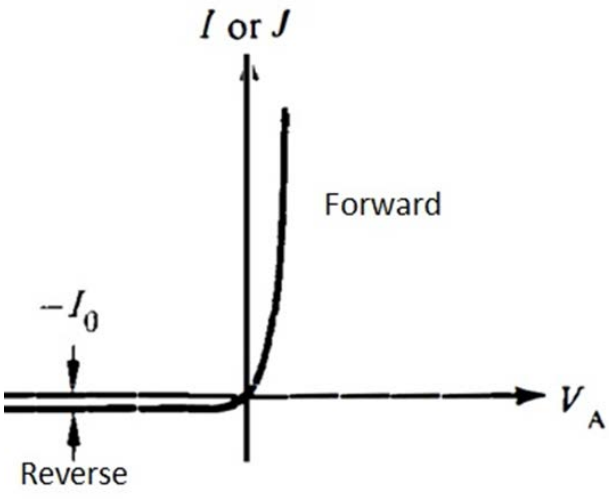

Figure 2.1.6: P-N junction ideal I or J- V characteristics [Neudek1983]

However, in several conditions of both reverse and forward applied voltage the ideal diode equation fails to adequately represent physical devices.

In reverse bias, the current becomes more negative than I_0 (figure 2.1.7) as a result of the carrier generation in the depletion region and, at even larger reverse voltages, due to junction breakdown [Neudek1983]. The voltage where the breakdown occurs is called breakdown voltage V_{BR} (figure 2.1.7), instead the current is called leakage current [Neudek1983], [Baliga 2008].

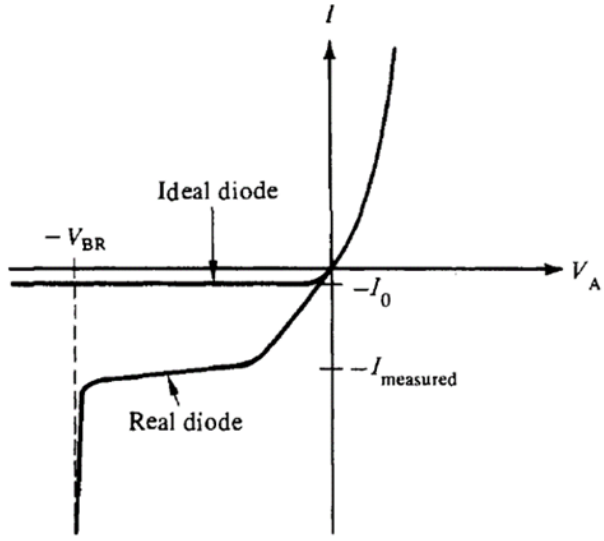

Figure 2.1.7: Reverse biased real diode [Neudek1983]

The carrier generation in the depletion region produces a current $I_{G\text{-}R}$ in excess through the diode [Neudek1983]:

$$I_{G\text{-}R} = -A\, q\, W\, n_i\, (2\, \tau_0)^{-1} \qquad (2.1.13)$$

where q is the charge, A junction area, W the depletion region width, n_i the intrinsic carrier concentration of the semiconductor and τ_0 the effective carrier lifetime or space- charge lifetime which is given by following equation [Baliga2008]:

$$\tau_0 = \tau_{p0}\, e^{[(E_T - E_I)/kT]} + \tau_{n0}\, e^{[-(E_T - E_I)/kT]} \qquad (2.1.14)$$

where E_T is the trap center energy within the semiconductor band gap, E_I is the intrinsic Fermi level energy, T the temperature. The τ_{p0} and τ_{n0} are the

minority carrier lifetimes in doped n-type and p-type semiconductor, respectively, and they are given by following equation [Baliga2008]:

$$\tau_{p0} = (C_p N_T)^{-1} = (v_{Tp} \sigma_{cp} N_T)^{-1} \quad (2.1.15)$$

$$\tau_{n0} = (C_n N_T)^{-1} = (v_{Tn} \sigma_{cn} N_T)^{-1} \quad (2.1.16)$$

where C_p and C_n are the hole and electron capture rate, respectively; v_{Tp} and v_{Tn} are the hole and electron thermal velocity, respectively; σ_{cp} and σ_{cn} are the hole and electron capture cross section, respectively, and N_T is the recombination centers density [Baliga2008]. Large value of τ_0 allow to reduce the generation leakage current [Baliga2008], [Neudek1983].

The reverse current increase at large V_A is mainly due to the avalanche and Zener breakdown. The former is related to the electric field in the depletion region and to the thermally generated minority carriers. At the critical electric field, the carriers accelerate to a large enough energy that when they collide with an atom in the crystal lattice an electron in the valence band is excited to the conduction band. All the “free” carriers gain kinetic energy, and participate to the electron-hole pairs generation by collisions: an avalanche of carriers takes place. Instead, the Zener process occurs in p-n junctions heavily doped on both sides (high N_A and N_D). In this condition the depletion region width W is very small and the conduction band edge on the n- side (E_{cn}) drops below the valence band edge on the p- side (E_{vp}), providing empty states in the conduction band of the n- material into which electrons may tunnel (figure 2.1.8) [Neudek1983].

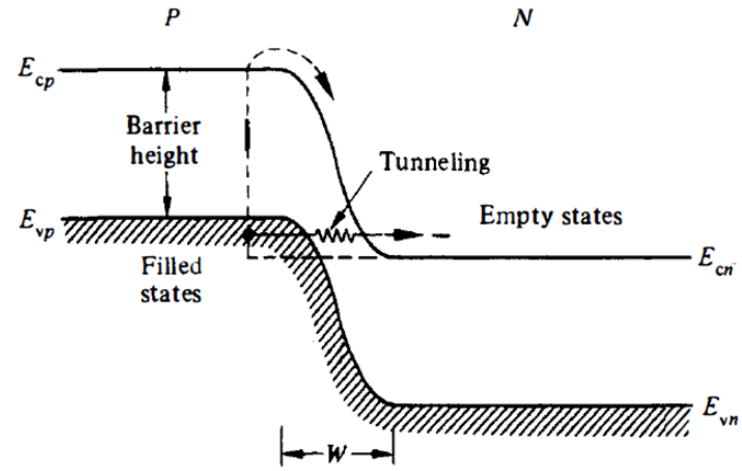

Figure 2.1.8: Reverse biased Zener breakdown in a p-n junction [Neudek1983]

The figure 2.1.9 shows a comparison between the breakdown voltage as a function of the doping concentration for silicon and 4H- SiC. It can be seen that the breakdown voltage decreases with increasing doping concentration in both materials. However, at fixed doping concentration, the 4H-SiC can support higher voltage than the silicon; the ratio of the breakdown voltage in 4H-SiC to that in silicon is found to be 67.4 [Baliga 2008].

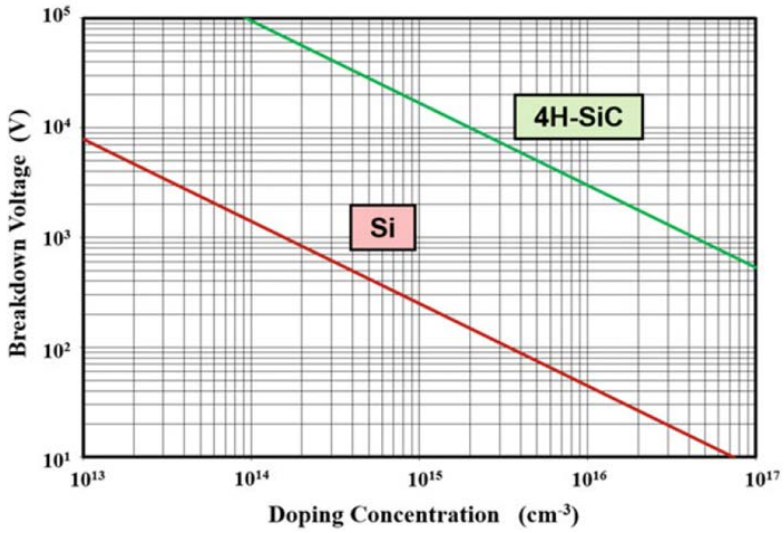

Figure 2.1.9: Breakdown voltage for silicon and 4H-SiC [Baliga 2008]

The deviations from the ideal diode under forward bias (figure 2.1.10) occurs at low applied voltage V_A due to the carrier recombination in the depletion region and, at high applied voltage V_A, mainly due to two effects: high-level carrier injection and ohmic voltage drops in the bulk regions and contacts; these two last effects are related to the electrical resistance of the system, called series resistance R_S [Neudek1983].

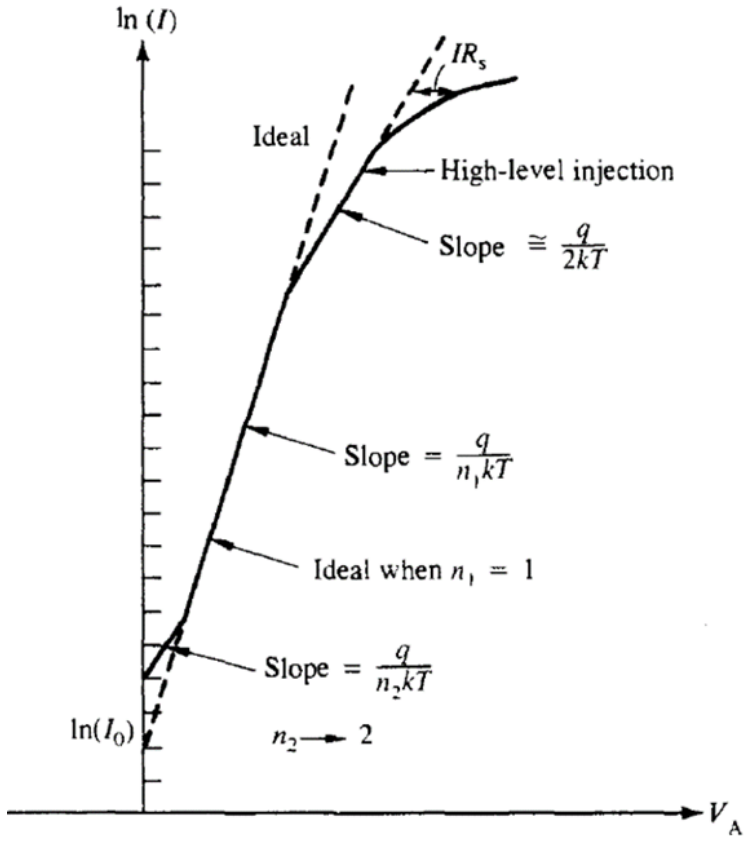

Figure 2.1.10: Semi-logarithmic I-V characteristic for a forward biased diode [Neudek1983]

At low forward current, the injected carrier densities are relatively small and holes leaving the p- region, travel through the depletion region W, to be injected as minority carriers into the n-region. Simultaneously, the electrons are traveling in opposite direction.

When the carrier number is greater than their thermal equilibrium value, recombination in the depletion region can occur in order to restore the equilibrium condition, each recombination event removes an electron- hole pair. In particular, the recombination is caused by recombination centers with an energy located deeply in the band gap (near the middle of band gap) as it is described by Shockley- Hall- Read (SHR) theory [Shockley1952] and by the model reported by C.T. Sah et al. in 1957 [Sah1957].

Instead, high level injection can occur when the excess minority carrier concentration approaches the majority carrier concentration in both side of the junction, and the drift and diffusion current component must be considered [Neudek1983], [Baliga2008].

The recombination and high levels injection effects result in a total current deviation than that predicted by the ideal diode equation (figure 2.1.10).

The total current for a real diode is the following [Neudek1983]:

$$I = I_0 \left(e^{qV_A/n_1kT} - 1\right) + A\,q\,W\,n_i\,(2\,\tau_0)^{-1}\left(e^{qV_A/n_2kT} - 1\right) \qquad (2.1.17)$$

where the first term is related to the ideal diode equation, the current flows mainly by means of diffusion mechanism, while the second term is related to the generation-recombination effect and it dominates at low level current. The parameter $n_1 = 1$ in the ideal case while $n_1 \geq 1$ in the other case, at large current levels when the high- level injection dominates the current flow $n_1 = 2$. Instead, the parameter $n_2 \approx 2$ at low current levels when the recombination dominates (figure 2.1.10) [Neudek1983].

At large current levels, the bulk semiconductor resistance and the metal-semiconductor contacts can produce a significant voltage drop, usually these two effects are combined into a resistor R_S (series resistance) in series with the diode. The current in a real diode with a series resistance R_S is given by equation 2.1.17 replacing the V_A with $V- IR_S$ [Shroder2006].

A third mechanism that contributes to the forward current flow and produces an “excess current” and, thus, a shunt paths in the real diode is the

tunneling [Sze1981]: the carriers tunnel through the junction by way of multiple energy states present within energy band gap [Sze1981].
The tunnel process adds a current term I_{sh} to the equation 2.1.17 which is given by the following relation [Pezzimenti 2017], [Sze1981]:

$$I_{sh} = I_t \, (e^{BV_A}) \tag{2.1.18}$$

Where B is fitting parameter and I_t is the saturation current for tunneling, it is related to the tunneling probability and it is inversely proportional to the square root of semiconductor energy band gap [Sze1981].
If the applied voltage V_A is higher than kT/q (k the Boltzman constant, T temperature and q the charge) the equation 2.1.17 can be simplified by using the following empirical equation [Nipoti2018] [Neudek1983], [Sze1981]:

$$I = I_0 \, (e^{qV_A/nkT}) \tag{2.1.19}$$

Taking the natural logarithm of the equation (2.1.19) [Neudek1983]:

$$\ln I = \ln I_0 + qV_A \, (nkT)^{-1} \tag{2.1.20}$$

The parameter n is called ideality factor: if n = 1 the diffusion current dominates (ideal diode case), instead, when n = 2 the recombination mechanism dominates [Nipoti2018], [Sze1981]. For $1 < n < 2$ both diffusion and recombination contribute to the total current [Sze1981]. The saturation current I_0 (equation 2.1.19) is related to the depletion region width W and to the effective carrier lifetime τ_0 trough to the following relation [Neudek1983], [Sze1981], [Sah1957]:

$$I_0 = A \, q \, W \, n_i \, (2 \, \tau_0)^{-1} \tag{2.1.21}$$

Where τ_0 is related to the trap concentration N_T by means of equations 2.1.15 and 2.1.16 [Baliga2008]. Moreover, the saturation current density J_0

(ratio between I_0 and the junction area A) can be related to the thermal activation energy E_a of the recombination centers [Strel'chuk2001]:

$$J_0 = J^*_0 \, e^{(-E_a/kT)} \tag{2.1.22}$$

$$\ln J_0 = \ln J^*_0 - E_a \, (kT)^{-1} \tag{2.1.23}$$

where T is the absolute temperature, k the Boltzman constant, the pre exponential factor J^*_0, at room temperature, is in the range 10^4-10^6 A·cm^{-2} when n = 2 [Strel'chuk2001] and it is proportional to $T^{5/2}$ [Li2005]; the activation energy E_a is related to the band gap width E_g and to the energy defects E_t located within the band gap [Sah1957]:

$$E_a = -\frac{1}{2} E_g \pm (E_t - E_i) \tag{2.1.24}$$

where E_i is the intrinsic Fermi level energy [Sah1957]. The main contribution to the saturation current is given by the recombination deep level located near the middle of the semiconductor band gap [Sah1957], [Strel'chuk2001].

2.2 Main 4H- SiC based devices

The simpler unipolar SiC based device is the Schottky barrier diode (SBD). It is a rectifying metal– semiconductor contact whose band diagram is illustrated in figure 2.2.1 where E_{VAC} is the vacuum level, Φ_M is the metal work function, χ is the electron affinity of the semiconductor, Φ_B is the barrier height for electrons, and ψ_{BI} is the built- in potential of the junction. In a Schottky contact, the Fermi level position near the middle of the semiconductor bandgap creates a barrier to carrier injection from the metal into either band of the semiconductor, so the current can only flow by the injection of majority carriers from the semiconductor into the metal [Kimoto2014], [Baliga2008]. The current flow in the SBD is related exponentially to the Φ_B which depends from the metal; for example, it is

equal to 1.6- 1.7 V or 1.73- 1.8 V for the Ni/SiC and Au/SiC Shottcky contact, respectively [Kimoto2014].

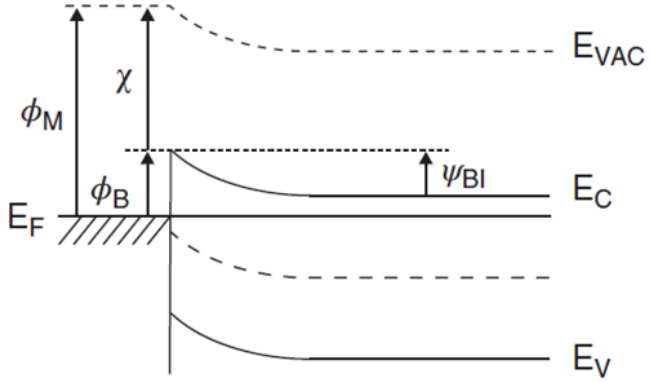

Figure 2.2.1: Band diagram of a Schottky diode on an n-type semiconductor [Kimoto2014].

The most important advantage of the SBD is the lack of minority carrier injection, leading to a very fast turn-off and low switching energy. However, high reverse leakage current, due to thermoionic field emission of carriers from the metal into the semiconductor, can lead to not negligible off- state power dissipation [Kimoto2014].

An important unipolar device is also the MOSFET (Metal Oxide Semiconductor Field Effect Transistor), and in figure 2.2.2 is shown the structure of an p- type 4H-SiC based MOSFET [Kimoto2014]. The gate generally is a metal; the gate, source and drain voltages are V_G, V_S and V_D, respectively. The channel length L is the region between the two n^+ bags [Kimoto2014]. The drain current I_D, flowing only along the y-direction in the channel, includes both drift and diffusion current components. The increasing source- drain voltage V_{SD} (equal to V_D-V_S) produces a shrinkage in the inversion layer (a layer with an electron density per unit volume equal to the density of holes per unit volume in the bulk [Kimoto2014]) near the drain and eventually pinches off. At the voltage at which this occurs $V_{D,\,SAT}$,

the drain current I_D saturates at the pinch-off value [Kimoto2014], [Baliga2008].

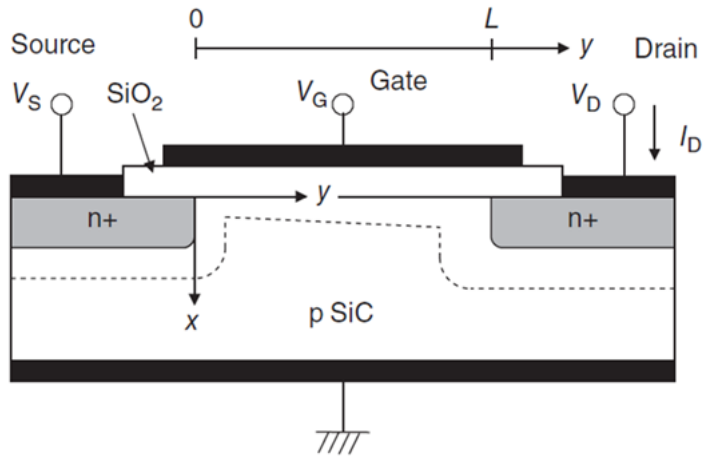

Figure 2.2.2: Structure of the basic MOSFET [Kimoto2014].

The MOSFET is at the base of power switch and applications in motor control and solar inverter [Kimoto2014], [Baliga2008]. However, in a power MOSFETs, the on-state resistance of the channel increases very rapidly with increasing the breakdown voltage. The resulting high conduction losses degrade the overall system efficiency [Baliga2008].

In recognition of these issues, the bipolar power devices such as BJT (Bipolar Junction Transistors, figure 2.2.3 a) and IGBT (Insulated- Gate Bipolar Transistors, figure 2.2.3 b) are developed. Both these bipolar devices are based on the p-n junction and for their properties such as high power gain and tailored switching speed are more promising for power electronic application [Kimoto2014], [Baliga2008].

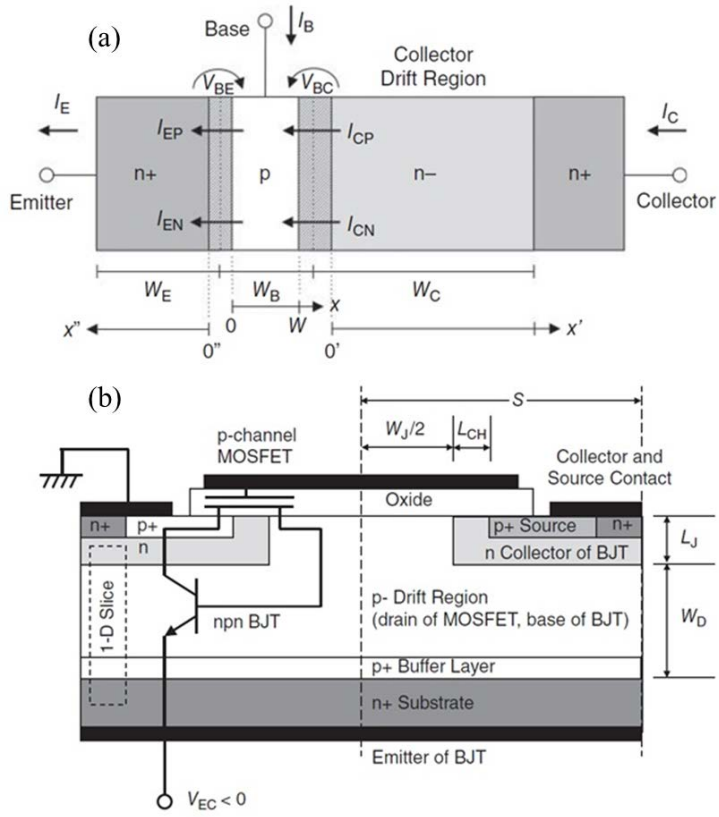

Figure 2.2.3: (a) Basic structure of an n^+/ p / n^- BJT and (b) Cross-section of a p-channel IGBT in 4H-SiC [Kimoto2014]

In the BJT (figure 2.2.3 a) the emitter is more doped than the base which is more doped than the collector ($N_{DE} \gg N_{AB} \gg N_{DC}$). We can identify four internal junction currents: hole and electron currents crossing the emitter–base (EB) junction (I_{EP} and I_{EN}) and the hole and electron currents crossing the collector– base (CB) junction (I_{CP} and I_{CN}) where the subscript index N and P indicate the electron and hole, respectively. Voltages V_{BE} and V_{BC} are developed across the junction depletion regions. Instead, the widths of the emitter, base, collector and neutral portion of the base are W_E, W_B, W_C and W, respectively. The terminal currents I_E, I_B, and I_C, each of them given by the sum of the current related to the electron and to the hole, are mainly related to the performance parameters such as current gain and specific on-

resistance [Kimoto2014]. In particular, the common- emitter current gain β (the ratio between the collector and base current) decrease by increasing the base current due to the increase in the hole diffusion from base to emitter under forward bias conditions at high current level [Kimoto2014].

The 4H-SiC BJTs are particularly attractive for high-temperature applications, since they are not dependent on the gate oxide properties.

The p channel 4H-SiC IGBT (figure 2.2.3 b) can be viewed as a p- channel MOSFET that supplies base current to an internal n/p/n BJT where the n^+ substrate acting as emitter and the p^- drift region acting as the base.

The most important characteristic of IGBT is that of switching [Kimoto2014]: in the conducting state, the current flows through the p-channel of the MOSFET, then through the forward- biased n^-/p^+ diode into the substrate. The thick n- base of the p/n/p BJT is in high-level injection condition (i.e. the minority carrier density exceeds the doping density), resulting in conductivity modulation that reduces the voltage drop across this region and, thus, the drift region resistance. The penalty to pay is the additional forward diode drops across the n^-/p^+ junction and a significant increase in turn off time, due to the minority carriers that must be removed from the base during turn- off, occurs. Moreover, the power dissipation during the switching event (switching dissipation) is proportional to the frequency of switching events and the energy dissipated per event [Kimoto2014]. To improve the switching properties and to reduce the turn off time, a p^+ buffer layer, also called field- stop layer [Baliga 2008], is placed between the p^- drift region and n^+ substrate; this layer produces a graded variation of the electric field which tends to zero into the buffer layer due to its high doping concentration [Baliga 2008], [Kimoto2014].

2.3 Radiation damage in 4H-SiC based device

Semiconductor devices operate often in radiation environment such as space, terrestrial, nuclear experiments and processing induced radiation. The electronic components exposed to radiation can be modified, resulting in a temporary or permanent failure of the electronic systems [Claeys2002]. To this end it is important to understanding the basic physical mechanisms of defect formation, their thermal stability, their effects on the material electric properties [Izzo2008].

Several literature studies report about the irradiation effects of different ions such as helium, proton, carbon and electron on SiC based devices such as Schottky junction, MOSFET and BJT [Izzo2008], [Luo2003], [Usmann2010], [Hallen2010], [Omotoso2018], [Luo2004].

It has been reported that irradiation with 7 MeV C^+ ion, at fluences Φ ranging between 10^9 and 10^{10} ion/cm^2, produces a reduction in forward current of Schottky Ni_2Si/ 4H-SiC junction based on two different epilayer donor concentration (N_d): $5x10^{14}$ cm^{-3} (figure 2.3.1a) and $7x10^{15}$ cm^{-3} (figure 2.3.1b). Both forward I-V curves show a smaller linear region and a current decrease with the increase of fluence that it is larger for the lower doped samples [Izzo2008]. This effect is related to the increase of series resistance, due to the substrate, epilayer and ohmic back contact resistances, because to a decrease in both dopant concentration and mobility [Izzo2009], [Izzo2008]. In particular, the reduction in free carrier concentration induced by ion irradiation in nitrogen doped 4H-SiC, also called compensation effect, is widely reported in literature [Aberg2001]. The nitrogen deactivation is caused by passivation of the nitrogen donor when combined with a point defect; the main candidates for dopant deactivation are the silicon vacancy and interstitial [Aberg2001] and the irradiation induced defects such as $R_{1/2}$ and R_4 [Izzo2008], [Izzo2009], already described in the

paragraph 1.3. Similar effects are observed also in 1.0 MeV Si^{+}- irradiated 4H- SiC Schottky diode [Roccaforte 2006].

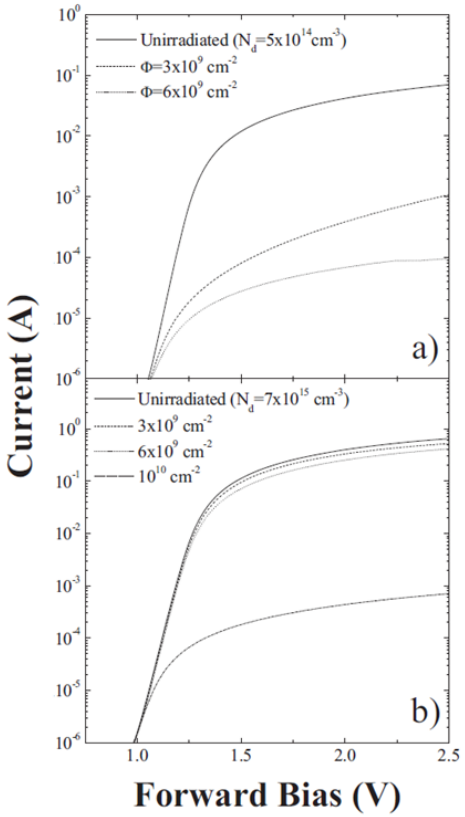

Figure 2.3.1: Forward I-V characteristics of 4H-SiC Schottky diodes before and after irradiation. The epilayers doping N_d is (a) 5.0 x 10^{14} cm^{-3} and 7.0x10^{15} cm^{-3} [Izzo2008]

The free carrier reduction (n) can be related to the ion irradiation fluence (Φ) by means of the follow empirical relation introduced by Paese et al. [Paese1987] and valid in the low fluence range [C. Claeys2002], [Hazdra2019]:

$$n = n_0 - K_n \phi \qquad (2.3.1)$$

Where n_0 are the carrier concentration of unirradiated sample and K_n is called carrier removal rate [C. Claeys2002] or carrier reduction efficiency.

The irradiation effects on more complex SiC based devices such as MOSFET [Lebedev2019], [Alexandreu2014] and BJT [Usmann2010], [Hallen2010] and are also discussed in literature.

A degradation in the electric performance is observed in the 4H- SiC MOSFET irradiated with high energy proton and electron [Lebedev2019], [Alexandreu2014]. The 15 MeV proton irradiation produces a decrease in the drain current I_d with increasing the irradiation fluence Φ, except for the irradiation fluence of 10^{13} ion/cm^2 (figure 2.3.2) [Lebedev2019]. The non-monotonic dependence between I_d and Φ is observed for both proton [Lebedev2019] and electron [Alexandreu2014] irradiated 4H-SiC MOSFET and it is caused by the trap centers in the gate oxide as well as in the channel-oxide interface [Alexandreu2014]. Instead, the irradiation induced deep levels such as $Z_{1/2}$, described in the paragraph 1.3, produce an increase in the drain- source resistance [Lebedev2019].

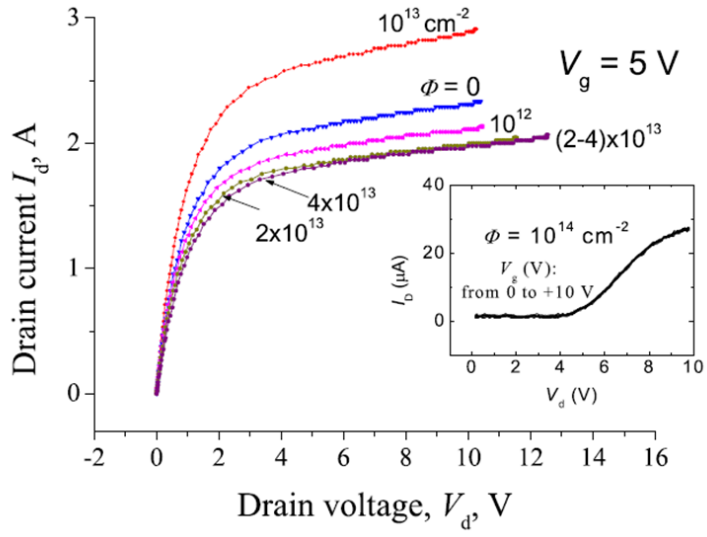

Figure 2.3.2: Drain I-V curve in the 15 MeV proton irradiated 4H-SiC MOSFET at different fluence Φ (gate voltage fixed at 5V) [Lebedev2019]

Both 3 MeV He ion [Usmann2010] and 2.3 MeV proton [Hallen2010] irradiation (fluence range 10^{10} – 10^{11} ion/cm^2 and 10^9 - 10^{12} ion/cm^2,

respectively) affect the electric properties of 4H-SiC BJT: it is observed a decrease in the collector current I_C with increasing the radiation fluence as shown in the figure 2.3.3 for the 3 MeV He irradiated 4H-SiC BJT [Usmann2010]. The I_C decrease is mainly due to the crystal damage which produces a decrease in the minority carrier lifetime and an increase in the resistance due to doping compensation [Usmann2010], [Hallen2010]. In particular, the trap centers within the semiconductor bandgap due to the irradiation induced defects (described in the paragraph1.3) can remove the electrons injected from the emitter into the base by means of recombination events, preventing them from contributing to collector current. This effect produces a decrease in the current gain β and an increase in the resistance due to doping compensation for the carriers flowing through the collector [Kimoto2014], [Usmann2010], [Hallen2010].

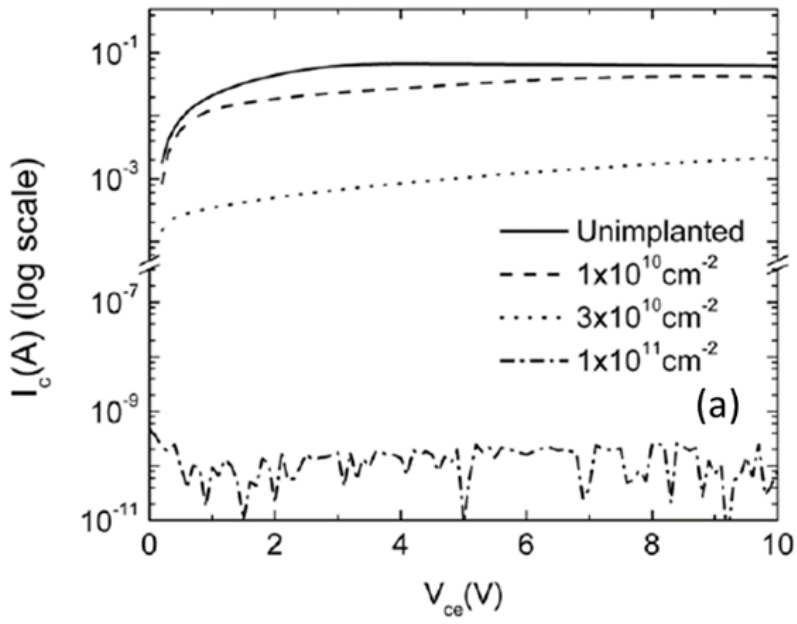

Figure 2.3.3: Collector current I_c versus collector–emitter voltage V_{ce} characteristics of unirradiated and 3 MeV He irradiated 4H- SiC BJTs at different ion fluence [Usmann2010].

As reported in literature, the ion irradiation affects the current flowing in the devices. The current decrease and, thus, the increase in the electrical resistance is induced by irradiation in different kinds of devices such as Schottky diode, MOSFET and BJT. These effects are mainly related to the reduction in free carrier concentration due to the passivation of the donor atoms when combined with the irradiation induced point defects such as $Z_{1/2}$, $R_{1/2}$ and R_4 (described in detail in the paragraph 1.3). These defects act as recombination centers and can remove carriers by means of recombination events. Moreover, as evidenced by Paese et al. the carrier reduction is fluence dependent.

In literature, there are not so extensive studies on 4H- SiC p-n junction diodes and on the correlation between the defects and electrical properties of ion irradiated bipolar devices.

Our study on simple 4H- SiC p-n junctions irradiated with high- energy He^+ ions allows us to examine and to understand the physical phenomena involved in a basic device. Moreover, the correlation between the ion irradiation induced defects and electrical performance of these devices can allow to understand the ion irradiation effect on more complex bipolar junction device such as, for example, BJT and IGBT.

Chapter 3

Material and methods

The main method to obtain p-n junction in SiC is the ion implantation that allows a precise impurity control [Neudek1983]. Usually, after implantation the sample is annealed in order to recover the ion induced damage and to activate the dopant.

In this thesis work, to study the effects of light ion irradiation on the simple 4H- SiC bipolar device as the p-n junction, devices were fabricated and then irradiated with He^{+} ions. The irradiation effects on the device electrical properties were studied by means of current- voltage (I- V) and capacitance-voltage (C- V) measurements. Instead, the radiation induced defects were investigated by DLTS technique.

In the present chapter the main techniques used in this Ph. D thesis for the fabrication of p-n junction devices, for they irradiation as well as for their characterization are described.

3.1 Device Processing

The used p- n junction devices were fabricated at CNR- IMM- Catania clean room facilities by using n- type 4H-SiC epitaxial layers (1.2 μm thick, 5 $x10^{17}$ donor/cm^3) grown by LPE (Luigi Preti Epitaxy) – Italy Silicon Carbide Epi Technologies on a n- type heavily doped ($1x10^{19}$ donor/cm^3) 4H-SiC 4” diameter substrate. The figure 3.1.1a shows a schematic (not in scale) cross section of the 4H-SiC p-n junction; the diode is laterally surrounded by a silicon dioxide layer. Instead, the top view picture of the device (anode contact) is shown in the figure 3.1.1 b; the devices are characterized by a circular geometry with a diameter of 1 mm (area = 0.8 x 10^{-2} cm^2).

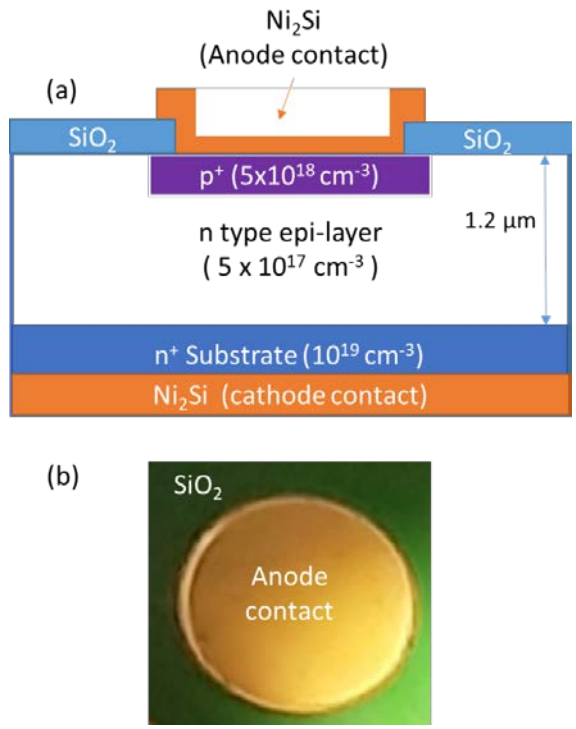

Figure 3.1.1: a) Schematic cross section of the 4H-SiC p-n junction (not in scale) and b) anode contact of the devices.

The formation of shallow p^+ region in the n- doped epitaxial layer (figure 3.1.1a) was performed by means of two consecutive Al^+ implantation processes at 400°C: 30 keV with fluence of 3 x 10^{13} ion/cm^2 and 80 keV with fluence 1x 10^{14} ion/cm^2. Thermal annealing process at 1700 °C for 30 minutes in Ar ambient was used to activate the dopant and to recover the implantation damage [Mazzillo2009], [Mazzillo2015], [Sciuto2015]. The p^+ formed region has a depth of about 0.175 µm and a dopant concentration, obtained by means of Hall effect measurements, of about 5x10^{18} cm^{-3} [Frazzetto2011], [Spera2019].

The Ni_2Si/ n^+ back ohmic contact (0.4 µm thick) was formed by means of the Ni sputter (0.2 µm thick) and, then, RTA process at 1000°C in N_2 ambient for 1 minute [Roccaforte2004].

For the front ohmic contact formation on p^+ side a Ni thin film (0.1 μm thick) was thermally evaporated after the optical lithography process used to define the contact region. The Ni_2Si front ohmic contact (0.2 μm thick) was obtained by means of RTA thermal process at 800°C in N_2 for 1 minute. [Konishi2003], [Roccaforte2004].

3.2 Post fabrication ion Irradiation

The ion irradiation consists in the introduction of charged particle into a material and it is adopted to study the effect of physical damage on the performance of the devices. The full knowledge of defect structure induced by neutron, electron or high energy light ions as helium [Usman2010] can allow to understand the effects on the electrical properties of SiC based devices such as the carrier lifetime and allowing the control of the turn-off time.

Typically, energetic particles, when penetrating through a material, decelerate and the transferred energy can modify material structure and properties. In the case of crystalline semiconductors, the particle-induced materials modification, known as radiation damage, occurs as long as the projectile particles have an energy, E, larger than the displacement energy, E_d [Auret 2004] (energy required to move an atom from its lattice site [Was2007]). The transfer of kinetic energy to the lattice atom gives birth to a knock-on atoms (PKAs) with the subsequent displacement of the atoms from their lattice sites [Was2007].

The incoming particle energy loss per unit length $(dE/dx)_{tot}$ (equation 3.2.1) mainly depends on the target atom density, N, and on the stopping power [Was2007] S, measured in $eV \cdot cm^2$ and defined as the energy loss by a projectile ion moving through a differential thickness dx of a target material of unit density [Was2007], [Nastasi2006]. The stopping power S is given by the sum between the energy loss due to the elastic interaction with the

target nuclei (nuclear stopping power, S_n) and the energy loss due to the inelastic collision with the target electron (electronic stopping power, S_e) [Was2007], [Nastasi2006], [Auret 2004].

$$- (dE/dx)_{tot} = N\,S = N\,(S_n + S_e) \qquad (3.2.1)$$

In figure 3.2.1 is shown the nuclear and electronic energy loss as a function of square root of particle energy E. For light charged particles such as proton or He- ion, the nuclear stopping is the dominant mechanism for particle energy in the keV range; instead, the electron stopping is dominant for energy of MeV [Auret 2004], [Nastasi2006], [Was2007].

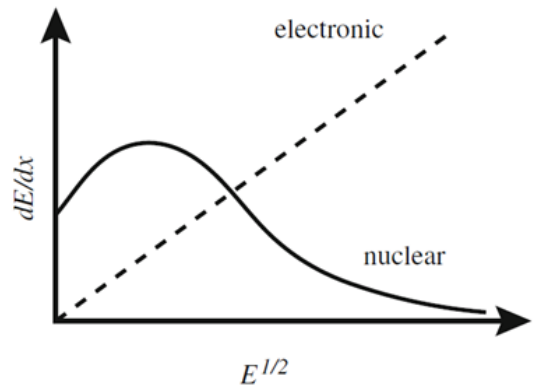

Figure 3.2.1: Energy loss as a function of particle energy square root [Wasa2007]

The ion path into the material is random as shown in figure 3.2.2 [Nastasi2006] where R is the total distance of the ion into the target material and the R_p, projected range, is the projection of the total range R on the initial direction of the particle path [Was2007].

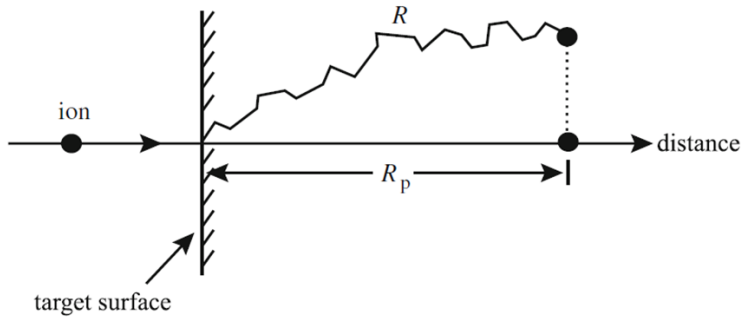

Figure 3.2.2: Total path length R and projected range R_p for an ion incident on a target material [Was2007]

The incident particles N into the material has a Gaussian distribution [Was2007]:

$$N(x) = N_p \, e^{-(x - R_p)^2 / 2 (\Delta R_p)^2} \qquad (3.2.2)$$

where N_p is the concentration of the projectile ions at R_p (projected range) and ΔR_p is the R_p standard deviation or straggling. It is related to the ion energy and to the ratio between the masses of the irradiated ions and the target material atoms [Was2007].

The main effects of ion irradiation in semiconductor are: 1) ionization due to the electronic stopping (electron- hole pair generation) [Zeller1995], [Claeys2002], [Schwank2008] and 2) displacement damage due to the nuclear stopping (vacancies- interstitial pair production) [Messenger1992], [Claeys2002].

The ionization effect on the materials are mainly two: charge flow due to the ionization- induced conductivity and the buildup of the charges near the interface between dissimilar materials [Vanlint1971]. Instead, concerning the displacement damage, the generated vacancies are effective recombination and trapping centres which permanently affect the electric properties of the material. Furthermore, their diffusion produces the

vacancies and interstitials recombination or the formation of complex defects [Messenger1992], [Claeys2002].

One of the most important problems in the electronic device related to displacement damage is the charge carrier removal, i.e. a reduction in majority carrier density. It causes a decrease in carrier mobility and an increase in the material resistivity [Izzo2008], [Siemieniec2006].

The SiC p-n junctions analyzed in this Ph. D thesis were irradiated at room temperature with He^+ at 700 keV and fluences in the range 10^{12} - 10^{15} ion/cm^2. The goal was the study of fluence effects on the electrical properties of 4H- SiC p-n junctions. SRIM simulation [Ziegler 2013] of 700 keV He^+ in SiC shows a projected range of about 1.64 μm which is higher than the epitaxial layer thickness (1.2 μm); the ion energy was chosen in order to irradiate almost uniformly the epilayer. The figure 3.2.3 shows the single He^+ energy loss (black line) and induced vacancies distribution (red line) calculated by using SRIM software [Ziegler 2013]. At SiC epitaxial layer depth of 1.2 μm, the He^+ induces the formation about $1.5x10^5$ vacancies·cm^{-1} and the energy loss in elastic collision is 2.2×10^7 eV·cm^{-1}.

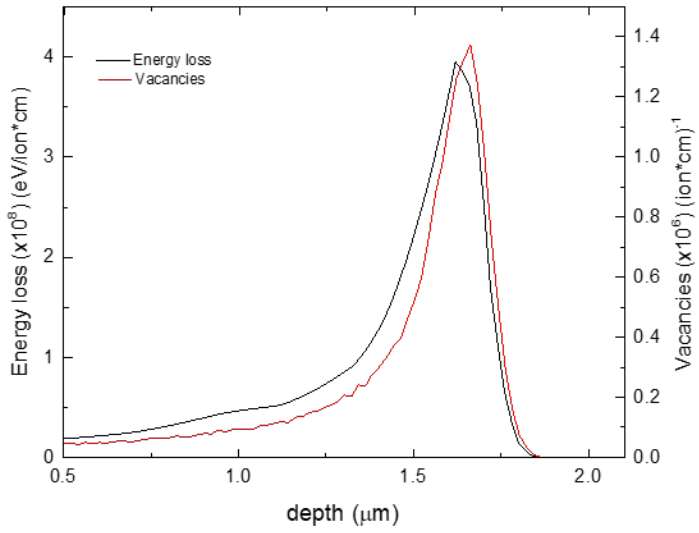

Figure 3.2.3: Energy loss and vacancies distribution obtained by SRIM simulation.

3.3 Analysis Techniques

The effects of irradiation on device electrical properties were investigated by using current-voltage (I-V) and capacitance-voltage (C-V) measurements: the former allows the study of the device electrical behavior, instead the C-V measurement allows to monitor the change in the donor concentration in the semiconductor as a function of irradiation fluence. The Deep Level Transient Spectroscopy (DLTS) was used to study the traps and recombination centers introduced by irradiation defects as well as their evolution.

3.3.1 Two-point probe electric measurements

The two point- probe electric measurement is an easy method for the study of the material and device electric properties and behavior. In two- point arrangement a bias V is applied to the ends of the sample and the current flowing is measured by ammeter connected in series with the sample and the generator. The curve of the current flowing through the sample as a function of the applied voltage is called current- voltage (I-V) curve or characteristic [Shroder2006].

To perform the I-V measurement two tips were connected to the front and back side of the sample as shown in figure 3.3.1: the device is mounted on a copper foil using silver paint. The back contact is then accessible approaching the probe tip on the copper foil front in a point near to the device. This solution was in particular adopted in order facilitate the mounting of the samples in the irradiation chamber and the back electrical contact in the DLTS apparatus (see paragraph 3.3.3).

Figure 3.3.1: Two- point probe measurement performed on the 4H-SiC p-n junction.

The electrical measurements in this Ph. D thesis were performed in a thermally controlled (in the range 300 ÷ 448 K) Kurl Susse probe station in dark condition by using a Keithley 2636B SMU (Source Meter Unit).
All diodes were characterized before and after irradiation with He^{+} ions.

3.3.2 C-V measurement

The capacitance- voltage measurements are an efficient method to obtain the carrier density in a Schottky or p-n junction structures. The method is based on the relation between the depletion region capacitance C and the reverse applied voltage V: differentiating the equation 2.1.4, it is possible to obtain the semiconductor donor or acceptor concentration N(W) [Sze1981], [Shroder2006]:

$$N(W) = 2\left[q\, K_S\, \varepsilon_0 \frac{d(A/C)^2}{dV}\right]^{-1} \qquad (3.3.1)$$

where A is the diode area, q the charge, K_S is the relative dielectric constant, ε_0 is the vacuum dielectric constant and W the depletion region [Shroder2006]:

$$W = K_S\, \varepsilon_0\, A\, (C)^{-1} \qquad (3.3.2)$$

The C- V measurement is a two- point probe technique: a reverse bias V is applied to the device through two metal tips. The diode capacitance is measured by a capacitance meter, usually an RC (Resistance- Capacitance) bridge circuit [Webster2004]. The curve of the depletion region capacitance C as a function of reverse applied voltage V is called capacitance- voltage (C-V) curve or characteristic [Webster2004], [Shroder2006].

The C- V measurements, at 100 KHz, in this thesis were made by using a Boonton 7200 capacitance meter contacting the samples in the thermally controlled probe station as yet described for the I-V characterization.

3.3.3 Deep Level Transient Spectroscopy (DLTS) technique

The most promising and very sensitive technique for the characterization and study of the deep and shallow levels, related to the point or point like defects, present within the crystalline semiconductor band gap is the Deep Level Transient Spectroscopy (DLTS), introduced by D. V. Lang in 1974 [Lang1974]. The technique uses the depletion region capacitance of a p-n or Schottky junction as a probe to monitor the changes in the trap centers charge state. The DLTS, based on a high-frequency (MHz range) capacitance transient thermal scanning method, is able to distinguish between majority and minority carrier traps and it provides information on the trap centers density, energy levels and capture rates.

The diode capacitance variation is produced by the application of a periodic reverse voltage followed by the carrier thermal emission as shown in figure 3.3.2 where N_D is the donor density in n- type semiconductor while n_T and p_T are the electron and hole occupied trap state density, respectively [Lang1974], [Shroder2006].

At the beginning the system is under the reverse bias voltage $-V_1$ (the traps in the depletion region are empty). The applied voltage change, from $-V_1$ to 0 V, produces a depletion region width W reduction and the diode

capacitance switches from its background value C_0 to the C (V=0); thus, the electrons are captured and fill the traps (figure 3.3.2 a). At the time t = 0 the reverse bias application – V_1 produces again an increase in the depletion region width W with the traps filled by the carriers. At the time t > 0, the carrier thermal emission from the trap centers within the semiconductor band gap (figure 3.3.2 b) produces a capacitance transient ΔC_e; as the electron are emitted from the traps to the conduction band, the capacitance C increases until the steady state is attained (the capacitance reaches its background value C_0) [Shroder2006], [Lang1974].

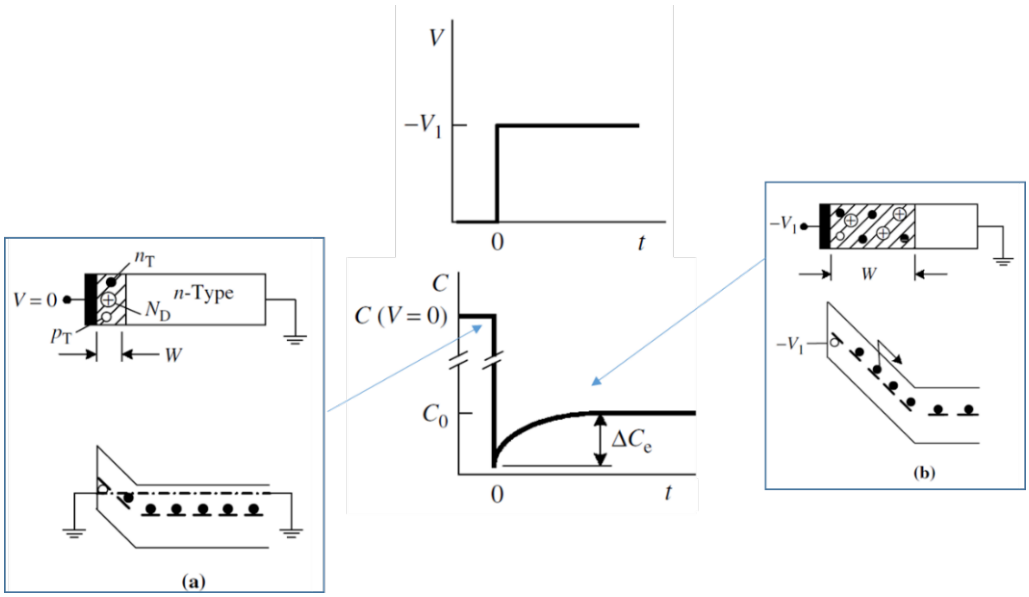

Figure 3.3.2: Diode capacitance variation as a function of the time: a) zero bias application at t < 0 and (b) reverse bias application at t > 0 [Shroder2006]

If the total trap center density N_T is very low, $N_T << N_D$, the capacitance transient ΔC_e is given by following equation [Shroder2006]:

$$\Delta C_e = C_0\,(2\,N_D)^{-1}\,N_T\,e^{-e_n t} \qquad (3.3.3)$$

Where e_n is the electron emission rate [Tin2012]:

$$\ln(e_n T^{-2}) = \ln[16\pi\, m_e^{*}\, k^2\, \sigma_n\, (gh^3)^{-1}] - \frac{E_C - E_T}{kT} \qquad (3.3.4)$$

where T is the absolute temperature, m_e^* is the electron effective mass in the conduction band, k the Boltzman constant, g the level degeneracy, σ_n the capture cross- section, h the Plank constant, E_C the conduction band energy and E_T the trap state energy. The σ_n and the e_n are the intrinsic properties of the deep level. An equation similar to the 3.3.4 is obtained also for the hole emission rate e_p [Kimoto2014].

If $t \rightarrow \infty$: $C = C\ (t \rightarrow \infty)$ the equation (3.3.3) become the following [Shroder2006]:

$$\Delta C_e = C_0\, (2\, N_D)^{-1}\, N_T \qquad (3.3.5)$$

The decaying capacitance transient ΔC_e measured at two different time delays t_1 and t_2 from the voltage pulse termination (rate windows technique), also called DLTS signal S and measured in pF, is given by following equation [Tin2012]:

$$S = \Delta C_e = C(t_1) - C(t_2) = C_0\, (2\, N_D)^{-1}\, N_T\, (\, - e^{-\, e_n\, t_1} + e^{-\, e_n\, t_2}\,) \qquad (3.3.6)$$

where $C\ (t_1)$ and $C(t_2)$ are the capacitance value at the time t_1 and t_2, respectively, C_0 is the background capacitance, e_n is the electron emission rate, N_T and N_D are the trap and donor concentration, respectively [Tin2012].

As the temperature T changes, the electron emission rate e_n and consequently the capacitance transient ΔC_e (equation 3.3.3) also change (figure 3.3.3). In particular, the time emission constant (inversely proportional to the e_n) at low temperature is longer, reflecting the low emission rate of the trapped electrons due to inadequate thermal energy necessary for the electrons to escape. As the temperature of the sample increases, the thermal energy required for excitation into the conduction

band increase; thus the time constant becomes shorter corresponding to a faster emission rate of the trapped electrons [Tin2012]. By monitoring the DLTS signal S as a function of the temperature T (DLTS spectrum, figure 3.3.3), it can be seen that at a low temperature and at high temperature the signal is very small. However, there are a temperature T_m where the DLTS signal will go through a maximum value due to the majority carrier emission from the trap centers. The position in temperature of the peak in the DLTS spectrum is uniquely determined by thermal emission properties of the trap centers [Lang1974].

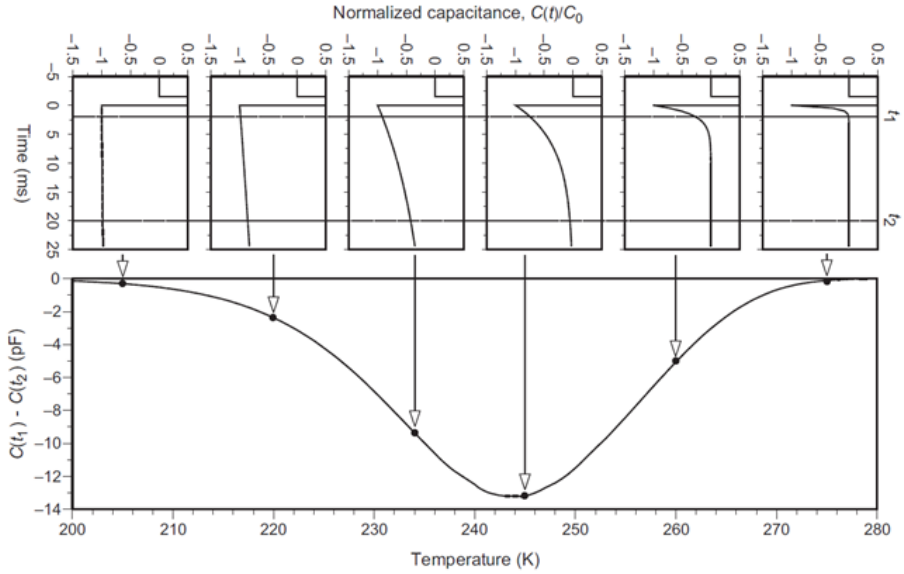

Figure 3.3.3: Graphic relation between the normalized device capacitance $C(t)/ C_0$ as a function of time t and the capacitance transient ΔC_e temperature dependence [Tin2012].

At the peak temperature T_m, the thermal emission rate e_n and the time delays t_1 and t_2 are related (equation 3.3.7) [Tin2012], [Lang1974]:

$$e_n = \ln(t_2/t_1)\,(t_2 - t_1)^{-1} \qquad (3.3.7)$$

By varying t_2 and t_1 but, for example, keeping its ratio constant and repeating the temperature scan, different spectra are obtained. The peak

temperature change (figure 3.3.6 a) and, thus, an Arrhenius plot (figure 3.3.6 b), ln (e_n/T^2) as a function of 1/T (equation 3.3.4), can be obtained. The electron trap energy E_T relative to the conduction band edge E_C is related to the Arrhenius plot slope and the electron capture cross section is given by the Arrenius plot y- intercept [Tin2012]. Instead, the trap concentration N_T is proportional to the DLTS spectrum peak height (equation 3.3.5) [Shroder2006].

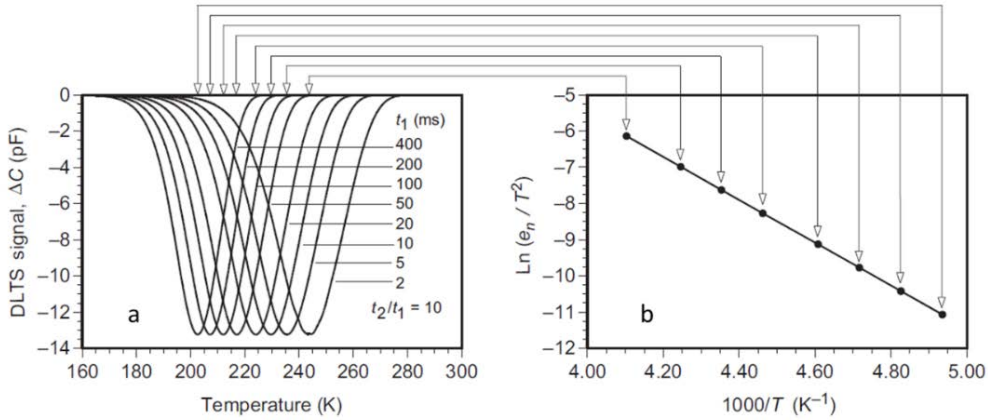

Figure 3.3.6: a) DLTS spectra peak at different time delay t_1 with a ratio t_2/t_1 equal to 10 and b) Arrhenius plot [Tin2012]

The DLTS measurements in this Ph. D thesis were performed by using a SULA double boxcar spectrometer. The working conditions are the following: the temperature range 150- 750 K, rate windows range 2- 23 s^{-1} and voltage range from -13 V to 0 V. The samples are cooled by means of the liquid N_2 and they are electrically connected by using two tungsten tips like in a two- point probe technique. The wide temperature range (150 K – 750 K) needs to detect the trap level in the wide band gap semiconductor such as SiC.

Chapter 4

4H-SiC p-n junction Characterization

This thesis chapter is focused on the effects of high- energy He^+ ions irradiation on 4H-SiC p-n junction. In a first chapter section we analyze the ion irradiation effects on the 4H-SiC p-n diodes as a function of the irradiation fluence by using current- voltage (I-V) and capacitance- voltage (C-V) measurements at room temperature. The changes induced in the electrical properties of the device are correlated to the variation in the 4H-SiC epilayer donor concentration obtained by C-V measurements and to irradiation defects measured by DLTS technique. In a second section of the chapter is discussed the temperature behavior of the p- n junction diodes. In particular, the study of the temperature effects on I-V characteristics allows the correlation of physical junction properties with the changes in the semiconductor properties induced by irradiation as well as to obtain more information about the defect structure in irradiated SiC.

4.1 Unirradiated diodes electrical behavior

All 4H-SiC p-n diodes were characterized before and after He^+ irradiation (whose fabrication is described in the chapter 3) by means of current-voltage (I-V), capacitance- voltage (C-V) and DLTS techniques.

The figure 4.1.1 shows the forward (figure 4.1.1a) and reverse (figure 4.1.1b) semi- logarithmic I-V characteristic of some typical unirradiated diodes. The I-V characteristics of unirradiated samples exhibit a reasonable current dispersion less than 5% around the typical trend, may be due to the presence of some processing defects. To overcome this effect each device was characterized before and after irradiation and its characteristics were

compared in order to discriminate the effects due to irradiation from the processing induced issues.

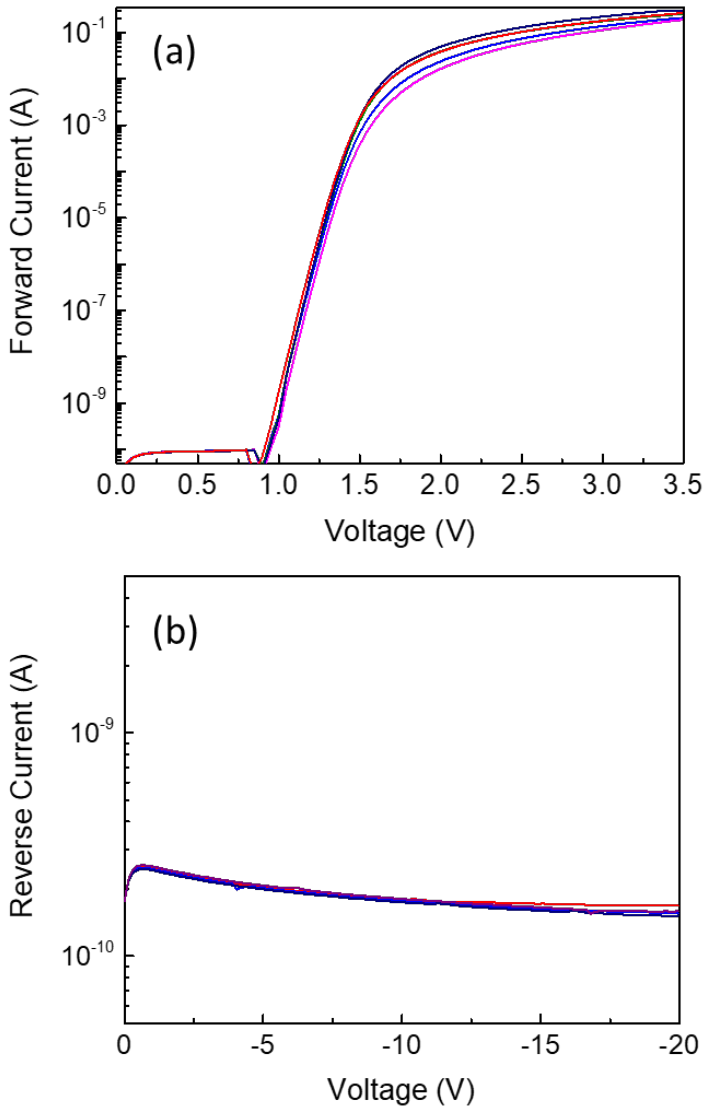

Figure 4.1.1: Unirradiated 4H-SiC p-n junction forward (a) and reverse (b) current – voltage (I-V) curves.

The forward I-V curves (figure 4.1.1a) exhibit the typical p-n junction behavior described in the chapter 2: an exponential increase of the current at low voltage (<1.5 V) mainly due to the diffusion and recombination processes, while at high voltage the current has a linear increase due to the

onset of the series resistance. The reverse I-V characteristics (Figure 4.1.1b) saturates at about 0.16 nA (saturation current density of about 20.3 nA/cm^2) for voltage up to -20V; the investigated voltage range is considered sufficient to monitor the effects of damage in the junction region avoiding the leakage contribute that will take place at higher voltage being absent any guard ring structure.

The experimental forward current- voltage curves were analyzed in the low voltage range by using the equation 2.1.20; the analysis gives the ideality factor n, related to the slope of the linear region in the semi- logarithmic I-V curve (dashed red line in the figure 4.1.2), and the saturation current I_0, related to the intercept at V = 0.

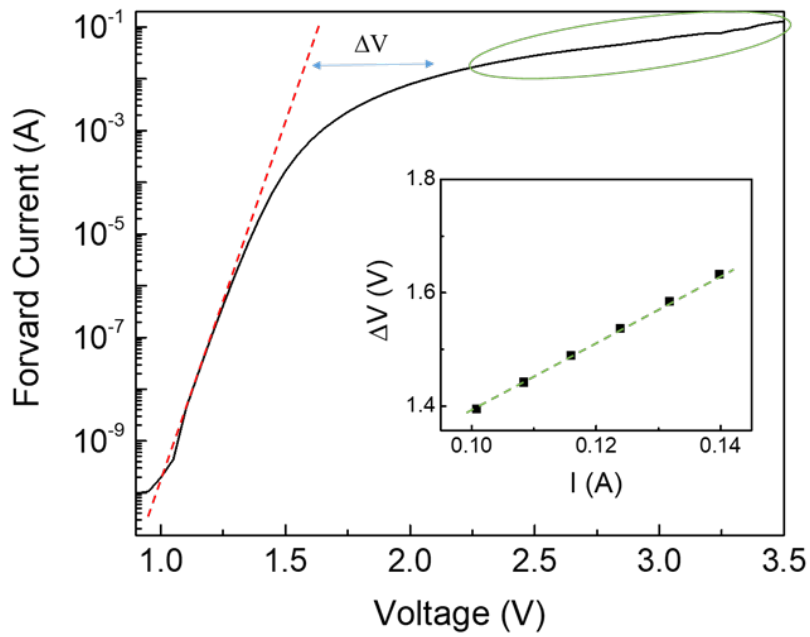

Figure 4.1.2: Typical unirradiated 4H-SiC p-n junction forward current-voltage (I-V) characteristics with analysis method scheme. (inset) ΔV- I linear plot versus the related current I (see text)

The series resistance R_S is obtained from the I-V curves saturation region at high voltage (green circle in the figure 4.1.2) where its contribution dominates the current flow. In particular, the series resistance R_s can be

determined by the slope of the ΔV- I linear plot (inset in the figure 4.1.2) where ΔV is the difference between the experimental and ideal voltage drop at fixed current value I extracted by the I-V curve at high voltage (green circle in the figure 4.1.2).

The obtained values of ideality factor, saturation current and series resistance are $n = 1.30 \pm 0.05$, $I_0 = (2.5 \pm 0.4) \times 10^{-23}$ A and $R_s = 5.84 \pm 0.05$ Ω, respectively.

The C-V characteristics of unirradiated samples are similar each other and in figure 4.1.3 is reported a typical curve (black line) and the related $(A/C)^2$ plot (red square) where A is the active diode area (0.8×10^{-2} cm^2). The donor concentration N_d of unirradiated samples, calculated from the $(A/C)^2$ plot slope by means of equation 3.3.1, is equal to $(7.5 \pm 0.1) \times 10^{17}$ cm^{-3} (close to the nominal epilayer concentration value of 5×10^{17} cm^{-3}). Moreover, the linearity of the $(A/C)^2$ plot (red square in the figure 4.1.3) indicates the uniform donor density distribution in the epilayer of the unirradiated 4H-SiC.

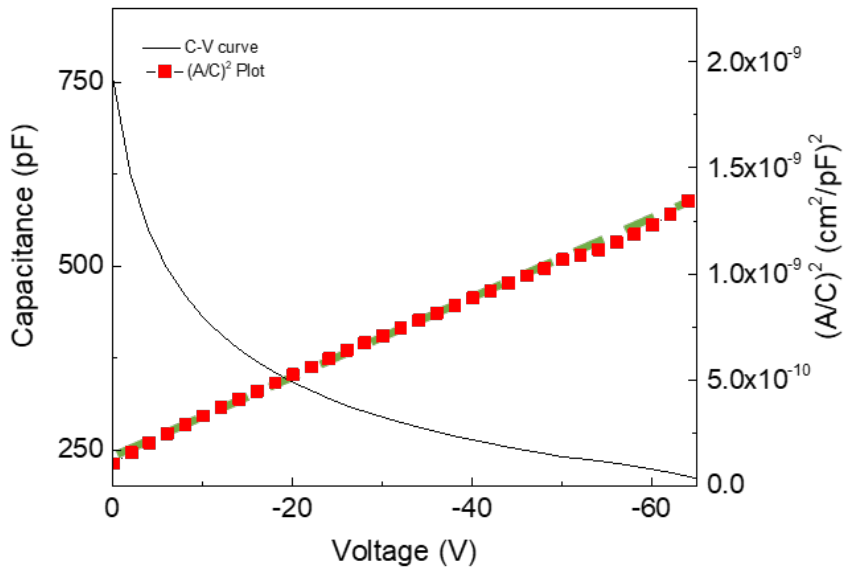

Figure 4.1.3: Unirradiated sample typical capacitance- voltage (C-V) curve (black line) and the $(A/C)^2$ plot (red square).

The DLTS analysis of unirradiated samples (figure 4.1.4) does not show the presence of peaks related to the point defects and, thus, deep level within the band gap. This means that the unirradiated samples have a very small concentration of processing defects, less than the DLTS sensitivity (< 10^{10} traps/cm^3).

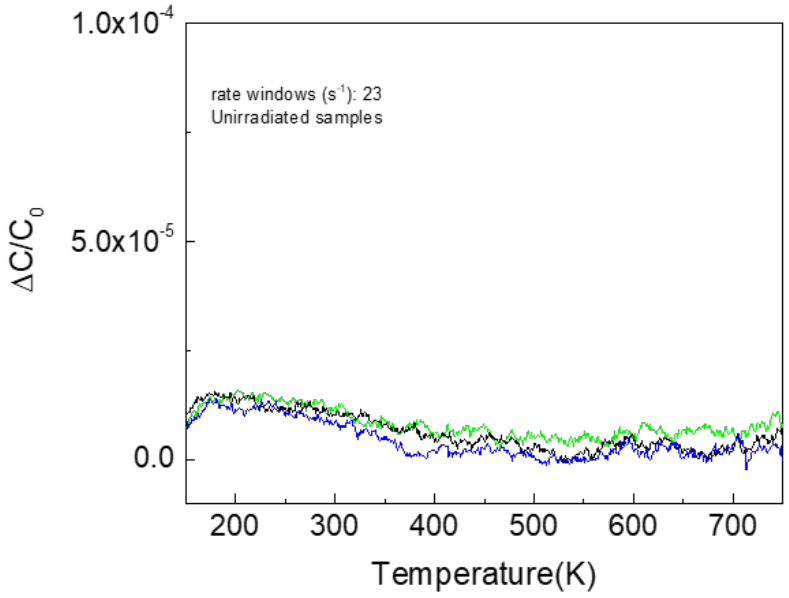

Figure 4.1.4: DLTS spectra of different unirradiated samples (rate windows: 23 s^{-1})

4.2 Room Temperature Characterization

After 700 keV He^+ irradiation at different fluences, the diodes were again characterized (at room temperature) in order to study the effects of the ion fluence on the electric behavior of the devices [Pellegrino2021].

The figure 4.2.1 shows the forward semi- logarithmic I-V characteristics of the p-n junction before (black line) and after He^+ irradiation in the fluence range 10^{12} ion/cm^2 (red line) - 10^{15} ion/cm^2 (orange line).

Relevant modifications are observable in the forward I-V characteristics after irradiation (figure 4.2.1). The irradiated diodes characteristics show a behavior similar to the one of unirradiated device (figure 4.2.1 black line);

however, in low voltage range the ion irradiation produces a variation in the linear region slope and in the intercept at V= 0 as well as a decrease in the current flow. The turn-on voltage varies from 1± 0.03 V obtained for the unirradiated and 10^{12} ion/cm^2 irradiated diodes to the value of 2 ± 0.1 V, obtained for the sample irradiated at 10^{15} ion/cm^2; moreover, a higher voltage shift of the entire characteristic is observed. The forward I-V characteristics in the high voltage range become flat and the current are entirely dominated by series resistances which increase by increasing the ion fluence [Pellegrino2021].

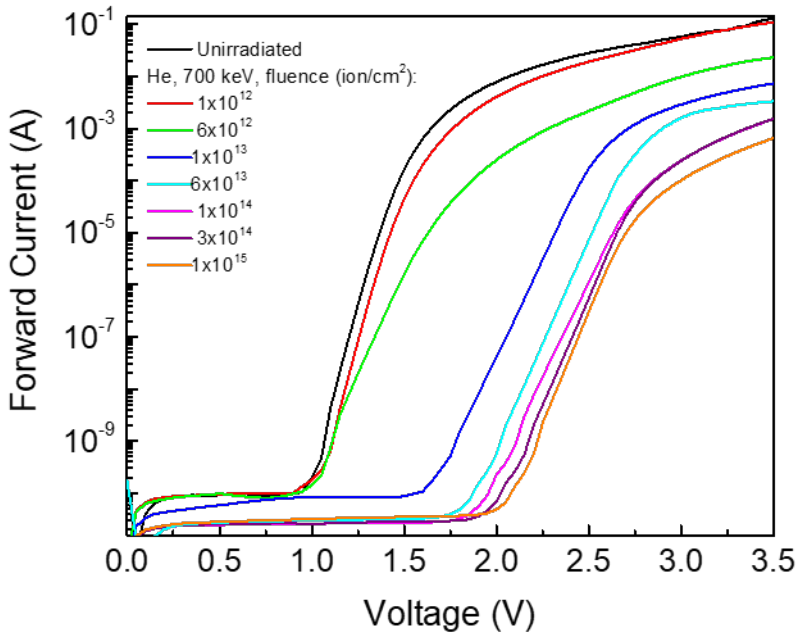

Figure 4.2.1: Forward semi- logarithmic current- voltage (I-V) curves of 4H-SiC p-n diodes before and after irradiation.

The reverse I-V characteristics (figure 4.2.2) do not show relevant changes after ion irradiation in the fluence range 10^{12} ion/cm^2 (red line) - 10^{13} ion/cm^2 (blue line) while at higher fluences (> 1x 10^{13} ion/cm^2) the reverse current decreases. The leakage current measured at -15 V decreases of about a factor 3 (figure 4.2.2 inset) [Pellegrino2021].

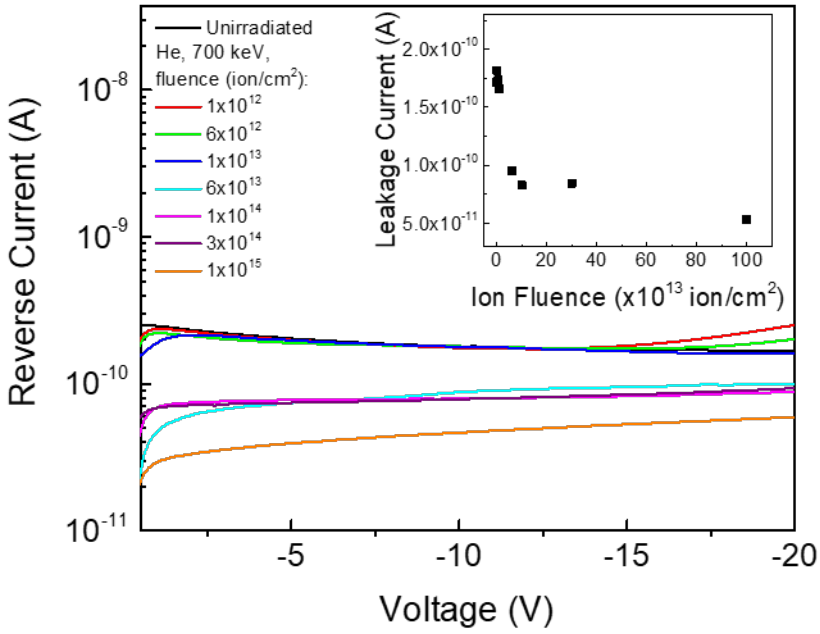

Figure 4.2.2: Reverse semi- logarithmic current- voltage (I-V) curves of 4H-SiC p-n diodes before and after irradiation. Leakage current @ -15V versus He^+ fluence (inset)

An important parameter in the I-V junction characteristics is the rectification ratio (RR ratio). It is defined as the ratio between the forward and reverse current at the same voltage and it gives the diode rectification efficiency [Sze1981], [Muhammad2018]. The RR ratio, calculated at ± 3.5 V (figure 4.2.3), is 5 x 10^8 in the unirradiated sample and it has a sharp decrease by increasing the irradiation fluence at 10^{13} ion/cm^2 (figure 4.2.3 inset); in the higher fluence range, the RR ratio continues to decrease reaching a value of 2 x 10^7. This trend evidences the degradation of diodes rectifying properties.

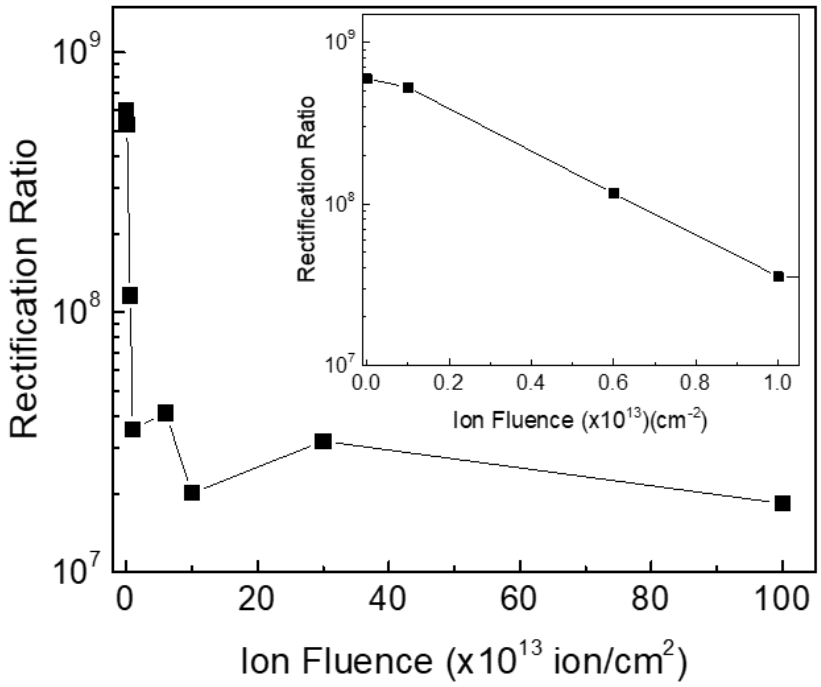

Figure 4.2.3: Rectification ratio (RR ratio) as a function of irradiation fluence in semi- logarithmic scale.

4.2.1 Carrier compensation

The decrease of forward current at high voltages in the I-V curves by increasing the irradiation fluence can be ascribed to the rise in the diode series resistance (R_S) induced by irradiation damage. The R_S values as a function of irradiation fluence are show in the figure 4.2.4. The resistance shows a sharp increase of about a factor 6 up to a fluence of 6×10^{12} ion/cm^2 passing from about 6 Ω to the value of 36 Ω (figure 4.2.4 inset). By increasing the irradiation fluence at 10^{15} ion/cm^2 the R_S continues to increase and it reaches the value of about 320 Ω, more than 50 times than the unirradiated devices [Pellegrino2021].

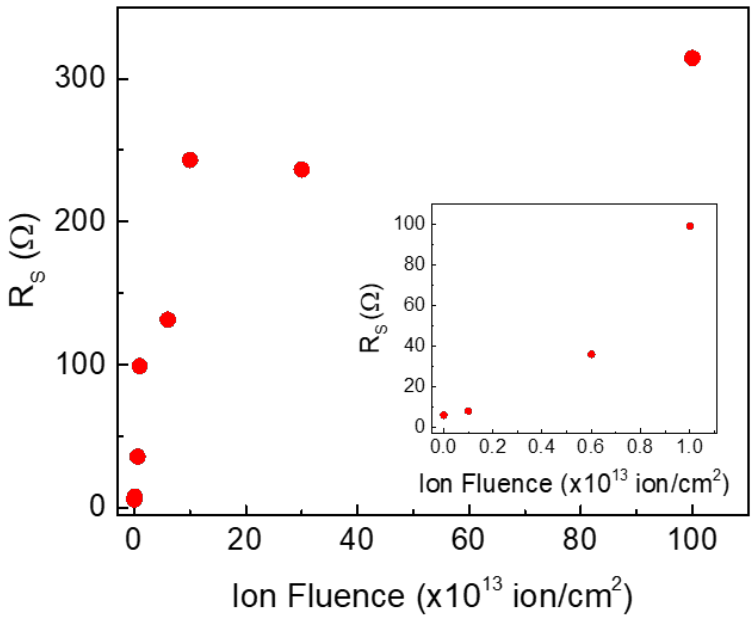

Figure 4.2.4: Series resistance (R_s) as a function of ion irradiation fluence. In inset the series resistance up to irradiation fluence of 10^{13} ion/cm^2

A similar effect is reported in literature for irradiation with neutron, proton and other types of ions in different kind of devices such as Schottky [Izzo2008], [Omotoso2018] and BJT [Usman2010], [Hallen2010] as well as p-n junction [Strel'chuk2017], [Moscatelli2007] and [Nipoti2018]. The series resistance increase is ascribed to the decrease of free carrier concentration (compensation effect) [Claeys2002], [Aberg2001]. The donors of n-type epitaxial layer are compensated by irradiation defects which exhibit acceptor- like behavior [Aberg2001], [Hazdra2014]. Nevertheless, it is worth noting that even the decrease of carrier mobility can be responsible for the increase of R_s [Izzo2008].

In order to study the correlation between R_s and the carrier concentration, the C-V measurements are performed.

The C-V characteristics in the voltage range 0 ÷ 80 V of unirradiated and irradiated devices in the fluence range 10^{12}- 10^{15} ion/cm^2 are shown in the figure 4.2.5. Typical trends of C-V curves are observed in the unirradiated

and irradiated diodes up to a fluence of 10^{13} ion/cm^2 while, at higher fluence ($\geq 10^{13}$ ion/cm^2, figure 4.2.5), the C-V curves are almost constant and independent on the applied voltage [Pellegrino2021]. Similar behavior of C-V characteristics has already been observed in the p-n junction irradiated with protons [Lebedev2000] and it was ascribed to the strong increase of diode series resistance R_s [LebedevJr 2000], [Lebedev2000].

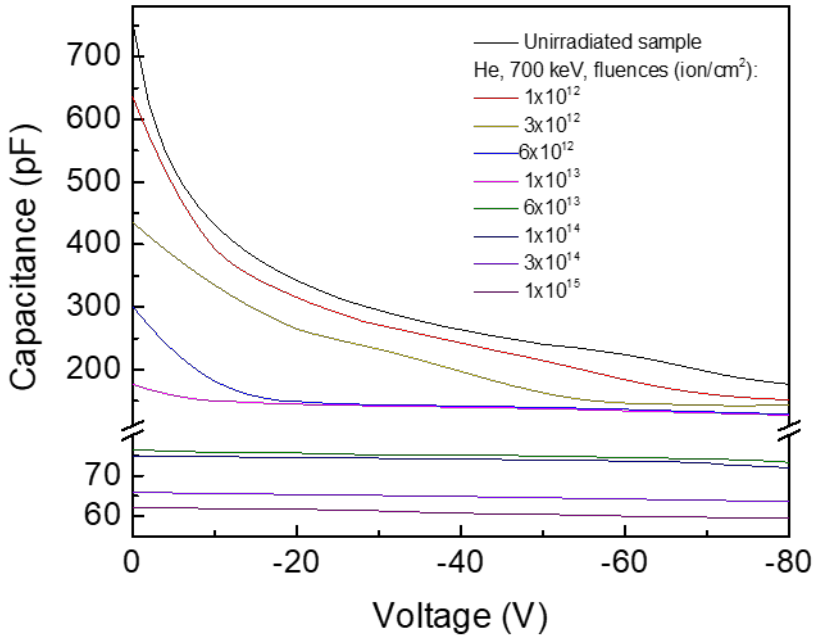

Figure 4.2.5: capacitance- voltage (C-V) characteristics of unirradiated and irradiated 4H-SiC p-n junction.

The C-V characteristics (figure 4.2.5) show a capacitance decrease by increasing the irradiation fluence which indicates a decrease in the carrier concentration after irradiation as supported by the reverse I-V curves trend (figure 4.2.2).

The carrier concentration (N_d) in the n side of junction is calculated by the $(A/C)^2$ plot slope as shown in figure 4.1.3 and it is reported as a function of fluence up to 10^{13} ion/cm^2 (bottom x- axis) and as a function of vacancy concentration (top x- axis), calculated by the SRIM software [Ziegler 2013], in the figure 4.2.6 a.

The flat C-V characteristics obtained for the irradiated samples with a fluence greater than 10^{13} ion/cm^2 (figure 4.2.5) makes impossible the determination of N_d.

The carrier concentration decreases almost linearly by increasing the irradiation fluence (figure 4.2.6 a), in agreement with the empirical relation reported by Paese et al., [Paese1987]; N_d value varies from 7.5 x 10^{17} cm^{-3}, for the unirradiated sample, to about 2 x 10^{17} cm^{-3} for the irradiated sample with a fluence of 6 x 10^{12} ion/cm^2 where the vacancy concentration in the epitaxial layer reaches the value of 8.4 x 10^{17} cm^{-3} [Pellegrino2021]. Moreover, the decrease in the carrier concentration of about a factor 3.7 is coherent with the increase of the series resistance (figure 4.2.4), indicating that the carrier mobility is almost unchanged up to this value of irradiation fluence (6 x 10^{12} ion/cm^2). Certainly, at higher irradiation fluence the carrier concentration continues to decrease and simultaneously the carrier mobility could significantly reduce.

The carrier reduction efficiency (compensation/vacancy), obtained from the slope of the N_d versus vacancy concentration plot (figure 4.2.6 a), as a function of N_d, is shown in figure 4.2.6 b. The efficiency increase by increasing the carrier concentration is due to the reduced average distance between the donor atoms for high concentrations of these last; this indicates that the free carrier reduction is mainly due to the donor passivation when combined with the radiation induced point defects as observed by Aberg et al. [Aberg2001].

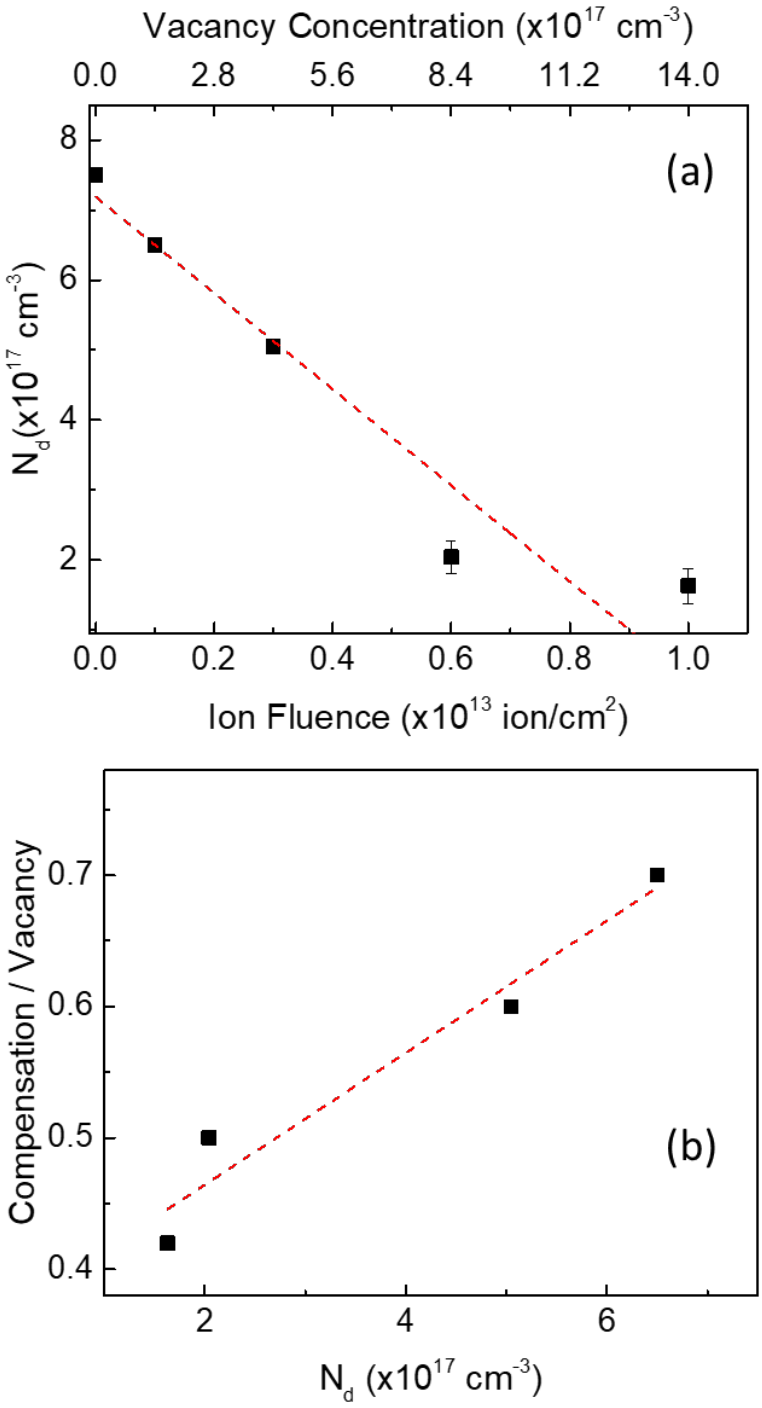

Figure 4.2.6: (a) Carrier concentration (N_d) versus irradiation fluence (bottom x- axis) and vacancy concentration (top x- axis), (b) compensation- vacancy ratio as a function of N_d.

4.2.2 Effects of defects in the device performance

The forward I-V characteristics (figure 4.2.1) in the low voltage range depends on the mechanisms which contribute to the current flow and on the carrier lifetime as well as on the depletion region width; the former one is related to the ideality factor n, instead the last two are related to the saturation current I_0 (see chapter 2). The analysis of these parameter was already discussed in the paragraph 4.1 (figure 4.1.2).

The figure 4.2.7 shows the ideality factor n as a function of irradiation fluence. The n parameter is equal to 1.3 for the unirradiated device and it increases up to the value 2.1 at a fluence of $6x10^{12}$ ion/cm^2 (figure 4.2.7 inset). The n values indicate that in the unirradiated and low fluence irradiated devices (10^{12} ion/cm^2) both diffusion and recombination mechanism contribute to the current flow. The increase of n at high fluence indicates that the recombination mechanism become dominant. Pezzimenti et al. [Pezzimenti2017] correlated the increase of ideality factor n to the increase of concentration of point defects such as $Z_{1/2}$ and $EH_{6/7}$ (paragraph 1.3). At high fluence ($\geq 10^{13}$ ion/cm^2), the ideality factor reaches the almost constant value of 2.2 which indicates a forward current mainly due to the recombination mechanism [Pellegrino2021].

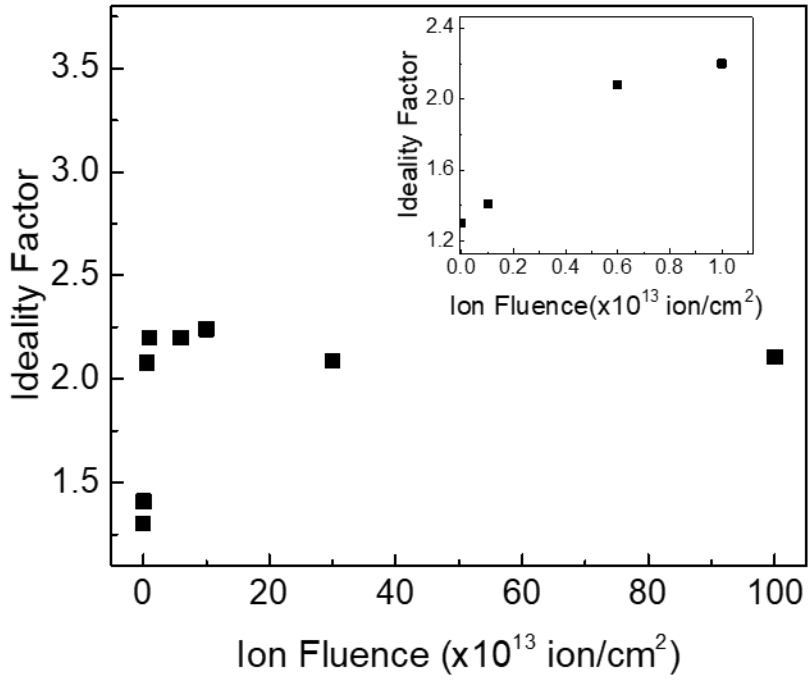

Figure 4.2.7: Ideality factor (n) as a function of irradiation fluence. In the inset the trend at low fluence is shown in details.

The saturation current density J_0 (ratio between the saturation current I_0 and device area A) as a function of the He^+- irradiation fluence is shown in figure 4.2.8. It increases about three order of magnitude up to the fluence $6x10^{12}$ ion/cm^2 and, then, at higher irradiation fluence ($\geq 10^{13}$ ion/cm^2), abruptly decreases of about eight order of magnitude [Pellegrino2021].

The J_0 is directly proportional to the depletion region width W and inversely proportional to the effective carrier lifetime τ_0 (equation 2.1.21, see chapter 2). Moreover, the J_0 variation is related to the shift of forward I-V curves (changes in the turn-on voltage, figure 4.2.1 a). At low fluences (up to 6 x 10^{12} ion/cm^2), the increase of J_0 is associated both with the increase of W and the decrease of τ_0. In particular, the depletion region width W (inversely proportional to the capacitance C, equation 2.1.4) increases after irradiation at $6x10^{12}$ ion/cm^2 by about a factor 3, equal to the capacitance decrease at

V=0 (figure 4.2.5); thus, the observed increase of J_0 (about three orders of magnitude) is mainly due to the carrier lifetime τ_0 decrease (more than two order of magnitude). This variation of τ_0 is related to the recombination centers concentration (N_T) increase (equation 2.1.15 and 2.1.16).

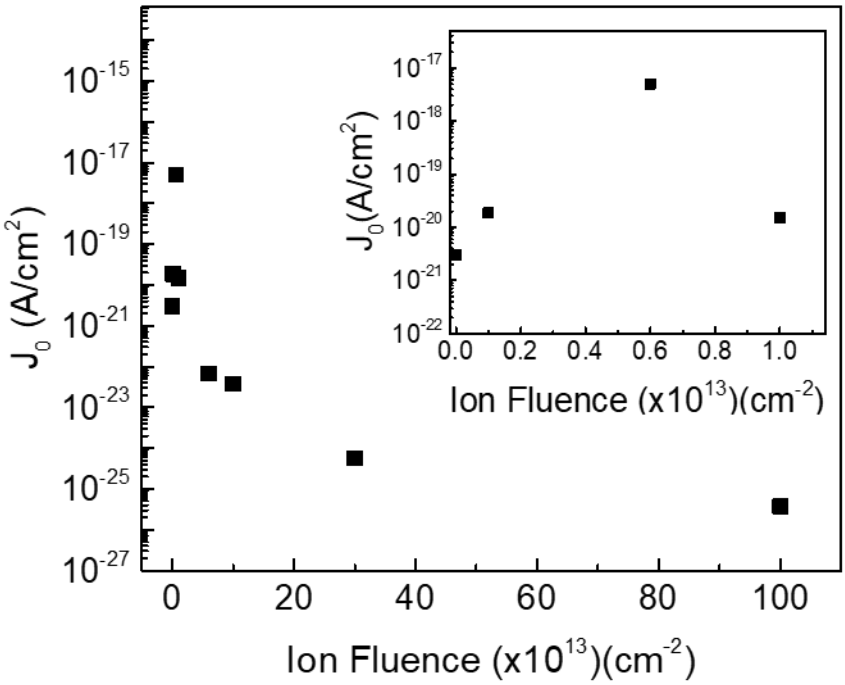

Figure 4.2.8: Saturation current density (J_0) as a function of irradiation fluence, in inset J_0 up to the fluence of 10^{13} ion/cm^2

At higher fluence ($\geq 10^{13}$ ion/cm^2), it is possible to observe a decrease of J_0 of about eight order of magnitude (figure 4.2.8), however it is impossible a decreases of radiation induced point defects concentration N_T; moreover, the ideality factor value ($n \approx 2$) in this range of fluence ($\geq 10^{13}$ ion/cm^2) indicates a current flow mainly due to the recombination mechanism. However, this experimental observation can be explained with the existence of further events influencing the current flow such as the point defects agglomeration or their rearrangement already observed by P. Hazdra et al. [Hazdra2019].

The changes in the p-n junction parameters such as R_s, n and J_0 can be related to the deep levels within the band gap of semiconductor associated with the radiation induced defects. In order to investigate about these defects DLTS measurements were performed.

The figure 4.2.9 a shows the DLTS spectra acquired at different rate windows (from 2 to 23 s^{-1}) of the He^+- irradiated sample with the fluence of 10^{12} ion/cm^2. Two main peaks at about 290 K and 620 K appear in the DLTS spectra (figure 4.2.9 a); their energies (E_t) are 0.61 ± 0.05 eV and 1.50 ± 0.05 eV below the conduction band edge E_C, respectively, as obtained from the slope of Arrhenius plot (figure 4.2.9 b) by using the equation 3.3.4. These two defects are identified in literature as $Z_{1/2}$ (E_c-E_t ≈ 0.61 eV) and $EH_{6/7}$ (E_c-E_t ≈ 1.5 eV) [Kimoto2014]. Instead, the main contribution to the DLTS signal in the temperature range 400- 500 K (figure 4.2.9 a) is given by $RD_{1/2}$ defects, also identified in literature [Kimoto2014], with an energy of 0.95 ± 0.05 eV below the conduction band edge E_C as obtained from the Arrhenius plot slope (figure 4.2.9 b) [Pellegrino2021].

Some authors report that both $Z_{1/2}$ and $EH_{6/7}$ centers originate from the same structural defects (carbon vacancy) with different charge state [Kimoto2014]. However, in some papers the $Z_{1/2}$ has been related to different structures such as interstitial carbon (C-interstitial), antisites [Castaldini2004], [Izzo2009] and silicon vacancy (V_{Si}) while $EH_{6/7}$ is attributed to the silicon- carbon vacancy (V_{Si} + V_C) [Kimoto2014], [Kawara2013], [Castaldini2005]. The presence of these two defects is reported in literature both in as-grown and irradiated 4H-SiC samples [Kimoto2014], [Hazdra2013], [Davidov2001]. Instead, the exact correlation between $RD_{1/2}$ center and a specific structural defect has not been established, but V_{Si}, V_C or antisites could be responsible for these centers mainly related to the radiation damage (RD) [Hazdra2013], [Izzo2009], [Castaldini2005].

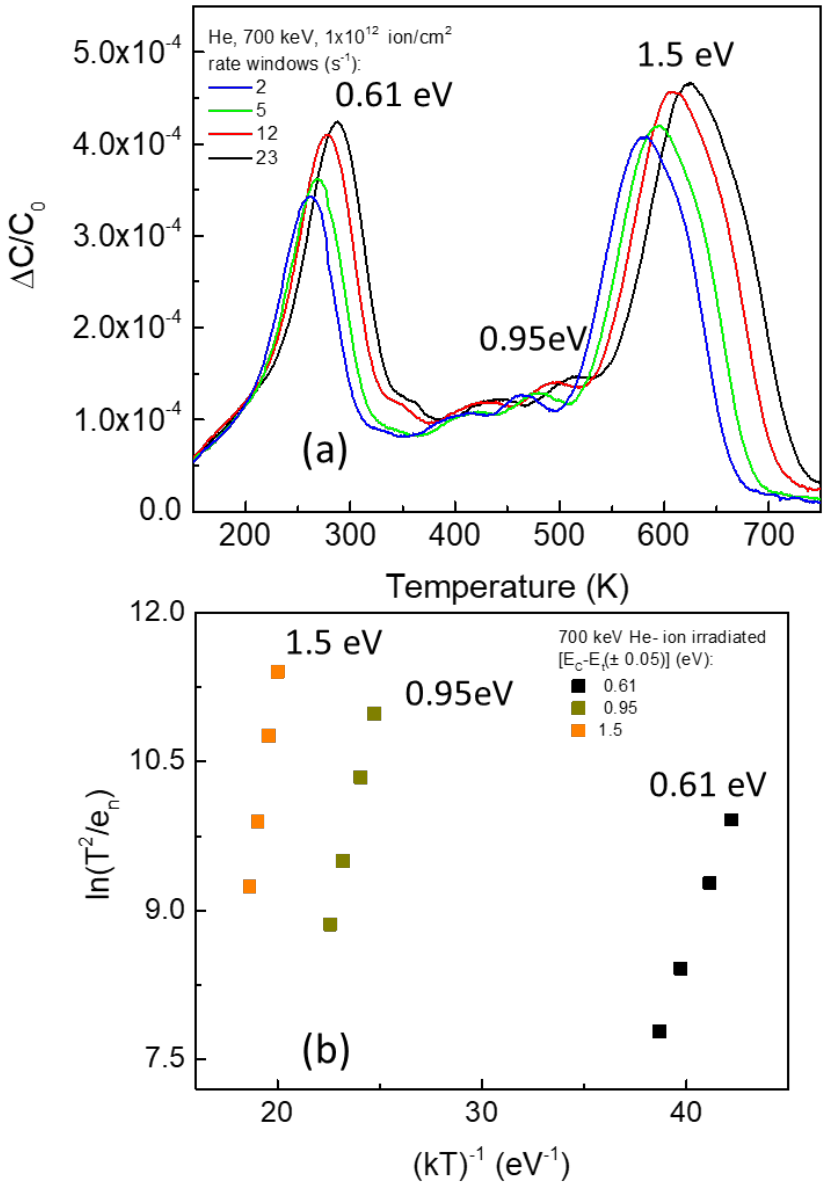

Figure 4.2.9: a) DLTS spectra of the He^+- irradiated sample with a fluence of 10^{12} ion/cm^2 at different rate windows (2 - 23 s^{-1}) and (b) relative Arrhenius plot.

The figure 4.2.10 shows the DLTS spectra (acquired at rate windows of 23 s^{-1}) of samples irradiated at different fluence (1 x 10^{12}, 6 x 10^{12}, 1 x 10^{13}, 6 x 10^{13} and 1 x 10^{15} ion/cm^2).

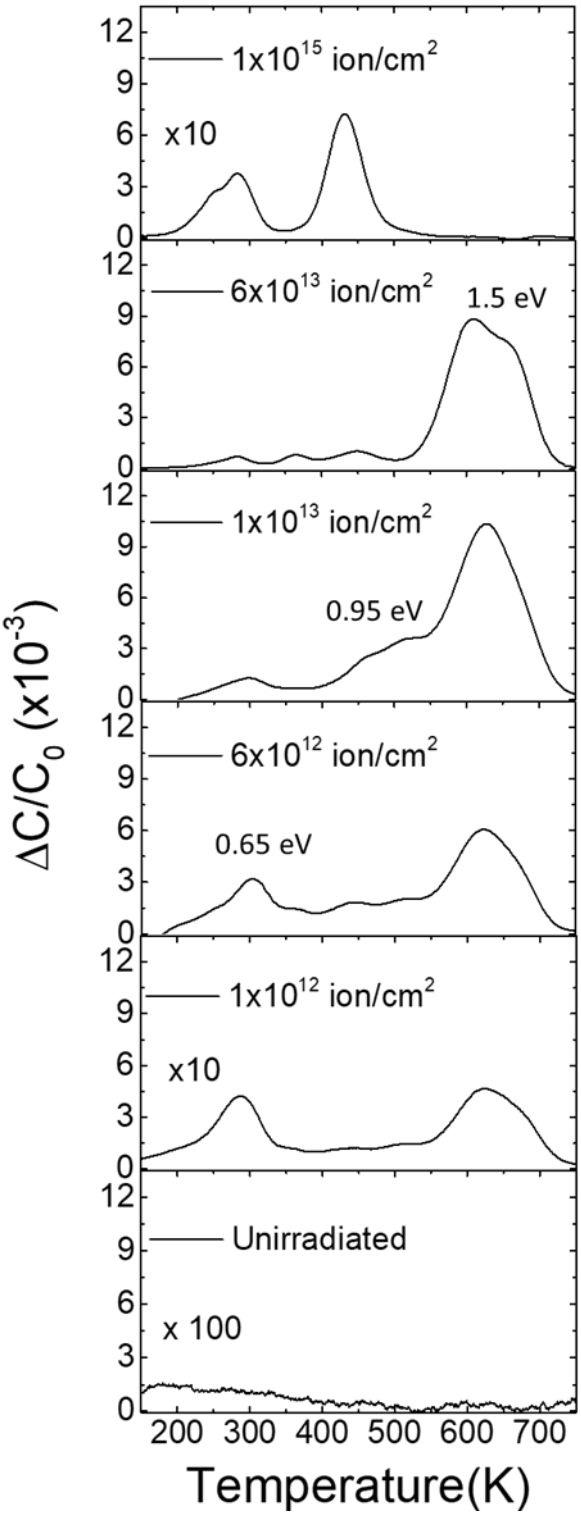

Figure 4.2.10: DLTS spectra of unirradiated and irradiated devices (fluences: 1 x 10^{12}, 6 x 10^{12}, 10^{13}, 6 x 10^{13}, 1 x 10^{15} ion/cm^2).

The DLTS spectrum (figure 4.2.10) of unirradiated diode does not show any relevant presence of traps, evidencing the good crystalline quality of the epitaxial layer. At the fluence of 6 x 10^{12} ion/cm^2 an increase in the intensity of DLTS signal $\Delta C/C_0$ (proportional to the traps concentration N_t by means of equation 3.3.7) related to the defects $Z_{1/2}$, $EH_{6/7}$ and $RD_{1/2}$ (Arrhenius plot in figure 4.2.11 a) is observed (figure 4.2.10); these defects are already identified in the sample irradiated with a fluence of 10^{12} ion/cm^2 (figure 4.2.9 a). The further increase of the fluence at 1 x 10^{13} ion/cm^2 induces a variation in the defect concentration ($Z_{1/2}$, $EH_{6/7}$ and $RD_{1/2}$), also identified in this sample by means of an Arrhenius plot (figure 4.2.11 b): $EH_{6/7}$ and $RD_{1/2}$ traps concentration increases while the $Z_{1/2}$ concentration slightly decreases. The concentration of the defects for the irradiation fluence of 1x 10^{13} ion/cm^2 is in the range 1x 10^{15} - 4 x 10^{15} cm^{-3}. At higher fluence (6x10^{13} ion/cm^2), the $EH_{6/7}$ related peak (at $\approx$ 620 K) evolves, in the DLTS spectrum appears a shoulder at about 650 K (figure 4.2.10). By increasing the fluence at 1 x 10^{15} ion/cm^2 only the $Z_{1/2}$ (peak at 287K) and $RD_{1/2}$ (peak at 440 K) defects survive (figure 4.2.10).

The observed trend evidences that a rearrangement of defects occurs over the fluence threshold of 1x10^{13} ion/cm^2. It must be outlined that at fluence greater than this threshold value the concentration of defects could be higher than the dopant concentration and, therefore, quantitative evaluation of ion irradiation defects is not possible by DLTS. However, the DLTS results help us to identify two irradiation fluence regions: i) a low fluence regime (fluence $\leq$ 1 x 10^{13} ion/cm^2) in which ions irradiation produces point defects whose concentration increases with the fluence; ii) a high fluence regime (fluence > 1 x 10^{13} ion/cm^2), characterized by a decrease of the point defects concentration and, at the same time, by an interaction between primary defects [Pellegrino2021]. This interaction gives rise to clustering of point defects and formation of more complex defects such as atoms clusters.

These complex defects are not observable by DLTS analyses probably because they are not electrically active or because the associated band gap levels are too deep in energy to be detected with our system; however, the defects agglomerations are known in literature [Storasta2004], [Litrico2009], [Hazdra2019]. At high fluence, the defect concentration increases, thus the mean vacancy distance is reduced and point defects aggregation can occur. The defects evolution observed by the DLTS spectra are in agreement with the results on the trend of the J_0 parameter (figure 4.2.8): at fluence < 1.0 x 10^{13} ion/cm^2, the J_0 increase is mainly associated to the accumulation of point defects while, at higher fluence, J_0 decreases evidencing the existence of a new process influencing the current flow in the diode, ascribable to the formation of a different kinds of defects.

Then, in summary, the He^+ irradiation affects the electrical performance of the devices. In particular, the increase in the ion fluence produce an increase in the series resistance (figure 4.2.4), mainly due to a decrease in free carrier concentration (figure 4.2.6 a) as obtained from the C-V measurement (figure 4.2.5) and affects both the ideality factor n (figure 4.2.7) and the saturation current density J_0 (figure 4.2.8) as obtained from the I-V measurements: the increase in the ideality factor (figure 4.2.7) evidences the recombination mechanism contribution to the current flow by means of the radiation induced deep level centers; instead, the increase of the saturation current density J_0 (figure 4.2.8), mainly related to the carrier lifetime, and its subsequent decrease at fluences greater than 1x 10^{13} ion/cm^2 (figure 4.2.8) can be ascribed to the evolution of the radiation induced defects as shown from the DLTS spectra as a function of the fluence (figure 4.2.10) [Pellegrino2021].

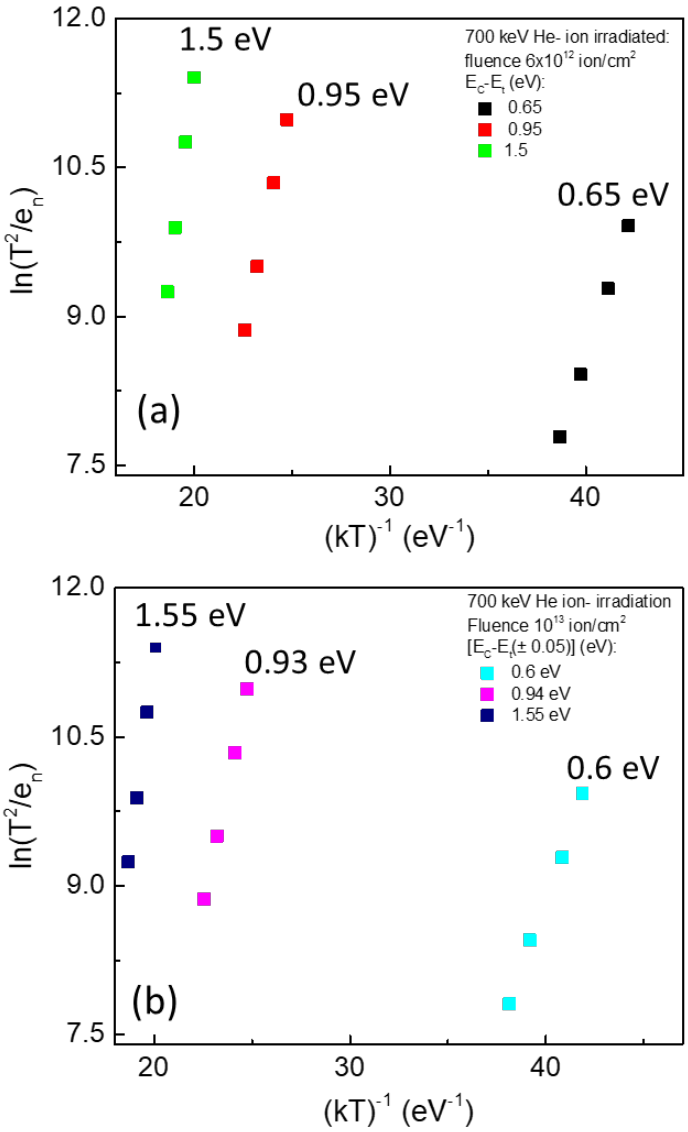

Figure 4.2.11: Arrhenius plot of the irradiated samples with the fluence of (a) $6x10^{12}$ ion/cm^2 and (b) 10^{13} ion/cm^2.

4.3 Temperature behavior

The temperature dependence on I-V characteristic of irradiated devices evidences the change in the semiconductor junction properties induced by irradiation and allows to obtain more information about the defect structure and defect evolution on irradiated SiC.

4.3.1 Low fluence irradiated diodes

The figure 4.3.1 shows the reverse (a) and forward (b) current- voltage (I-V) characteristics of diode irradiated at fluence of 6 x 10^{12} ion/cm^2, measured in the temperature range 298÷ 448 K [Pellegrino2021].

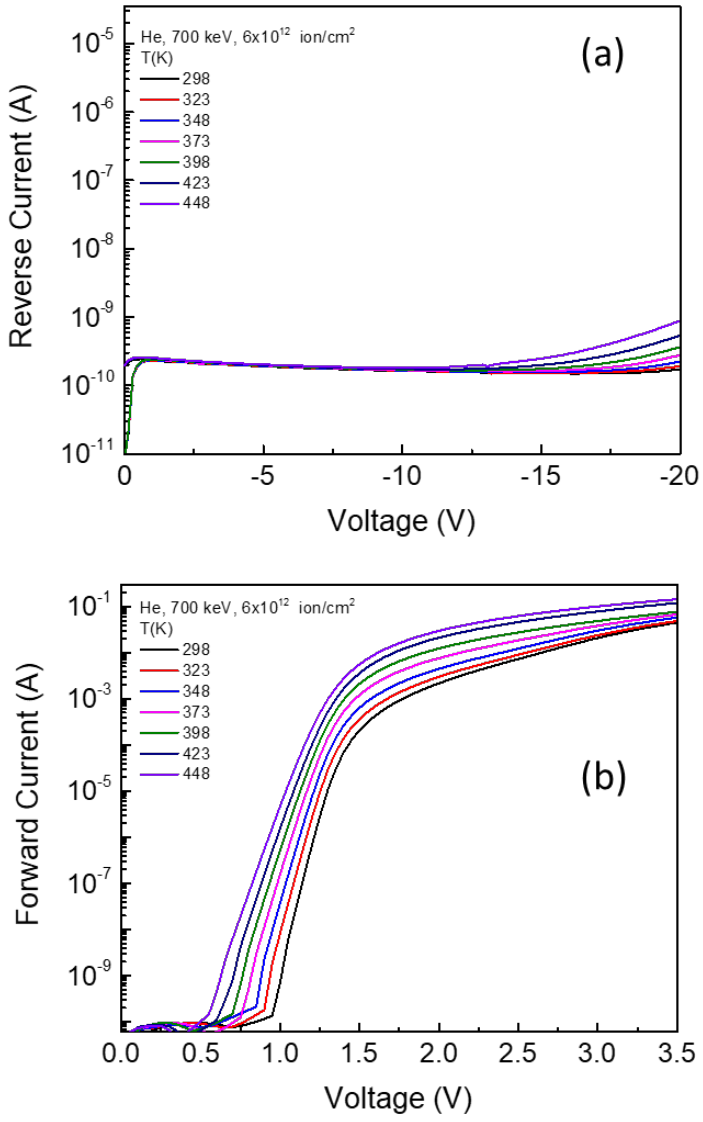

Figure 4.3.1: a) Reverse and b) forward current- voltage (I-V) characteristics of diode irradiated at low fluence (6 x 10^{12} ion/cm^2) in the temperature range 298÷ 448 K

The reverse current of diode irradiated at fluence of 6 x 10^{12} ion/cm^2 (figure 4.3.1 a) as well as that of unirradiated sample shows a weak dependence from temperature. Instead, the temperature affects the forward I-V characteristics of low fluence irradiated diode (figure 4.3.1 b) as well as that of unirradiated device: in both cases, by increasing the temperature, we observe a decrease in the turn-on voltage and an increase in the forward current (at fixed bias) as reported also in literature [Strel'chuch2005], [Pistavu 2019].

The ideality factor n and the saturation current density J_0 were calculated from all the I-V curves, measured at different temperatures; in particular, as described in the paragraph 4.1, n is related to the slope of the forward I-V curve in the low voltage region while J_0 is related to the intercept at V = 0. The former remains almost constant with temperature while the saturation current density J_0 exhibits an exponential dependence (equation 2.1.22); in particular, the J_0 parameter is correlated to the trap activation energy E_a which is mainly related to the band gap energy E_g and to the trap energy level E_t (equation 2.1.24). The J_0 temperature dependences for the unirradiated (black square) and low fluence irradiated devices (6 x 10^{12} ion/cm^2) are shown in the figure 4.3.2; in both case the activation energy is calculated from the slope of the J_0 versus $(kT)^{-1}$ plot. The E_a values is 1.40 ± 0.05 eV, for unirradiated sample, and of 1.50 ± 0.05 eV for low fluence irradiated diode [Pellegrino2021]. The obtained data are consistent with the SRH model of recombination via a deep level near the middle of the band gap [Shockley1952], [Sah1957], (3.2 eV in the case of 4H-SiC [kimoto2014]), as well as with the literature [Li2005], [Strel'chuk2005], [Strel'chuch2001].

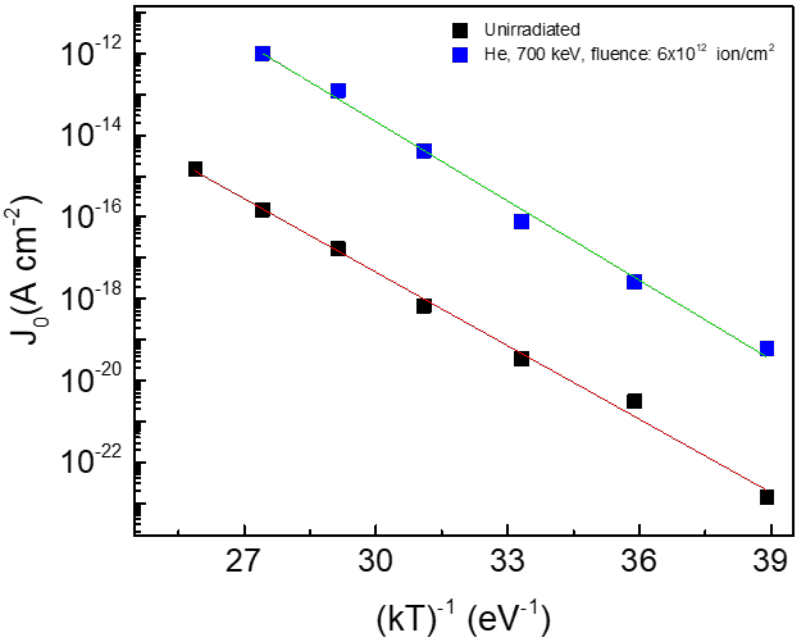

Figure 4.3.2: Saturation current density J_0 as a function of $(kT)^{-1}$ for un-irradiated and $6x10^{12}$ ion/cm^2 irradiated devices.

4.3.2 High fluence irradiated diodes

The devices irradiated at fluence $\geq 10^{13}$ ion/cm^2 show a dependence on the measurement temperature in both the reverse and forward polarization.

In particular, the increase of temperature induces an increase in the reverse current as shown in the figure 4.3.3 for a fluence of $1x10^{15}$ ion/cm^2. In this case, we observe an exponential dependence of the reverse current from the temperature and from the slope of the current, at -20V, versus $(kT)^{-1}$ plot (figure 4.3.3 inset) we extracted an activation energy of about 0.7 eV. This energy is very close to the $Z_{1/2}$ energy level, which is present in the high fluence irradiated samples as shown in the DLTS spectra (figure 4.2.10). This result evidences that the related defect is responsible of the inverse current [Pellegrino2021].

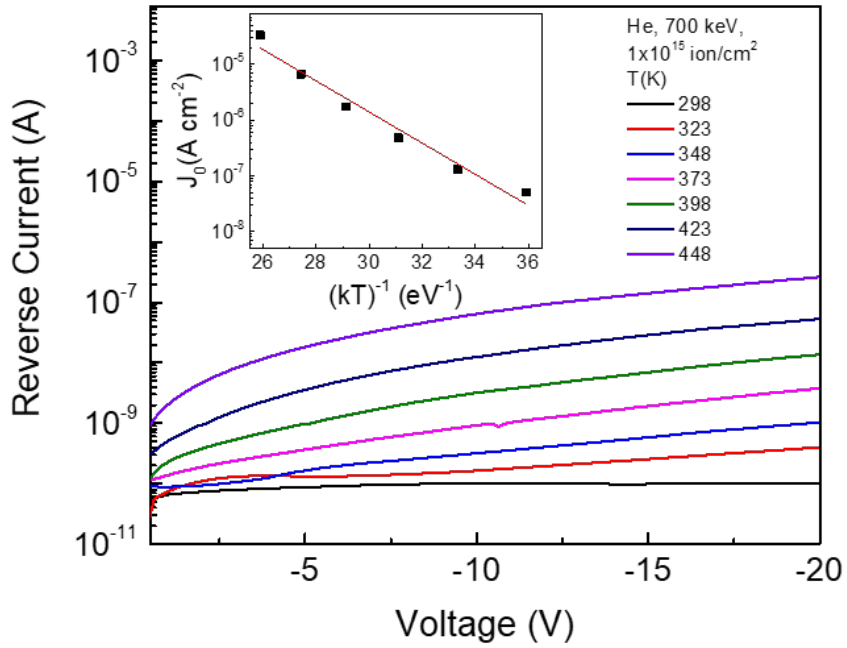

Figure 4.3.3: Reverse I-V characteristics of diode irradiated at 1 x10^{15} ion/cm^2 in the temperature range 298÷ 448 K. In inset the current density J_0 at reverse voltage of 20 V as a function of $(kT)^{-1}$

The forward I-V characteristics of irradiated diodes show also a temperature dependence. In particular, by increasing the irradiation fluence (≥ 1x10^{13} ion/cm^2), the forward I-V characteristics show an extra-current at low bias which increases with the temperature. In the case of 6x10^{13} ion/cm^2 irradiated diode, the forward I-V characteristic (figure 4.3.4), measured at different temperatures, shows the extra-current contribution, mainly centered in the voltage region between 1.0 – 1.5 V, which increases for temperature greater than 398 K [Pellegrino2021]. This effect could be related to new mechanisms contributing to the current flow over the recombination current. Similar results are already observed in the as-fabricated [Strel'chuch2006], [Strel'chuch2014] and aluminum [Pezzimenti2017], gamma ray and neutron [Strel'chuch2005] irradiated 4H-SiC p-n junction. The extra-current was attributed to the epitaxial layer

defects and is due to the shunt paths [Pezzimenti2017], [Strel'chuch1997], [Wolf1977].

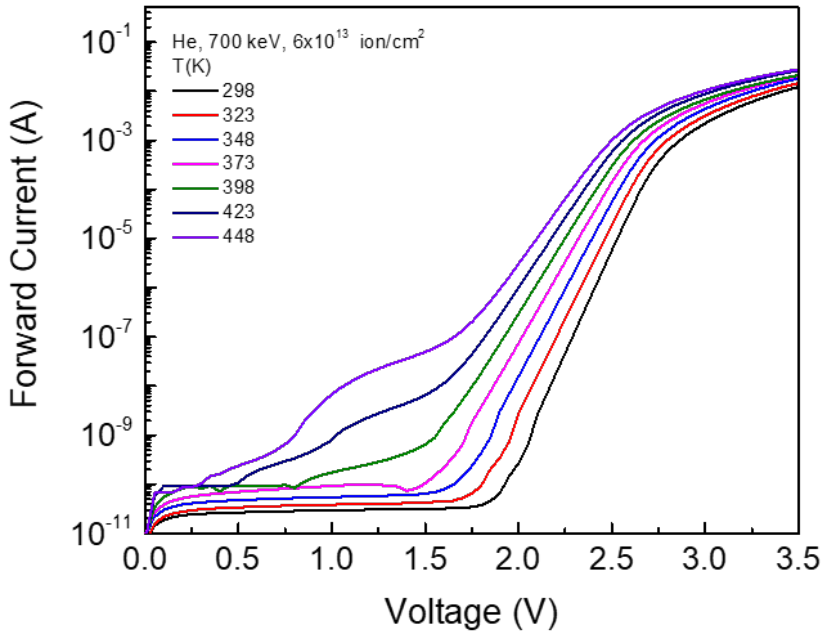

Figure 4.3.4: Forward I-V characteristics of He^+- irradiated diode at 6 x10^{13} ion/cm^2 in the temperature range 298÷ 448 K.

The figure 4.3.5 shows the forward I-V characteristics measured at 448 K for the irradiated diodes at three different fluences (ion/cm^2): 1x10^{13} (black square), 6x10^{13} (red circle) and 1x10^{15} (green triangle). By increasing the irradiation fluence, the extra-current contribution is shifted at lower voltage; moreover, in the high voltage region (V > 2.2V) the current decreases. The experimental results obtained for high fluence irradiated diodes (figure 4.3.5) can be explained and modeled by using the "parallel double diodes model", used for the first time by Wolf in 1977 [Wolf1977] and, successively by Banerjee [Banerjee1986]: the analyzed p-n diode is equivalent to an electric circuit with two parallel branches containing respectively an ideal diode in series with an ideal resistance, named as a

diodes D_1, D_2 and resistance R_1 and R_2 as shown in the inset of figure 4.3.5. The total current I is given by the following equation:

$$I = I_1 + I_2 + I_{sh} \tag{4.3.1}$$

where I_{sh} is a shunt term obtained from the current value at V = 0 V while I_1 and I_2, are the current in the ideal diode 1 and diode 2, respectively. The voltage across each diode is equal to V_A- ($I \cdot R_s$) where V_A is the applied voltage and R_s the diode series resistance.

In the figure 4.3.5 is reported the fit carried out on the I-V curve of the $6x10^{13}$ ion/cm^2 irradiated diode (red circle) by using the parallel double diodes model where the red dash line is related to the diode 2 (D_2), the black dash line to the diode 1 (D_1) and the blue dash line refers to the total current flowing in the system, given by equation (4.3.1) [Pellegrino2021].

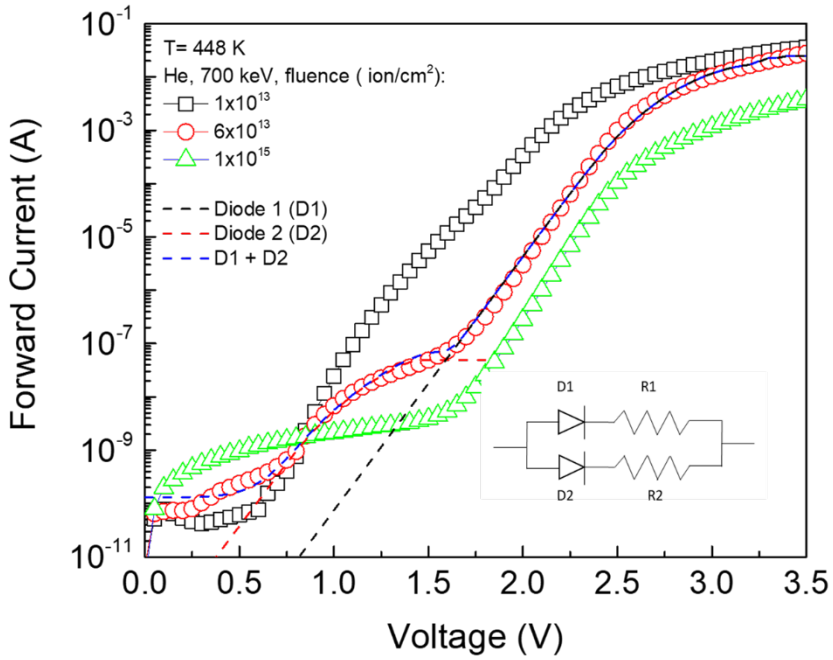

Figure 4.3.5: Forward, I-V characteristic at 448 K for different irradiation fluence (see text). The fit of the I-V characteristic is reported for the 6.0×10^{13} ion/cm^2 irradiated device. In the insert, a typical equivalent circuit of the p-n structure is sketched.

The ideality factor n is fixed to the value of 2 for both diodes (D_1 and D_2) while the saturation current density $J_{0,1}$ and series resistance R_1 for the diode D_1 as well as those ($J_{0,2}$ and R_2) for diode D_2 are extracted from the fit of the experimental curves.

The figure 4.3.6 shows the $J_{0,1}$ (a) and R_1 (b) as a function of $(kT)^{-1}$ for the high fluence irradiated devices: $1x10^{13}$ ion/cm^2 (black square), $6\ x10^{13}$ ion/cm^2 (red square) and $1x10^{15}$ ion/cm^2 (green square). In all cases $J_{0,1}$ (figure 4.3.6 a) exhibits an exponential trend (following the equation 2.1.22) with an activation energy E_a, obtained from the slope of the $J_{0,1}$ versus $(kT)^{-1}$ plot, in the range 1.5 ÷ 1.7 eV, very close to half energy band gap ($E_g/2 \approx 1.6$ eV) as expected in the SHR model [Shockley1952]. Instead, the series resistance R_1 shows a week dependence from the temperature and, thus, a negligible activation energy [Pellegrino2021].

The analysis of saturation current density and series resistance by using the same model is also performed for the diode 2 (D_2) for the same high fluence irradiated devices (figure 4.3.7). The saturation current density $J_{0,2}$ (figure 4.3.7 a) exhibits an exponential behavior as observed in the case of the diode D_1 (figure 4.3.6 a); however, $J_{0,2}$ values are higher than the $J_{0,1}$. It must be outlined that the determination of $J_{0,2}$ for the device irradiated at the fluence of $1x10^{15}$ ion/cm^2 is quite impossible because the I-V curve exhibits a very low turn-on voltage (green triangle, figure 4.3.5). The activation energy evaluated for the diode D_2 gives a value in the range 1.6÷1.7 eV as obtained for the diode D_1 (figure 4.3.6 a) and also for the unirradiated and low fluence irradiated devices (figure 4.3.2) [Pellegrino2021].

The obtained E_a values in all these cases confirm that the current flow is due to the SHR generation current mechanism through a deep level near the middle of the band gap.

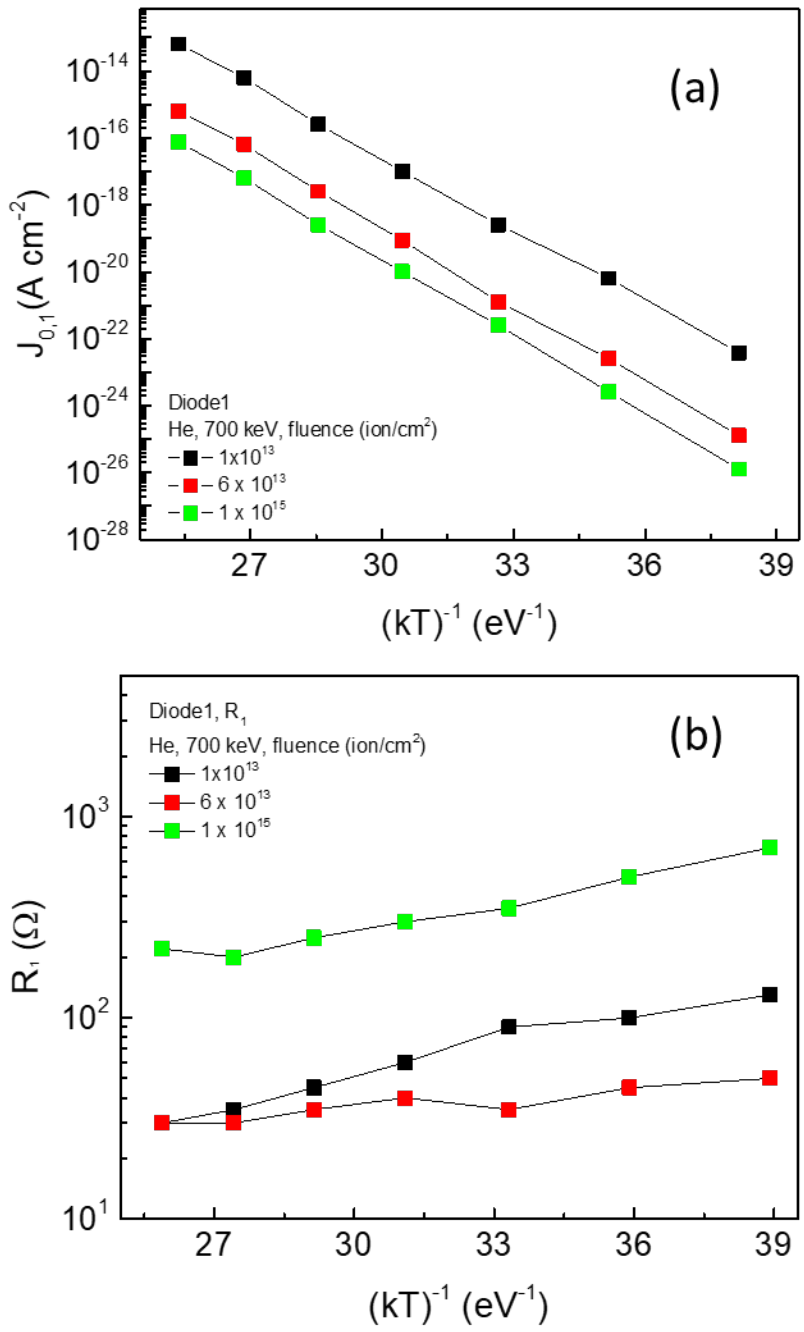

Figure 4.3.6: Diode D_1 saturation current density $J_{0,1}$ (a) and series resistance R_{s1} (b) as a function of $(kT)^{-1}$ for high fluence- irradiated diodes obtained by using the "parallel double diodes" structure (see text).

The series resistance for the diode D_2 (figure 4.3.7 b) exhibits higher values (several orders of magnitude) with respect the diode D_1 and a quite different trend with temperature. In all analyzed devices, R_2 shows an exponential behavior with the temperature. The activation energy, obtained from the slope of R_2 versus $(kT)^{-1}$ plot, is in the range 0.9÷ 1.2 eV, very close to the energy of the $RD_{1/2}$ levels. The exponential dependence of series resistance with temperature was also reported by Lebedev [Lebedev Jr 2000] in p-n junction irradiated with 8.0 MeV protons and was associated with a "pinning" of the Fermi level near the irradiation induced defects [Liang2016], [Ewing2007].

Such behaviour is observed also in other semiconductor material, such as GaAs [Look1987], and occurs when the defects concentration overcomes the net doping concentration. In light of these considerations, we can state that the defect density in the region associated with the branch 1 is lower than the epilayer doping level because the activation energy is negligible (0.1 eV) while in the region associated with the branch 2 the defects density approaches (or overcomes) the doping density and the Fermi level is pinned leading to activation energy in the range 0.9÷1.2 eV. This value is very close to the energy of the $RD_{1/2}$ acceptor levels, probably the most important defect introduced by high fluence ion irradiation in SiC [Pellegrino2021].

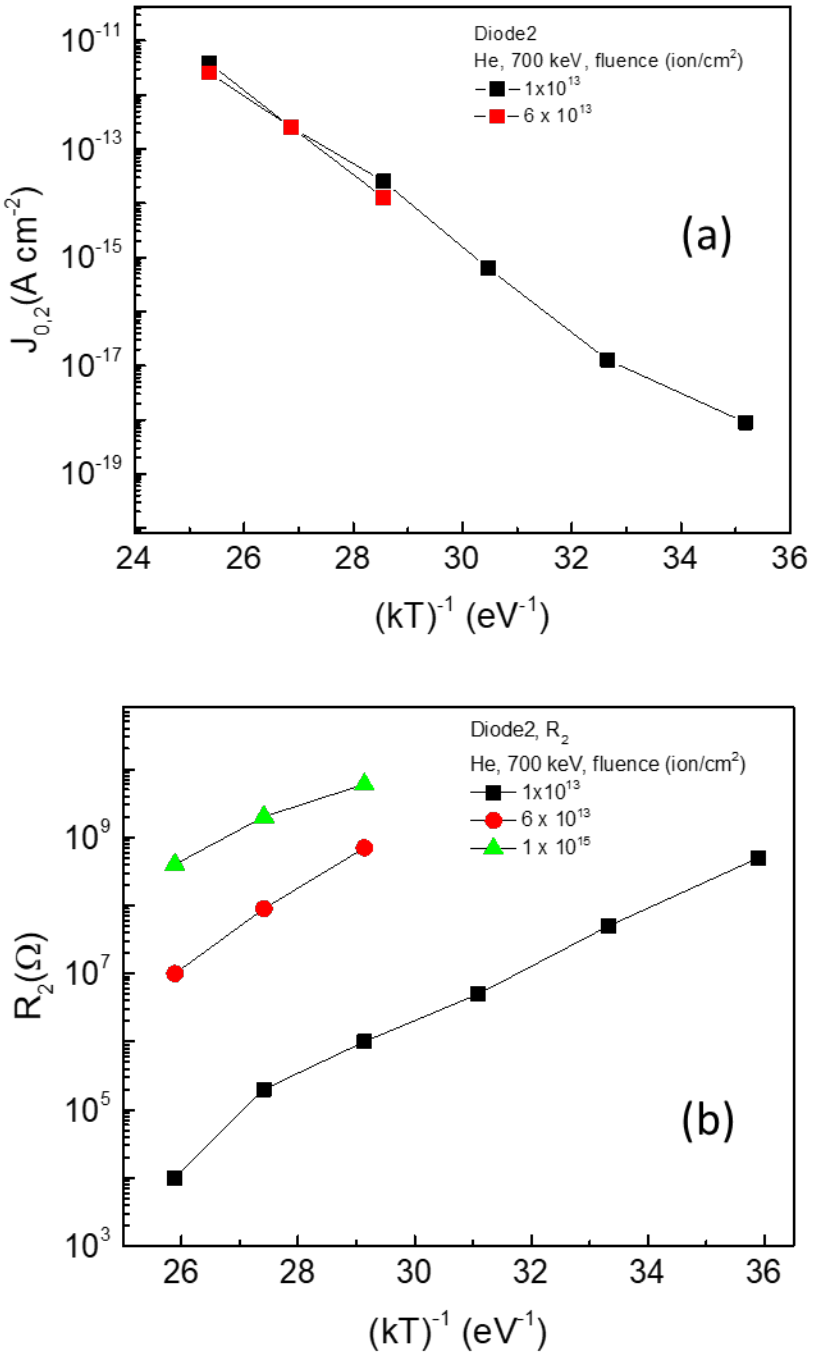

Figure 4.3.7: Diode D_2 saturation current density $J_{0,2}$ (a) and series resistance R_{s2} (b) as a function of $(kT)^{-1}$ for high fluence- irradiated diodes obtained by using the "parallel double diodes" structure (see text).

In summary, the I-V measurements as a function of temperature evidence a different behavior in the different fluence irradiated diodes. In particular, in the low fluence regime ($< 1 \times 10^{13}$ ion/cm^2), the forward I-V characteristics shows only a decrease in the turn-on voltage and an increase in the current by increasing the temperature. The saturation current density shows an exponential behavior with the temperature and an activation energy consistent with the SHR model is obtained. Instead, the reverse current exhibits a weak dependence on temperature. The opposite situation is observed in the high fluence regime ($\geq 1 \times 10^{13}$ ion/cm^2), both forward and reverse I-V characteristics shows a dependence from the temperature. In particular, the forward I-V characteristics exhibit the presence of an extra-current at low voltage growing with the temperature. The observed results are explained with the "parallel double diodes" model which allows to analytically describe the presence of two different kinds of active defects contributing to the forward current flow. The former are point defects that pre-exist in the epilayer and/or are introduced by low fluence He^+ irradiation; instead, the others are produced by the high irradiation fluence. The obtained activation energy for the saturation current density for both kinds of defects confirms the SHR generation current mechanism. Instead, the series resistance shows an exponential dependence on the temperature only for high irradiation fluence; the obtained activation energy in the range 0.9 – 1.2 eV evidences the contribution of $RD_{1/2}$ radiation induced defects to the current flow.

Conclusion

Thanks to its excellent chemical and physical properties Silicon Carbide is undoubtedly the optimal material for power electronics and more generally for fabrication of devices able to operate in hostile environment such as radiation rich ones and for many years SiC was described in literature as a radiation hard material. In this thesis we have conducted a study on the effects of ion irradiation on the electrical performances of the p-n junction in order to evaluate its use in this particular environment. The ion irradiation in fact induces damage and a degradation in the electric characteristics of 4H-SiC based devices.

In the present thesis, the effects of He^+ irradiations (in the fluence range $10^{12} \div 10^{15}$ ion/cm^2) on the 4H-SiC p-n junction were examined through current-voltage (I-V), capacitance-voltage (C-V), and DLTS measurements.

The electrical performances of the devices change after irradiation. In particular, at high voltage, the forward current is entirely dominated by the series resistance which increases with ion fluence mainly due to the decrease of free carrier concentration. Instead, in the low voltage region, the irradiation affects both the ideality factor n and the saturation current density $J_{0.}$ The former increases with irradiation fluence and, then, saturate at 2.1, evidencing the generation-recombination mechanism contribution to the current flow by means of deep level centers. The saturation current density J_0, mainly related to the carrier lifetime, increases at irradiation fluence lower than 1x 10^{13} ion/cm^2 and, then decreases at high fluence ($\geq$ 1x 10^{13} ion/cm^2). The reverse current instead decreases at high irradiation fluence. The DLTS measurements help us to identify the radiation induced point defects and its evolution with fluence.

Two fluence regimes are identified. At low fluence, ion irradiation induces the formation of point defects (mainly $Z_{1/2}$, $RD_{1/2}$ and $EH_{6/7}$), whose

concentration increases by increasing the fluence: these defects exhibit an acceptor -like behavior mainly inducing the compensation effects in n- type SiC epilayers. At high fluence, the point defects concentration decreases and its agglomeration is promoted, producing a decrease of the saturation current density J_0. The threshold fluence which separates the two observed regime is experimentally identified with the $1x10^{13}$ ion/cm^2.

The I-V measurements as a function of temperature are in agreement with the DLTS results. In the low fluence regime, the forward I-V characteristics show only a decrease in the turn-on voltage and an increase in the current by increasing the temperature. The saturation current density behavior (exponentially dependent on the temperature) is consistent with the SRH model: the recombination via a deep level near the middle of band gap gives the main contribution to the current flow. Instead, the reverse current exhibits a weak dependence on temperature. The opposite situation is observed in the I-V characteristics, as a function of temperature, of the diodes irradiated at the high fluence ($\geq 1x\ 10^{13}$ ion/cm^2). The forward I-V characteristics shows the presence of an extra- current at low voltage which increases by increasing the temperature; this effect can be related to the evolution of radiation induced point defects such as their agglomeration as evidenced by the DLTS measurements. In fact, the DLTS spectra of the irradiated sample at fluence of 6×10^{13} ion/cm^2 shows a variation in the $Z_{1/2}$ and $RD_{1/2}$ defects concentration and an evolution of the $EH_{6/7}$ defects. Moreover, also the reverse current of high fluence irradiated devices show a temperature dependence.

To explain the observed results and to describe the different kinds of active defects contributing to the irradiated diodes current, the forward I-V characteristics of high fluence irradiated devices are analytically analyzed by adopting the “parallel double diodes” model: the real diode is equivalent with an electrical circuit, composed by two branches, each branch is composed by a diode connected in series with a resistance. The diode D_1 is

related to point defects introduced by low fluence He^+ irradiation: it has a low generation rate and low series resistance weakly dependent on temperature. Instead, the diode D_2 is related to defects produced by irradiation at fluence $\geq 1 \times 10^{13}$ ion/cm^2 (high fluence regime); it has a high carrier generation rate and high series resistance, exponentially dependent on the temperature. In this last regime, the irradiation induces the formation of additional defects and disorders that, on one hand, create deep levels responsible for the extra- current generation (thought the SHR process) and, on the other hand, determine the high series resistance paths advent. In particular, the activation energy of the resistance in this second diode D_2, between 0.9- 1.2 eV, is very close to the energy of the $RD_{1/2}$ defects, present also in the high fluence regime as shown by DLTS spectra.

The comparison between DLTS measurements and temperature dependence of I-V characteristics indicates that an evolution of defects occurs during irradiation. In particular, it can be argued that in the low fluence regime simple defects are formed; by increasing the fluence, agglomeration of point defects occurs and these complex defects are responsible for conduction paths formation in the active device region as well as of low voltage extra-currents observable in high-temperature I-V curves.

The obtained results may be applicable to explain the ion irradiation effects on the electric characteristics of 4H-SiC p-n junction based devices, as well as for an accurate control of carrier lifetime in SiC devices. The correlation between the electrical properties and radiation induced defects as well as their evolution with fluence can be used to tune devices simulation for the defects engineering. Nevertheless, the p-n junctions show low leakage current and good rectifying proprieties up to a fluence of 10^{13} ion/cm^2, corresponding to a dose of 10 KGy confirming the radiation hardness properties of SiC devices.

Possible future measurements are related to the study of the electrical properties of He^+ irradiated device such as MOSFET, BJT and IGBT in order to correlate the change in the electrical properties of these complex devices with the results obtained for the studied He^+ irradiated p-n diodes.

Bibliography

[Aberg2001] D. Aberg et al., Nitrogen deactivation by implantation-induced defects in 4H-SiC epitaxial layers, Appl. Phys. Lett., 78, 19, 2001

[Alexandreu2014] M. Alexandru et al., 5 MeV Proton and 15 MeV Electron Radiation Effects Study on 4H-SiC n MOSFET Electrical Parameters, IEEE Transaction on Nuclear Science, 61, 1732-1738, 2014

[Alfieri2005] G. Alfieri et al., Defect energy levels in hydrogen-implanted and electron-irradiated n –type 4H- Silicon Carbide, J. Appl. Phys. 98, 113524, 2005

[Askeland2011] D. R. Askeland, P. P. Fulay and W. J. Wright, The Science and Engineering of Materials, ed. Cengage Learning, 2011

[Auret2004] F. Danie Auret and Prakash N.K. Deenapanray, Deep Level Transient Spectroscopy of Defects in High-Energy Light-Particle Irradiated Si, Critical Reviews in Solid State and Materials Sciences, 29, 1, 2004

[Baliga2005] B. J. Baliga, Silicon Carbide Power Device, ed. World Scientific Publishing, 2005

[Baliga2008] B. J. Baliga, Fundamentals of Power Semiconductor Devices, ed. Springer, 2008

[Banerjee1986] S. Banerjee et al., Conduction mechanism in the radiation damaged MINP Si solar cells, IEEE Trans. Nucl. Science, 33, 1474, 1986

[Barth2003] J. L. Barth et al., Space, Atmospheric and Terrestrial Radiation Environments, IEEE Trans. On Nucl. Scien., 50, 3, 2003

[Bertuccio2003] G. Bertuccio et al., SiC x-ray detectors for spectroscopy and imaging over a wide temperature range, Mater. Sci. Forum, 433, 941, 2003

[Bourdarie2008] S. Bourdarie et al., The Near- Earth Space Radiation Environment, IEEE Trans. On Nucl. Scien., 55, 4, 2008

[Cai2014] J. Cai et al., High-performance 4H-SiC- based p-i-n ultraviolet photodiode
and investigation of its capacitance characteristics, Optics Communications, 333, 182–186, 2014

[Castaldini2004] A. Castaldini et al., Low temperature annealing of electron irradiation induced defects in 4 H- SiC, Appl. Phys. Lett., 85, 17, 2004

[Castaldini2005] A. Castaldini et al., Deep levels by proton and electron irradiation in 4H–SiC, J. Appl. Phys. 98, 053706, 2005

[Claeys2002] C. Claeys E. Simoen, Radiation Effects in Advanced Semiconductor Materials and Devices, ed. Springer, 2002

[Cutroneo2013] M. Cutroneo et al., High performance SiC detectors for MeV ion beams generated by intense pulsed laser plasmas, Journal of Materials Research, 28, 1, 2013

[Danno2005] K. Danno, et al., Midgap levels in both n- and p-type 4H–SiC epilayers investigated by deep level transient spectroscopy, Appl. Phys. Lett., 86, 122104, 2005

[Danno2007] K. Danno, et al., Deep level transient spectroscopy on as-grown and electron irradiated p-type 4H-SiC epilayers, J. Appl. Phys., 101, 103704, 2007

[Davydov2001] D.V. Davydov et al., DLTS study of defects in 6H- and 4H SiC created by proton irradiation, Physica B, 308–310, 641–644, 2001

[De Napoli2007] M. De Napoli et al., Light ions response of silicon carbide detectors, Nucl. Instrum. Methods Phys. Res., Sect. A, 572, 831, 2007

[Doyle1998] J. P. Doyle et al., Electrically active point defects in n-type 4H– SiC, J. Appl. Phys., 84, 3, 1998

[Ewing2007] D. J. Ewing et al., Inhomogeneities in Ni/4H-SiC Schottky barriers: Localized Fermi-level pinning by defect states, J. Appl. Phys., 101, 114514, 2007,

[Fabbri2009] F. Fabbri et al., Comparison between cathodoluminescence spectroscopy and capacitance transient spectroscopy on Al^{+} ion implanted 4H-SiC p^{+} n diodes, Superlattices and Microstructures, 45, 383, 2009

[Frazzetto2011] A. Frazzetto, et al., “Structural and transport properties in alloyed Ti/Al Ohmic contacts formed on p-type Al-implanted 4H-SiC annealed at high temperature”, J. Phys. D: Appl. Phys., 44, 255302, 2011

[Gulnahar2014] Murat Gülnahar, Temperature dependence of current-and capacitance–voltage characteristics of an Au/4H-SiC Schottky diode, Superlattices and Microstructures, 76, 394–412, 2014

[Hallen2010] A. Hallén et al., Low-Temperature Annealing of Radiation-Induced Degradation in 4H-SiC Bipolar Junction Transistors, IEEE Electr. Dev. Lett., 31, 7, 2010

[Hazdra2013] P. Hazdra et al., Radiation defects produced in 4H-SiC epilayers by proton and alpha-particle irradiation, Materials Science Forum, 740-742, 661-664, 2013

[Hazdra2014] P. Hazdra et al., Point defects in 4H– SiC epilayers introduced by neutron irradiation, Nuclear Instruments and Methods in Physics Research B, 327, 124, 2014

[Hazdra2019] P. Hazdra et al., Radiation Defects Created in n-Type 4H-SiC by Electron Irradiation in the Energy Range of 1–10 MeV, Phys. Status Solidi A, 216, 1900312, 2019

[Hazdra2021] P. Hazdra et al., Radiation Resistance of High-Voltage Silicon and 4H-SiC Power p-i-n Diodes, IEEE Trans. Electr. Dev., 68, 202-207, 2021

[Hemmingsson1997] C. Hemmingsson et al., Deep level defects in electron-irradiated 4H-SiC epitaxial layers, J. Appl. Phys., 81, 9, 1997

[Hemmingsson1998] C. Hemmingsson et al., Negative-U centers in 4H silicon carbide, Phys. Rev. B, 58, 16, 1998

[Izzo2008] G. Izzo et al., Electrical properties of high energy ion irradiated 4H-SiC Schottky diodes, J. Appl. Phys., 104, 093711, 2008

[Izzo2009] G. Izzo et al., Defects in High Energy Ion Irradiated 4H-SiC, Materials Science Forum, 615- 617, 397, 2009

[Kawara2013] K. Kawahara et al., Investigation on origin of $Z_{1/2}$ center in SiC by deep level transient spectroscopy and electron paramagnetic resonance, Appl. Phys. Lett., 102, 112106, 2013

[Kimoto2014] T. Kimoto and J. A. Cooper, Fundamentals of Silicon Carbide Technology Growth, Characterization, Device and Application, ed. John Wiley & Sons, 2014

[Konishi2003] R. Konishi et al., Development of Ni/Al and Ni/Ti/Al ohmic contact materials for p-type 4H-SiC, Mat. Sci. Eng. B, 98, 286, 2003

[Lang 1974]: D. V. Lang, Deep- Level transient spectroscopy: A new method to characterize traps in semiconductor, J. Appl. Phys., 45, 7, 1974.

[Lebedev 2000] A. A. Lebedev, et al., Doping of n-type 6H–SiC and 4H–SiC with defects created with a proton beam, J. Appl. Phys., 88, 11, 2000

[LebedevJr 2000] A. A. Lebedev Jr et al., Capacitance Measurements for Diodes in the Case of Strong Dependence of the Diode-Base Series Resistance on the Applied Voltage, Semiconductors, 34, 1, 2000

[Lebedev2019] A. A. Lebedev et al., Effect of high energy (15 MeV) proton irradiation on vertical power 4H-SiC MOSFETs, Semicond. Sci. Technol., 34, 045004, 2019

[Liang2016] J. Liang et al., Improved electrical properties of n-n and p-n Si/SiC junctions with thermal annealing treatment, J. Appl. Phys.,120, 034504, 2016

[Li2005] C. Li et al., Fabrication and Characterization of 4H-SiC P-N Junction Diodes
by Selective-Epitaxial Growth Using TaC as the Mask, J. Electr. Mater., 34, 4, 2005.

[Litrico2009] G. Litrico et al., Defects in high Energy Ion Irradiated 4H-SiC, Materials Science forum, 615- 617, 397- 400, 2009.

[Litrico2018] G. Litrico et al., Silicon Carbide detectors for nuclear physics experiments at high beam luminosity, Journal of Physics Conference Series, 1056, 012032-5, 2018

[Look1987] D. C. Look et al., Defect production in electron-irradiated n-type GaAs, J. Appl. Phys., 62, 3660- 3664, 1987

[Luo2003] Z. Luo et al., Impact of Proton Irradiation on the Static and Dynamic Characteristics of High-Voltage 4H-SiC JBS Switching Diodes, IEEE Trans. on Nucl. Scien., 50, 6, 2003

[Luo2004] Z. Luo et al., Proton Radiation Effects in 4H-SiC Diodes and MOS capacitors, IEE Trans. on nuclear science, 51, 6, 2004

[Margarone2008] D. Margarone et al., Diamond detectors for characterization of laser-generated plasma, Radiat. Eff. Defects Solids, 163, 463, 2008

[Matsunami2004] Matsunami H., Technological breakthroughs in growth control of silicon carbide for high power electronic devices, Jp. J. Appl. Phys., 43, 6835-6847, 2004

[Mayer1990] J. W. Mayer and S.S. Lau, Electronic Material Science: For Integrated circuits in Si and GaAs, ed. Macmillan. Inc., 1990

[Mazzillo2009] M. Mazzillo et al., "Highly Efficient Low Reverse Biased 4H-SiC Schottky Photodiodes for UV-Light Detection", IEEE Photonics Technology Letters, 21, 1782-1784, 2009.

[Mazzillo2015] M. Mazzillo et al., "Electro-Optical characterization of patterned thin metal film Ni_2Si-4H SiC Schottky photodiodes for UV light detection", IEEE Sensors Journal, 15, 1858-1863, 2015

[McPherson2002] M. McPherson, Nuclear Instruments and Methods in Physics Research A, 488, 100–109, 2002

[Messenger1992] G. C. Messenger, A Summary Review of Displacement Damage from High Energy Radiation in Silicon Semiconductors and Semiconductor Devices, IEEE Trans. on Nucl. Scien., 39, 3, 1992

[Moscatelli2007] F. Moscatelli et al., Effect of very high neutron fluence irradiation on p+n junction 4H-SiC diodes, Mater. Sci. Forum, 556, 917-920, 2007

[Muhammad2018] H. Muhammad et al., Power Electronics Handbook, Elsevier Inc., 2018

[Musumeci2014] P. Musumeci et al., Silicon carbide detectors for diagnostics of ion emission from laser plasmas, Phys. Scr, T161, 014021, 2014

[Nastasi2006] M. Nastasi, J.W. Mayer, Ion Implantation and Synthesis of Materials, Springer, 2006

[Nava2008] F. Nava et al., Silicon carbide and its use as radiation detector material, Meas. Sci. Technol., 19, 102011-102046, 2008

[Neudek1983] G. W. Neudeck, The P-N Junction Diode, vol. 2 of Modular series on solid
state devices, ed. Wesley Publishing Inc., 1983

[Neudek1998] G. W. Neudeck, Perimeter Governed Minority Carrier Lifetimes in 4H-SiC
p^+n Diodes Measured by Reverse Recovery Switching Transient Analysis, J. Electr. Mater., 27, 4, 1998

[Nigam2002] S. Nigam et al., High energy proton irradiation effects on SiC Schottky rectifiers, Appl. Phys. Lett., 81, 13, 2002

[Nipoti2018] R. Nipoti et al., Perimeter and Area Components in the I–V Curves of 4H-SiC Vertical p^+-i-n Diode with Al^+ Ion-Implanted Emitters, IEEE Trans. on electr. dev., 65, 2, 2018

[Omotoso2018] E. Omotoso et al., Electrical characterisation of deep level defects created by bombarding the n-type 4H-SiC with 1.8 MeV protons, Surface and Coating Technology, 355, 2, 2018

[Pistavu 2019] G. Pistavu et al., Characterization of non-uniform Ni/4H-SiC Schottky diodes for improved responsivity in high-temperature sensing, Materials Science in Semiconductor Processing, 94, 64–69, 2019

[Paese1987] R. L. Paese et al., Comparison of proton and neutron carrier removal rates, IEEE Transactions on Nuclear Science, NS-34, 6, 1987

[Pellegrino2021] D. Pellegrino et al., Correlation between defects and electrical performances of ion irradiated 4H-SiC p-n junctions, Materials, 14, 8, 2021

[Pezzimenti2017] F. Pezzimenti et al., Analysis of the forward I-V characteristics of Al-implanted 4H-SiC pin diodes with modelling of recombination and trapping effects due to intrinsic and doping induced defect state, J. of Electronic Material, 47, 1-14, 2017

[Roccaforte2001] F. Roccaforte et al., Improvement of high temperature stability of nickel contacts on n-type 6H-SiC, Appl. Surf. Sci., 184, 295, 2001

[Roccaforte2004] F. Roccaforte et al., Stuctural and electrical properties of Ni/Ti Schottky contacts on silicon carbide upon thermal annealing, J. App. Phys., 96, 4313, 2004

[Roccaforte 2006] F. Roccaforte et al., Defects and electrical behavior in 1MeV Si^{+}-ion irradiated 4H–SiC Schottky diodes, J. of Appl. Phys., 99, 013515, 2006

[Ruddy2006] F.H. Ruddy et al., The fast neutron response of 4H silicon carbide semiconductor radiation detector, IEEE Trans. Nucl. Sci., 53, 1666, 2006

[Sah1957] C.-T. Sah, et al., Carrier generation and recombination in P-N junction and P-N junction characteristics, Proc. IRE, 45, 1228, 1957.

[Sciuto2015] A. Sciuto, M. Mazzillo, S. Di Franco, F. Roccaforte, G. D'Arrigo, “Visible blind 4H-SiC P+-N UV photodiode obtained by aluminum implantation”, IEEE Photonics Journal, vol. 76801906-6801910, 2015

[Sciuto2016] A. Sciuto et al., SiC interdigit detectors for post- accelerated ions generated by laser plasma, Vacuum 131, 170, 2016

[Sciuto2021] Sciuto, A et al., 4H-SiC p-n Junction- Based Near IR Photon Source, IEEE Sensors Journal, 21, 1504–1509, 2021.

[Schwank2008] James R. Schwank et al., Radiation Effects in MOS Oxides, IEEE Trans. on Nucl. Scien., 55, 4, 2008

[Shroder 2006] D. K. Schroder, Semiconductor Material and Device Characterization, ed. John Wiley & Sons, Inc., 2006

[Shockley1950] W. Shockley, The Theory of p-n Junctions in Semiconductors and p-n Junction Transistors, Bell Syst. Tech. J., 28, 435, 1949

[Shockley1952] W. Shockley et al., Statistics of the Recombinations of Holes and Electrons, Physical Review, 87, 5, 1952

[Seely2005] J. F. Seely et al., Response of a SiC photodiode to extreme ultraviolet through visible radiation, Optics Letters, 30, 3120-3122, 2005

[Siemieniec 2006] R. Siemieniec et al., Irradiation-Induced Deep Levels in Silicon for Power Device Tailoring, J. Electrochemical Society, 153, 2, 2006

[Spera2019] M. Spera et al., Effect of high temperature annealing ($T > 1650\ °C$) on the morphological and electrical properties of p-type implanted 4H-SiC layers, Mater. Science in Sem. Processing, 93, 274-279, 2019.

[Strel'chuk1997] A. M. Strel'chuk, et al., Shunting patterns occurring in epitaxial 6H-SiC p-n structures for high-voltage rectifiers, Materials Science and Engineering, B46, 231-235, 1997

[Strel'chuk2001] A. M. Strel'chuk, et al., Ideal 4H-SiC p-n junction and its characteristic shunt, Materials Science and Engineering, B80, 378, 2001

[Strel'chuk2005] A. M. Strel'chuk, et al., Influence of Gamma- Ray and Neutron Irradiation on injection characteristics of 4H-SiC p-n structures, Materials Science forum, 483- 485, 993- 996, 2005

[Strel'chuk2006] A. M. Strel'chuk, et al., About the nature of recombination current in 4H-SiC p-n structures, Materials Science forum, 527-529, 1343-1346, 2006

[Strel'chuk20014] A. M. Strel'chuk, et al., Variant of excess current in 4H-SiC p-n structures, Materials Science forum, 778-780, 859-862, 2014

[Strel'chuk 2017] A. M. Strel'chuk et al., Effect of neutron irradiation on current-voltage characteristics of packaged diodes based on 6H-SiC p-n structures, Mater. Sci. Forum, 897, 459-462, 2017

[Storasta 2001] L. Storasta et al., Pseudodonor nature of the D_I defect in 4H-SiC, Appl. Phys. Lett., 78, 1, 2001.

[Storasta 2004] L. Storasta et al., Deep levels created by low energy electron irradiation in 4 H- SiC, J. Appl. Phys., 96, 9, 2004

[Sze 1981] S. M. Sze, Physics of semiconductor devices, 2a ed. Wiley, 1981

[Tin2012] C. C. Tin, Characterization of Materials, Wiley & Sons Inc., 2012

[Torrisi2009] L. Torrisi et al., Single crystal silicon carbide detector of emitted ions and soft x rays from power laser-generated plasmas, J. Appl. Phys., 105, 123304, 2009

[Torrisi2012] L. Torrisi et al., SiC Detectors for Sub-MeV Alpha Spectrometry, Journal of Electronic Materials, 46, 7, 2017

[Torrisi2015] L. Torrisi et al., Laser-plasma X-ray detection by using fast 4H-SiC interdigit and ion collector detectors, J. Instrum. 10, 1748, 2015

[Tuomisto2019] F. Tuomisto, Characterisation and Control of Defects in Semiconductors, The Institution of Engineering and Technology, 2019

[Usman2010] M. Usmann et al., Effect of 3.0MeV helium implantation on electrical characteristics of 4H-SiC BJTs, Phys. Scr., T141, 014012, 2010

[Vanlint1971] V. A. J. Van Lint et al., Ionization Radiation Effects in Insulators and Insulating Parts, IEEE Trans. Electr. Insul., EI-6, 3, 1971

[Was2007] Gary S. Was, Fundamentals of Radiation Materials Science, ed. Springer, 2007

[Webster2004] J.G. Webster, Electrical Measurement signal processing and displays, ed. CRC press, 2004

[Willander2006] M. Willander et al., Silicon carbide and diamond for high-temperature device applications, Journal of Materials Science Materials in Electronics, 17, 1-25, 2006.

[Wolf1977] M. Wolf et al., Investigation of the Double Exponential in the Current-Voltage
Characteristics of Silicon Solar Cells, IEEE Trans. Electron Devices, 24, 419, 1977

[Zeigler1981] J. F. Ziegler et al., The effect of sea level cosmic rays on electronic device, J. Appl. Phys., 52, 6, 1981.

[Zeller1995] H. R. Zeller, Cosmic ray induced failure in high power semiconductor device, Solid State Electronics, 38, 12, 1995

[Zeigler1998] J. F. Ziegler et al., Terrestrial cosmic ray intensities, IBM J. Res. Develop., 42, 1, 1998

[Ziegler 2013] J. Ziegler, SRIM, The Stopping and range of ions in Matter, actual website (2013) http://www.srim.org/.

Acknowledgment

I wish to thank my tutor, Prof. L. Calcagno, she gave me a lot of her knowledge, experience, time and practice with her kindness and availability. I truly appreciate her view on scientific research and I have really enjoyed working with she. I would like to thank Dr. A. Sciuto of IMM- CNR, section of Catania, who gave me the chance to work in his group. His knowledge and guide have stimulated in me the interest for the scientific research and I learned a lot from his way to conceive the scientific work.

I wish to thank Prof. E. Bruno for its help, suggestions and support during this PhD work. I am also grateful to Dott. M. Zimbone for being always present when I need assistance and for the useful discussion.